Czech Technical University in Prague
Faculty of Mechanical Engineering

Department of Technical Mathematics

Dissertation Thesis

2011   Jiří Šimonek

Czech Technical University in Prague
Faculty of Mechanical Engineering

Department of Technical Mathematics

Numerical Solution of the Turbulent Stratified Flows in Atmospheric Boundary Layer

Ph.D. study program:
Mathematical and Physical Engineering

Author: Jiří Šimonek

Supervisor: Prof. RNDr. Karel Kozel, DrSc.

Abstract

The thesis deals with the numerical solution of the 2D and 3D flows in atmospheric boundary layer. Flows in atmospheric boundary layer are modeled as a flow of the incompressible fluid. The work presents several mathematical models that could be used to simulate the flows in atmospheric boundary layer and shows results of these simualtions on 2D and 3D geometries, usually flows around cosine function shaped hills.

To simulate the fluid flow in atmospheric boundary layer means to use a large scale computational domains, where the lengt scales are ones or tens of kilometres and the velocities of the fluid motion are from ones to tens of metres per second and it leads to simulations with very high Reynolds numbers about $10^7 - 10^9$.

There has been taken into account a simple system of incompressible incompressible Reynolds averaged Navier-Stokes equations together with the Cebecci-Smith algebraic turbulence model as a mathematical model and the first results have been obtained. The second mathematical model that has been used to simulate the flows in atmospheric boundary layer is the Boussinesq model, i.e. the system of incompressible Reynolds averaged Navier-Stokes equations with addition of the equation of density change. The second model has been tuned on several 2D and 3D geometry configurations and computational grids with different boundary conditions in order to achieve a creation of so called Lee waves which should be present in a stably stratified flows.

The overview and validation of $k - \varepsilon$ type turbulence models and first stably stratified flows over the "Witch of Agnesi hill" using standard $k - \varepsilon$ turbulence model are presented in this work and compared with another numerical results.

The thesis also brings an overview of mathematical a numerical methods that have been used to compute all results, such as artificial compressibility method, finite volume method and explicit numerical schemes (multistage Runge-Kutta scheme and Lax-Wendroff (Mac-Cormack) scheme).

Key words: Computational Fluid Dynamics, Finite Volume Method, Artificial Compressibility Method, Atmospheric Boundary Layer Flows, Variable density Flows, Stratified Flows, High Reynolds Number Flows

Abstrakt

Práce pojednává o numerickém modelování 2D a 3D proudění v mezní vrstvě atmosféry. Proudění v mezní vrstvě atmosféry je modelováno jako proudění nestlačitelné tekutiny. V práci je představeno několik matematických modelů, které mohou být použity k simulacím proudění v mezní vrstvě atmosféry, a prezentovány výsledky numerických simulací provedených na 2D a 3D geometriích. Povětšinou je uvažováno proudění okolo kopečků tvaru funkce cosinus.

Simulovat proudění v mezní vrstvě atmosféry znamená simulovat proudění v oblastech, jejichž charakteristické rozměry jsou v řádech jednotek až desítek kilometrů a rychlosti proudění jsou řádově jednotky až desítky metrů za sekundu. Tyto parametry vedou na simulace s obrovskými Reynoldsovými čísly kolem $10^7 - 10^9$.

Jako nejjednodušší matematický model byly použity nestlačitelné středované Reynoldsovy rovnice, uzavřené algebrackým modelem turbulence, a byly získány první numerické výsledky. Jako druhý model pro simulace proudění v mezní vrstvě atmosféry byl použit Boussinesqův model, to znamená nestlačitelné středované Reynoldsovy rovnice s přidanou transportní rovnicí pro hustotu. Druhý model byl laděn na několika různých 2D a 3D konfiguracích geometrie výpočetní oblasti s různými okrajovými podmínkami, za účelem získání výsledků proudění s vlnitým charakterem ("lee waves"), vlny které by měly vznikat u stratifikovaného proudění v mezní vrstvě atmosféry.

Část práce je věnovaná také modelování turbulence a popisuje vybrané turbulentní modely typu $k - \varepsilon$. Jsou zde také prezentovány první numerické výsledky proudění okolo kopečku tvaru "Witch of Agnesi" s použitím standardního $k - \varepsilon$ modelu turbulence a jejich srovnání s jinými numerickými vysledky.

Práce také přináší přehled matematických a numerických metod, které byly použity k vypočtení všech prezentovaných výsledků, jako jsou metoda umělé stlačitelnosti, metoda konečných objemů a explicitní numerická schémata (vícestupňové Runge-Kuttovo schéma a Laxovo-Friedrichsovo (MacCormackovo) schéma).

Klíčová slova: Počítačová mechanika tekutin, metoda konečných objemů, metoda umělé stlačitelnosti, proudění v mezní vrstvě atmosféry, proudění s proměnnou hustotou, stratifikované proudění, proudění s vysokými Reynoldsovými čísly

Contents

List of Figures

14

List of symbols

Latin symbols

c_f	friction coefficient
c_p	specific heat capacity at a constant pressure
c_v	specific heat capacity at a constant volume
$\mathbf{D}$	artificial dissipation
e	energy (per unit of mass)
E	energy (per unit of volume)
$\mathbf{F}$, $\mathbf{G}$, $\mathbf{H}$	convective fluxes
$\tilde{\mathbf{F}}$, $\tilde{\mathbf{G}}$, $\tilde{\mathbf{H}}$	numerical convective fluxes
Fr	Froude number
$\mathbf{g}$	vector of gravitational acceleration
g_i	i$^{\text{th}}$ component of gravitational acceleration vector
g_z	component of gravitational acceleration vector in z axis direction
i	internal energy (per unit of mass)
k	turbulent kinetic energy
$\mathbf{K}$	source term
$\tilde{\mathbf{K}}$	numerical source term
$\mathbf{L}$	residual operator
$\tilde{\mathbf{L}}$	residual operator with added artificial dissipation
L_m	mixing length
$\mathbb{M}$	matrix
$\mathbf{n}$	outer normal vector
N	Brunt-Väisälä frequency
p	pressure
p_0	reference pressure distribution
p_{0_A}	reference atmospheric pressure
P_k	production of turbulent kinetic energy
$\mathbf{q}$	heat flux vector
$\mathbf{R}$, $\mathbf{S}$, $\mathbf{T}$	diffusive fluxes
$\tilde{\mathbf{R}}$, $\tilde{\mathbf{S}}$, $\tilde{\mathbf{T}}$	numerical diffusive fluxes
$\mathbf{R}$, $\mathbf{S}$, $\mathbf{T}$	diffusive fluxes
$\tilde{\mathbf{R}}$, $\tilde{\mathbf{S}}$, $\tilde{\mathbf{T}}$	numerical diffusive fluxes
R	gas constant
Ri	Richardson number
Re	Reynolds number
S_E	source term in the energy equation

S_i	source term in the internal energy equation
S_{ij}	mean rate of strain tensor
$\mathbf{S}_M$	source term in the momentum equation (vector)
S_{M_i}	i[th] component of the source term in the momentum equation
t	time
T	temperature
T_0	reference temperature distribution
u_i	i[th] component of velocity vector
$u,\ v,\ w$	components of velocity vector
$\mathbf{U}$	velocity vector
u_r	friction velocity
V	volume of a cell
$\mathbf{W}$	vector of conservative variables

Greek symbols

β	thermal expansion coefficient
$\tilde{\beta}$	artificial speed of sound (artificial compressibility method)
δ	boundary layer thickness
δ_{ij}	Kronecker's symbol
Δt	time step
$\Delta x,\ \Delta y,\ \Delta z$	spatial step size
ε	turbulent kinetic energy dissipation rate
Θ	potential temperature
Θ_0	reference potential temperature distribution
κ	coefficient of thermal conduction
μ	dynamic viscosity
ν	kinematic viscosity
ν	kinematic viscosity
ν_t	turbulent kinematic viscosity
ν_{t_i}	turbulent kinematic viscosity (in inner region)
ν_{t_o}	turbulent kinematic viscosity (in outer region)
ν_e	sum of laminar and turbulent kinematic viscosity
ρ	density
ρ_0	reference density distribution
ρ_{0_w}	density on the ground, where $z = 0$
ρ_H	density on the upper boundary of the domain
ρ_w	density on the ground, where $z \neq 0$
$\rho_A,\ \rho_B,\ \rho_C$	spectral radius of the matrix $\mathbb{A}$, $\mathbb{B}$, $\mathbb{C}$
τ	shear stress tensor
τ_{ij}	i[th], j[th] component of the shear stress tensor
Ω	domain of solution (computational)
Ω_i	i[th] finite volume
$\partial\Omega$	domain boundary

Acknowledgements

I would like to thank to my supervisor Prof. RNDr. Karel Kozel, DrSc. for support and motivation that he was giving to me during my Ph.D. studies and also for many advices and remarks to my work that helped me to finish this thesis.

Chapter 1

Introduction

The thesis deals with the computational fluid dynamics (CFD) to be precise with modeling of atmospheric boundary layer flows. CFD is a part of the quite young and fast growing family of numerical simulations of physical processes. The popularity of numerical simulations in general grows fast nowadays, mainly thanks to fast growing computational power of today's computers. It is much more cheaper and faster to run the numerical simulation than to perform an experiment and also sometimes it could be almost impossible to do an experiment but the numerical simulation can provide accurate results. One of the branch where the CFD simulation could provide us more information than experiment is the flow in atmospheric boundary layer.

Atmospheric Boundary Layer, sometimes called planetary boundary layer, is the lowest part of the troposphere that is directly influenced by the presence of the Earth's surface, and responds to surface forcing with a timescale of about an hour or less. This forcing includes frictional drag, evaporation and transpiration, heat transfer, pollutant emission, and terrain induced flow modification. The boundary layer thickness is quite variable in time and space, ranging from tens of meters in strongly statically stable situations, to several kilometers in convective conditions [10]. It is often turbulent and is capped by a statically stable layer of air or temperature inversion. The shape of the ground strongly influences the air flow. The boundary layer is quite thin over smooth terrains, and much thicker over hilly, tree-covered, or urban areas with many large buildings.

Atmospheric boundary layer flows are related to meteorology and weather forecasts, transport of pollutant particles and their sedimentation (environmental problems), placing of wind-power plants, influence of large buildings and many other applications. Due to all the things that have been mentioned above is very necessary to know as much as possible about the behavior of the flows in atmospheric boundary layer in order to do right decisions which could influence the environment.

Simulation of atmospheric boundary layer flows is not a trivial problem. To find a complex mathematical model and a robust numerical method that will be able accurately capture all the phenomena of atmospheric boundary layer flows and will be computable on today's computers is very challenging task nowadays.

The flows in atmosphere are influenced by a lot of factors such as non constant vertical pressure, density and temperature distribution (stratification) and also the topology and roughness of the ground. The next thing is that the flow in atmospheric boundary layer is always a large scale problem. The size of the domain is about ones to tens of kilometers and the flow velocities are about ones to tens of meters per second. The resulting Reynolds numbers are between $10^7 - 10^9$, which means that the flow is fully turbulent (turbulence

is anisotropic in atmospheric boundary layer) and the choice of the turbulence modeling method plays significant role. But, the usage of methods such as direct numerical simulation (DNS) or large eddy simulation (LES) is almost impossible in cases with such a high Reynolds numbers. Then the possible solution of modeling turbulent flows is to use the system of Reynolds averaged Navier-Stokes (RANS) equations together with suitable turbulence model.

The state of the art

The simulation of the atmospheric boundary layer flows and stratified flows have been investigated at the Czech Technical University - Faculty of Mechanical Engineering - Department of Technical Mathematics in cooperation with the Institute of Thermo-mechanics of Czech Academy of sciences and with French LSEET Université de Toulon et du Var for more than 15 years.

In the beginning the basic problem and the simple mathematical model describing the atmospheric boundary layer flows has been chosen (Beneš, Bodnár, Sládek and Kozel) [21], [22]. Later on, the model has been improved by addition of the equation for transport of the passive pollutants. This model has been used for forecasts of the spread and sedimentation of pollutants coming from the brown coal depot [37], [38]. The similar problem has been investigated by Castro [23], [24], who compared the experimental data with the numerical simulation.

The stratified flows have been solved also by Beneš, Fürst and Fraunié [27]. The behavior of the stratified fluid in towing tank has been investigated in this case. Nowadays the thermally stratified atmospheric boundary layer flows are solved by Sládek, Kozel and Jaňour [34], [35], [36] who has been working on validation of the potential temperature model and comparison of the results with Eidsvik and Utnes [26]. The density based model, that has been used the most for numerical simulations of the stratified atmospheric boundary layer flows presented in this thesis, is similar to the one that has been presented by Uchida and Ohya [50]. This model was investigated also by Fürst, Beneš and Fraunié [17], [19], [27] applied to the atmospheric boundary layer flows and stratified flows in towing tank.

Aims of the work

Choice of the mathematical model
The choice of the governing equations and the appropriate boundary conditions plays the key role in further modeling. On the one hand the model has to correspond the with the phenomenon that is going to be modeled. On the other hand the mathematical model should be the simplest possible to be easily solvable.

Development of the numerical method and solver
The selected numerical method has to be the as accurate as possible, but also easy to implement.

Validation and application of the model and numerical method
It should be shown how the results of selected method correspond with the real phenomena by comparison of obtained results with the experimentally obtained data or with numer-

ical results of the similar mathematical model obtained by another numerical method. Application of the method to the real cases or to the cases that should model the real applications should be presented.

Structure of the thesis

Part I - Mathematical Models

The governing equations describing fluid motion are introduced in the first chapter of this thesis. These equations are partial differential equations arising from the conservation laws. To be exact, they are derived from the conservation of mass, momentum and energy. The main ideas of the derivation of governing equations are presented. Resulting equations are so called Navier-Stokes equations. Their name comes from the names of two men Claude-Louis Navier and George Gabriel Stokes, who independently derived these equations in 19th century. Hereafter the several forms of Navier-Stokes equations are mentioned, especially the variants of variable density flows, stratified flows. Readers will see that the variable density flows could be modeled by several approaches, using the transport equations for three different quantities, which are absolute temperature, potential temperature and density.

The second chapter is devoted to turbulent flows modeling. Several methods for modeling turbulent flows such as Direct Numerical Simulation (DNS), Large Eddy Simulation (LES) and averaging of Navier-Stokes equations are briefly introduced there. Much more interest is devoted to the last mentioned averaging of Navier-Stokes equations. The Reynolds Averaged Navier-Stokes equations are presented and algebraic turbulence models and several $k - \varepsilon$ turbulent kinetic energy transport turbulence models are described. Also the $k - \varepsilon$ turbulence model developed for the stratified flows is mentioned.

Part II - Numerical Solution

The chosen governing equations for modeling atmospheric boundary layer flows are introduced there in theirs standard and vector forms. The scaling of flow variables is shown there. The artificial compressibility method for pressure-velocity coupling for incompressible Navier-Stokes equations has been chosen and is described. The finite volume method (FVM) has been chosen as a discretization method of the governing equations and two explicit numerical schemes (multistage Runge-Kutta scheme and Lax-Wendroff scheme in MacCormack form) have been presented and used for further numerical computations. A section devoted to the stability issues of selected schemes is also in this part and a the stabilizing of the computations using artificial dissipation (artificial viscosity) is mentioned there. The basic 2D and 3D computational domains with one cosine function shaped hill and 2D computational domain with one so called "Which of Agnesi" hill and the survey of boundary conditions that have been used to close the mathematical model are stated at the end of this numerical part.

Part III - Numerical Results

Selected numerical results are presented and commented in last part of this thesis. Several 2D and 3D results of simplified real-case stratified atmospheric boundary layer flows are presented (the stratified flows over cosine shaped hills). The validation of the newly

implemented standard $k - \varepsilon$ turbulence model and first results of the neutrally stratified turbulent flows modeled using this turbulence model are shown and compared with the other results in this part.

Part I

Mathematical Models

Chapter 2

Governing equations

Contents

First section of this chapter is devoted to the overview of basic mathematical models and principles in fluid dynamics modeling. The main part of mathematical model is the system of partial differential equations that describes the problem. The system of governing equations is always based on conservation laws of fluid dynamics. The conservation of mass, momentum and energy has to be fulfilled and some transport equations for any other quantities could be added to the basic system in order to affect all the quantities that one would like to model.

Following section gives to the reader just a brief overview about the conservation laws and theirs resulting partial differential equations. One can find the detailed derivation e.g. in [2], [3] or [11].

2.1 Conservation Laws of Fluid Motion

2.1.1 Conservation of Mass

The mass balance has to be fulfilled in the fluid motion. It means that the mass which comes into a selected volume of the fluid has to be the same as the mass that leaves this volume in each time interval. This could be expressed by a following equation:

$$\frac{\partial \rho}{\partial t} + \sum_{j=1}^{3} \frac{\partial \rho u_j}{\partial x_j} = 0, \tag{2.1}$$

or in vector form:

$$\frac{\partial \rho}{\partial t} + div(\rho \mathbf{U}) = 0. \tag{2.2}$$

Equations (2.1) and (2.1) describe the conservation of mass in the compressible fluid. If one assumes that the fluid is incompressible, i.e. the density ρ is constant. Then the previously defined continuity equations could be simplified as follows:

$$\sum_{j=1}^{3} \frac{\partial u_j}{\partial x_j} = 0, \tag{2.3}$$

or written in vector form:

$$div(\mathbf{U}) = 0. \tag{2.4}$$

Equation (2.3) and (2.4) are the continuity equations for the incompressible flows.

2.1.2 Conservation of Momentum

Newton's second law states that the rate of change of momentum of a fluid particle equals the sum of the forces on the particle. The rates of increase/decrease of x,y and z momentum per unit volume of a fluid particle are given by material derivatives of velocity components:

$$\rho \frac{Du_i}{Dt} = \frac{\partial \rho u_i}{\partial t} + \sum_{j=1}^{3} \frac{\partial \rho u_j u_i}{\partial x_j}, \tag{2.5}$$

There are two types of forces on fluid particles:
surface forces
    - pressure forces
    - viscous forces
body forces
    - gravity force
    - centrifugal force
    - Coriolis force
    - electromagnetic force

The surface forces are caused by pressure forces (described through the change of pressure p) and the viscous forces (described through the change of stress tensor τ_{ij}). The body forces are usually added as a source terms S_M in the momentum equations (S_{M_i} is the ith component of the momentum source term vector).

The x component of the momentum equation is found by setting the rate of change of x momentum of the fluid particle equal to the total force in the x direction on the element due to surface stresses plus the rate of increase of x momentum due to sources. The momentum equation (conservative form) could be given as follows:

$$\frac{\partial \rho u_i}{\partial t} + \sum_{j=1}^{3} \frac{\partial \rho u_j u_i}{\partial x_j} = -\frac{\partial p}{\partial x_i} + \sum_{j=1}^{3} \frac{\partial \tau_{ij}}{\partial x_j} + S_{M_i}, \tag{2.6}$$

where τ is the stress tensor and for Newtonian fluids is symmetrical and is defined as follows:

$$\tau_{ij} = \mu \left(\frac{\partial u_i}{\partial x_j} + \frac{\partial u_j}{\partial x_i} \right) - \frac{2}{3} \mu \left(\sum_{k=1}^{3} \frac{\partial u_k}{\partial x_k} \right) \delta_{ij}. \tag{2.7}$$

The above mentioned momentum equation (2.6) together with the stress tensor τ defined in (2.7) is the definition of momentum conservation for compressible flows. Using continuity equation (2.1) one obtains the momentum equation in a non-conservative form:

$$\rho \frac{\partial u_i}{\partial t} + \rho \sum_{j=1}^{3} u_j \frac{\partial u_i}{\partial x_j} = -\frac{\partial p}{\partial x_i} + \sum_{j=1}^{3} \frac{\partial \tau_{ij}}{\partial x_j} + S_{M_i}, \tag{2.8}$$

Lets suppose now that the density ρ is constant and use the continuity equation for incompressible flows (2.3), then one obtains the momentum equation for incompressible flows in conservative form:

$$\frac{\partial u_i}{\partial t} + \sum_{j=1}^{3} \frac{\partial u_j u_i}{\partial x_j} = -\frac{1}{\rho} \frac{\partial p}{\partial x_i} + \sum_{j=1}^{3} \frac{\partial \tau_{ij}}{\partial x_j} + S_{M_i}. \tag{2.9}$$

The continuity equation for incompressible flows has to be completed by the incompressible stress tensor τ term, which one obtains applying the incompressible continuity equation (2.3) on (2.7) and dividing (2.7) by density ρ:

$$\tau_{ij} = \nu \left(\frac{\partial u_i}{\partial x_j} + \frac{\partial u_j}{\partial x_i} \right). \tag{2.10}$$

If one substitutes the viscous force term in (2.9) by (2.10) and one uses incompressible continuity equation (2.3) then one obtains:

$$\sum_{j=1}^{3} \frac{\partial \tau_{ij}}{\partial x_j} = \frac{\partial}{\partial x_j} \sum_{j=1}^{3} \nu \frac{\partial u_i}{\partial x_j}, \tag{2.11}$$

and therefore the incompressible momentum equation (conservative form) could be defined as follows:

$$\frac{\partial u_i}{\partial t} + \sum_{j=1}^{3} \frac{\partial u_j u_i}{\partial x_j} = -\frac{1}{\rho} \frac{\partial p}{\partial x_i} + \frac{\partial}{\partial x_j} \sum_{j=1}^{3} \nu \frac{\partial u_i}{\partial x_j} + S_{M_i}, \tag{2.12}$$

and the non-conservative form of the incompressible momentum equation:

$$\frac{\partial u_i}{\partial t} + \sum_{j=1}^{3} u_j \frac{\partial u_i}{\partial x_j} = -\frac{1}{\rho} \frac{\partial p}{\partial x_i} + \frac{\partial}{\partial x_j} \sum_{j=1}^{3} \nu \frac{\partial u_i}{\partial x_j} + S_{M_i}. \tag{2.13}$$

2.1.3 Conservation of Energy

The energy equation is derived from the first law of thermodynamics which states that the rate of change of energy of a fluid particle is equal to the rate of heat addition to the fluid particle plus the rate of work done on the particle. The rate of increase/decrease of energy of a fluid particle per unit volume is given by:

$$\frac{DE}{Dt} = \frac{\partial E}{\partial t} + \sum_{j=1}^{3} \frac{\partial u_j E}{\partial x_j}, \tag{2.14}$$

where E is total energy per unit of volume (total energy density) that consists of the internal energy density plus kinetic energy density:

$$E = \rho \left(i + \frac{1}{2}|\mathbf{U}|^2 \right), \tag{2.15}$$

where i is the internal energy density (i.e. internal energy per unit volume) of the fluid particle.

Total rate of work done on the fluid particle by surface stresses:

$$-\sum_{j=1}^{3} \frac{\partial p u_j}{\partial x_j} + \sum_{j,k=1}^{3} \frac{\partial u_j \tau_{jk}}{x_j}, \tag{2.16}$$

where τ_{ij} is defined by (2.7).

The rate of heat addition to the fluid particle due to heat conduction:

$$-\sum_{j=1}^{3} \frac{\partial \mathbf{q}}{\partial x_j}, \tag{2.17}$$

where $\mathbf{q}$ is the heat flux defined by a Fourier's law:

$$\mathbf{q} = -\kappa \nabla T, \tag{2.18}$$

where κ is heat conduction coefficient and T is absolute temperature. Putting all the terms (2.14), (2.16), (2.17) together and adding a energy density source term S_E one obtains the complete energy equation (conservative form):

$$\frac{\partial E}{\partial t} + \sum_{j=1}^{3} \frac{\partial u_j E}{\partial x_j} = -\sum_{j=1}^{3} \frac{\partial p u_j}{\partial x_j} + \sum_{j,k=1}^{3} \frac{\partial u_j \tau_{jk}}{x_j} - \sum_{j=1}^{3} \frac{\partial q_j}{\partial x_j} + \rho \mathbf{q} + S_E, \tag{2.19}$$

using the continuity equation (2.1) and the specific total energy $e = E/\rho$ (i.e. per unit mass) $(e = \rho E)$ one obtains the energy equation in non-conservative form:

$$\rho \frac{\partial e}{\partial t} + \rho \sum_{j=1}^{3} u_j \frac{\partial e}{\partial x_j} = -\sum_{j=1}^{3} \frac{\partial p u_j}{\partial x_j} + \sum_{j,k=1}^{3} \frac{\partial u_j \tau_{jk}}{x_j} - \sum_{j=1}^{3} \frac{\partial q_j}{\partial x_j} + \rho \mathbf{q} + S_E, \tag{2.20}$$

The energy equation could be rewritten into the form where the unknown is the internal energy i. Lets multiply the equation (2.6) by a one half of velocity $\frac{1}{2}\mathbf{U}$ and sum all the terms and one obtains the equation for conservation of kinetic energy:

$$\rho \frac{D\left(\frac{1}{2}\mathbf{U}^2\right)}{Dt} = -\mathbf{U} \cdot \nabla p + \sum_{j,k=1}^{3} u_k \frac{\partial \tau_{jk}}{\partial x_j} + \mathbf{U} \cdot \mathbf{S}_M. \tag{2.21}$$

Subtracting (2.21) from (2.20) and defining a new source term $S_i = S_E - \mathbf{U} \cdot \mathbf{S}_M$ one obtains the internal energy equation:

$$\rho\frac{\partial i}{\partial t} + \sum_{j=1}^{3} u_j \frac{\partial i}{\partial x_j} = -p\sum_{j=1}^{3}\left(\frac{\partial u_j}{\partial x_j} - \frac{\partial q_j}{\partial x_j}\right) + \sum_{j,k=1}^{3}\tau_{jk}\frac{\partial u_k}{\partial x_j} + \rho\mathbf{q} + S_i \qquad (2.22)$$

2.1.4   Equation of state

In the system composed from the continuity equation (2.1), momentum equation (2.6) or (2.8) and energy equation (2.19) or (2.20) there is one more variable than the number of equations so one more equation has to be introduced. The closing equation is so called equation of state which arises from the thermodynamics laws. If one assumes an ideal gas then the equation of state is given by:

$$p = \rho R T, \qquad (2.23)$$

where R is so called universal gas constant. Using this state equation and thermodynamic laws the internal energy could be expressed as follows:

$$i = c_v T, \qquad (2.24)$$

where c_v is the specific heat capacity at a constant volume. One can see that internal energy i is proportional to the absolute temperature T. Using this relation could be very advantageous, because one can take the equation (2.22) substitute the internal energy i by $c_v T$ and solve the system directly with absolute temperature equation instead of energy or the internal energy equations.

The state equation (2.23) could be written in following form when the computation with the total energy density E (2.15) is assumed:

$$p = (\gamma - 1)\left[E - \frac{1}{2}\rho|\mathbf{U}|^2\right], \qquad (2.25)$$

where $\gamma = c_p/c_v$ (specific heat ratio).

2.2   Navier-Stokes equations for compressible flow

The system of equations describing the flow of compressible Newtonian fluid (ideal gas) are so called Navier-Stokes equations (named by Navier and Stokes, who independently derived these equations from the conservation laws). The system of non conservative Navier-Stokes equations consists of continuity equation (2.1), momentum equation (2.8), energy equation (2.20) or internal energy equation (2.22) and or the temperature equation like it is explained at the end of section 2.1.3 and closed by a equation of state for an ideal gas. The resulting system could be stated as follows (note: the Einstein's summation rule

is used from this point in following chapters):

$$\frac{\partial \rho}{\partial t} + \frac{\partial \rho u_j}{\partial x_j} = 0, \tag{2.26}$$

$$\frac{\partial \rho u_i}{\partial t} + \frac{\partial \rho u_j u_i}{\partial x_j} = -\frac{\partial p}{\partial x_i} + \frac{\partial \tau_{ij}}{\partial x_j} + S_{M_i}, \tag{2.27}$$

$$\frac{\partial E}{\partial t} + \frac{\partial u_j E}{\partial x_j} = -\frac{\partial p u_k}{\partial x_k} + \frac{\partial u_j \tau_{jk}}{x_j} - \frac{\partial q_k}{\partial x_k} + \rho \mathbf{q} + S_E, \tag{2.28}$$

$$p = (\gamma - 1)\left[E - \frac{1}{2}\rho|\mathbf{U}|^2\right], \tag{2.29}$$

where the components of stress tensor τ_{ij} are defined as in (2.7).

2.3 Navier-Stokes equations for incompressible (neutrally stratified flows)

Assuming the simplifications of the incompressible fluid the Navier-Stokes equations for modeling incompressible (neutrally stratified) Newtonian fluid flows could be written in following form:

$$\frac{\partial u_j}{\partial x_j} = 0, \tag{2.30}$$

$$\frac{\partial u_i}{\partial t} + u_j \frac{\partial u_i}{\partial x_j} + \frac{1}{\rho_0}\frac{\partial p}{\partial x_i} = \frac{\partial}{\partial x_j}\left(\nu \frac{\partial u_i}{\partial x_j}\right). \tag{2.31}$$

$$\tag{2.32}$$

Governing equations for modeling incompressible neutrally stratified flows in vector form could be written as follows:

$$\mathbb{M} \cdot \mathbf{W}_t + \mathbf{F}_x + \mathbf{G}_y + \mathbf{H}_z = \mathbf{R}_x + \mathbf{S}_y + \mathbf{T}_z, \tag{2.33}$$

where $\mathbb{M}$ is diagonal matrix with following entries:

$$\mathbb{M} = diag\,\|\,0,\ 1,\ 1,\ 1\|, \tag{2.34}$$

$\mathbf{W}$ is a vector of conservative variables:

$$\mathbf{W} = \|\,p,\ u,\ v,\ w\|^T, \tag{2.35}$$

$\mathbf{F}$, $\mathbf{G}$, $\mathbf{H}$ are vectors of convective fluxes:

$$\mathbf{F} = \left\|\begin{array}{c} u \\ u^2 + p \\ u \cdot v \\ u \cdot w \end{array}\right\|, \quad \mathbf{G} = \left\|\begin{array}{c} v \\ v \cdot u \\ v^2 + p \\ v \cdot w \end{array}\right\|, \quad \mathbf{H} = \left\|\begin{array}{c} w \\ w \cdot u \\ w \cdot v \\ w^2 + p \end{array}\right\|, \tag{2.36}$$

$\mathbf{R}$, $\mathbf{S}$, $\mathbf{T}$ are vectors of diffusive fluxes:

$$\mathbf{R} = \nu\left\|\begin{array}{c} 0 \\ u_x \\ v_x \\ w_x \end{array}\right\|, \quad \mathbf{S} = \nu\left\|\begin{array}{c} 0 \\ u_y \\ v_y \\ w_y \end{array}\right\|, \quad \mathbf{T} = \nu\left\|\begin{array}{c} 0 \\ u_z \\ v_z \\ w_z \end{array}\right\|. \tag{2.37}$$

2.4 Equations for modeling incompressible stratified flows

2.4.1 Equations for variable density flows

Let me introduce the system of equations for variable density flows. Following two approximations calculate with transport equation for temperature. The temperature equation is coupled with the system of Navier-Stokes equations by the density $\leftrightarrow$ temperature relation that is introduced too. Following equations for variable density flows (Boussinesq model and "Full approximation") have been presented in [14].

2.4.1.1 Boussinesq model

$$\frac{\partial u_j}{\partial x_j} = 0 \tag{2.38}$$

$$\frac{\partial u_i}{\partial t} + u_j \frac{\partial u_i}{\partial x_j} + \frac{1}{\rho_0}\frac{\partial p}{\partial x_i} = \frac{\partial}{\partial x_j}\left(\nu \frac{\partial u_i}{\partial x_j}\right) + \frac{1}{\rho_0}\left(\rho - \rho_0\right)g_i \tag{2.39}$$

$$\frac{\partial T}{\partial t} + u_j \frac{\partial T}{\partial x_j} = \frac{\partial}{\partial x_j}\left(\frac{\kappa}{\rho_0 c_p}\frac{\partial T}{\partial x_j}\right) \tag{2.40}$$

$$\rho - \rho_0 = -\rho_0 \beta \left(T - T_0\right) \tag{2.41}$$

The system has five differential equations in 3D for p (pressure), u, v, w (velocity vector components) and T (temperature) and the system is closed by the algebraic relation (2.41). The β is thermal expansion coefficient, c_p is specific heat capacity coefficient, κ is heat conductivity, ρ_0 is the reference density and T_0 is the reference temperature and g_i are the components of gravitational acceleration vector.

2.4.1.2 Full approximation

$$\rho \frac{\partial u_j}{\partial x_j} - \rho_0 \beta u_j \frac{\partial T}{\partial x_j} = 0 \tag{2.42}$$

$$\frac{\partial u_i}{\partial t} + u_j \frac{\partial u_i}{\partial x_j} + \frac{1}{\rho}\frac{\partial p}{\partial x_i} = \frac{\partial}{\partial x_j}\left(\nu\left[\frac{\partial u_i}{\partial x_j} + \frac{\partial u_j}{\partial x_i} - \frac{2}{3}\frac{\partial u_k}{\partial x_k}\delta_{ij}\right]\right) + g_i \tag{2.43}$$

$$\frac{\partial T}{\partial t} + u_j \frac{\partial T}{\partial x_j} = \frac{\partial}{\partial x_j}\left(\frac{\kappa}{\rho_0 c_p}\frac{\partial T}{\partial x_j}\right) + \frac{u_j}{\rho c_p}\frac{\partial p}{\partial x_j} \tag{2.44}$$

$$\rho - \rho_0 = -\rho_0 \beta \left(T - T_0\right) \tag{2.45}$$

There are some new terms in the system of equations. Those new terms arise from proper derivatives. Density is a function of temperature and is not constant any more. The meaning of the terms in this system is the same as in previous section 2.4.1.1.

2.4.2 Equations for stratified atmospheric boundary layer flows

2.4.2.1 Potential temperature based model

The potential temperature of fluid at pressure p is the temperature that fluid would acquire after adiabatic compression (expansion) to a standard reference pressure p_{0_A},

typically $p_{0_A} = 10^5 Pa$ (atmospheric pressure near the ground). The potential temperature is denoted Θ and is given by following equation:

$$\Theta = T \left(\frac{p_{0_A}}{p} \right)^{\frac{R}{c_p}}, \tag{2.46}$$

where T is the current absolute temperature (in K)., R is the gas constant of the fluid, and c_p is the specific heat capacity at a constant pressure.

The potential temperature based model for atmospheric boundary layer flows arise from the Boussinesq model and has been presented in [26], [53] and in [15]:

$$\frac{\partial u_j}{\partial x_j} = 0 \tag{2.47}$$

$$\frac{\partial u_i}{\partial t} + u_j \frac{\partial u_i}{\partial x_j} = \frac{\partial}{\partial x_j} \left(\nu \frac{\partial u_i}{\partial x_j} \right) - \frac{1}{\rho_0} \frac{\partial p}{\partial x_i} + \frac{\Theta}{\Theta_0} g_i \tag{2.48}$$

$$\frac{\partial \Theta}{\partial t} + u_j \frac{\partial \Theta}{\partial x_j} = \frac{\partial}{\partial x_j} \left(\frac{\kappa}{\rho_0 c_p} \frac{\partial \Theta}{\partial x_j} \right) \tag{2.49}$$

where κ is the coefficient of thermal conduction and c_p is the specific heat capacity at a constant pressure and g_i are the components of gravitational acceleration vector. The term Θ_0 (reference potential temperature distribution) could be defined according to [53] as follows:

$$\Theta_0 = \gamma z + \Theta_w, \tag{2.50}$$

where $\gamma = \partial \Theta_0 / \partial z$ and Θ_w is the temperature on the Earth's surface. The dissipation term $\frac{\partial}{\partial x_j} \left(\frac{\kappa}{\rho_0 c_p} \frac{\partial \Theta}{\partial x_j} \right)$ in the transport equation for potential temperature (2.49) is very often neglected.

This model could be rewritten is sense of pressure and potential temperature perturbations. The variables are split into the sum of initial values and their perturbation as follows:

$$p = p'' + p_0, \tag{2.51}$$

$$\Theta = \Theta'' + \Theta_0, \tag{2.52}$$

where p'' and Θ'' are the pressure and potential temperature perturbations and p_0 and Θ_0 are the reference distributions of pressure and potential temperature.
One can see the resulting modification of equations after this substitution e.g. in [15].

2.4.2.2 Density based model

Density based model is prescribed using the incompressible Navier-Stokes equations with addition of transport equation for density. There has been taken into account transport equation for density without diffusive terms on the RHS. In other words the diffusion coefficient of the transport equation for density is equal 0. This model has been published in [50] and arises from the Boussinesq model.

$$\frac{\partial u_j}{\partial x_j} = 0 \tag{2.53}$$

$$\frac{\partial u_i}{\partial t} + u_j \frac{\partial u_i}{\partial x_j} = \frac{\partial}{\partial x_j} \left(\nu \frac{\partial u_i}{\partial x_j} \right) - \frac{1}{\rho_0} \frac{\partial p}{\partial x_i} + \frac{\rho}{\rho_0} g_i \tag{2.54}$$

$$\frac{\partial \rho}{\partial t} + u_j \frac{\partial \rho}{\partial x_j} = 0 \tag{2.55}$$

Let me introduce a vector form of the previous system at this place, which will be very useful in the following chapters:

$$\mathbb{M} \cdot \mathbf{W}_t + \mathbf{F}_x + \mathbf{G}_y + \mathbf{H}_z = \mathbf{R}_x + \mathbf{S}_y + \mathbf{T}_z + \mathbf{K}, \tag{2.56}$$

where $\mathbb{M}$ is diagonal matrix with following entries:

$$\mathbb{M} = diag \, \| \, 0, \; 1, \; 1, \; 1, \; 1 \, \|, \tag{2.57}$$

$\mathbf{W}$ is a vector of conservative variables:

$$\mathbf{W} = \| \, p, \; u, \; v, \; w, \; \rho \, \|^T, \tag{2.58}$$

$\mathbf{F}$, $\mathbf{G}$, $\mathbf{H}$ are vectors of convective fluxes:

$$\mathbf{F} = \left\| \begin{array}{c} u \\ u^2 + p \\ u \cdot v \\ u \cdot w \\ u \cdot \rho \end{array} \right\|, \quad \mathbf{G} = \left\| \begin{array}{c} v \\ v \cdot u \\ v^2 + p \\ v \cdot w \\ v \cdot \rho \end{array} \right\|, \quad \mathbf{H} = \left\| \begin{array}{c} w \\ w \cdot u \\ w \cdot v \\ w^2 + p \\ w \cdot \rho \end{array} \right\|, \tag{2.59}$$

$\mathbf{R}$, $\mathbf{S}$, $\mathbf{T}$ are vectors of diffusive fluxes:

$$\mathbf{R} = \nu \left\| \begin{array}{c} 0 \\ u_x \\ v_x \\ w_x \\ 0 \end{array} \right\|, \quad \mathbf{S} = \nu \left\| \begin{array}{c} 0 \\ u_y \\ v_y \\ w_y \\ 0 \end{array} \right\|, \quad \mathbf{T} = \nu \left\| \begin{array}{c} 0 \\ u_z \\ v_z \\ w_z \\ 0 \end{array} \right\| \tag{2.60}$$

and $\mathbf{K}$ is the source term defined as follows in this case:

$$\mathbf{K} = \frac{\rho}{\rho_0} \, \| \, 0, \; 0, \; 0, \; -g_z, \; 0 \, \|^T. \tag{2.61}$$

2.4.2.3 Pressure perturbation model (Density based)

One can split the pressure into sum of its value when there is no motion in the fluid p_0 (initial value) and its perturbation p'' as follows:

$$p(z) = p'' + p_0, \tag{2.62}$$

and the same could be done with density (ρ_0 the value of density when there is no motion in the fluid (initial value), ρ'' the density perturbation):

$$\rho(z) = \rho'' + \rho_0. \tag{2.63}$$

and because the values of pressure p_0 and values of density ρ_0 has to be in equilibrium when there is no fluid motion, i.e.:

$$\frac{\partial p_0}{\partial x} = 0, \tag{2.64}$$

$$\frac{\partial p_0}{\partial y} = 0, \tag{2.65}$$

$$\frac{\partial p_0}{\partial z} = -\rho_0 g_z, \tag{2.66}$$

so if one substitute the pressure p in equation (2.54) by (2.62), one obtains the system in which the unknowns are the pressure perturbations:

$$\frac{\partial u_j}{\partial x_j} = 0, \tag{2.67}$$

$$\frac{\partial u_i}{\partial t} + u_j \frac{\partial u_i}{\partial x_j} = \frac{\partial}{\partial x_j}\left(\nu \frac{\partial u_i}{\partial x_j}\right) - \frac{1}{\rho_0}\frac{\partial p''}{\partial x_i} + \frac{\rho''}{\rho_0}g_i, \tag{2.68}$$

$$\frac{\partial \rho}{\partial t} + u_j \frac{\partial \rho}{\partial x_j} = 0. \tag{2.69}$$

This system has been used in a numerical model for all the computations of stratified flows that have been presented in this thesis.

2.4.3 Stability of Stratified Flows

We distinguish three types of stratification [6], [15]:

Neutrally stratified fluid
  - potential temperature is constant

$$\frac{\partial \Theta}{\partial z} = 0. \tag{2.70}$$

Stably stratified fluid
  - potential temperature increases with increasing height

$$\frac{\partial \Theta}{\partial z} > 0. \tag{2.71}$$

Unstably stratified fluid
  - potential temperature decreases with height

$$\frac{\partial \Theta}{\partial z} < 0. \tag{2.72}$$

Chapter 3

Turbulence Modeling

Contents

There are several approaches in modeling turbulent flows. One of them, the most accurate one, is the Direct Numerical Simulation (DNS). DNS does not model the turbulent flow but it computes the Navier-Stokes equations on such a fine grid, that the turbulence appears in the results. Results have to be averaged over a selected time interval in order to obtain mean values of the flow (averaging of results). DNS needs very fine computational grid especially near walls. According to [9] the number of grid cells is proportional to $Re^9/4$, where Re is the Reynolds number of the flow. One can see that the requirements of the grid fineness grow very fast with the increasing Reynolds number. And this is the reason why it is impossible to perform DNS in simulation of atmospheric boundary layer flows, where the Reynolds number is about $10^7 - 10^9$ at this time.

The second way how to simulate turbulent flows is the statistical approach, where the instantaneous values of variables are split into mean values and fluctuations and only the mean values of the variables stand in the governing equations (averaging of equations). When the Reynolds averaging is applied on Navier-Stokes equations one obtains the system of so called Reynolds Averaged Navier-Stokes equations (RANS). The RANS system is not closed and a turbulence model has to be added.

The third approach in turbulence flows modeling is so called Large Eddy Simulation (LES). Where the large scale eddies are simulated directly as in DNS and the small scale eddies are modeled in a similar way as it is in RANS modeling. Nowadays as the computational power of computers grow the LES approach starts to substitute the RANS approach.

3.1 Reynolds Averaged Navier Stokes equations (RANS)

Statistical approach rests in splitting variables of the flow into mean values and fluctuations. Turbulence is the stochastic process and the flow variables are therefore chance quantities of time. The mean value of the chance quantity is defined as follows (when average of the chance quantity does not vary with time):

$$\overline{\Phi}(x_i) = \lim_{\Delta t \to \infty} \frac{1}{\Delta t} \int_{t_0}^{t_0 + \Delta t} \Phi(x_i, t) \, dt, \tag{3.1}$$

where t_0 is the initial time of averaging. The period of averaging Δt has to be much larger than the dominant period of changes of the averaged variable.

Using so called Reynolds averaging the instantaneous value of the variable is given by the sum of its mean value and the fluctuation:

$$A(x_i, t) = \overline{A}(x_i) + a''()x_i, t), \tag{3.2}$$

where the mean value $\overline{A}$ is given by equation (3.1) and the mean value of the fluctuation is equal to zero

$$\overline{a''}(t) = \lim_{\Delta t \to \infty} \frac{1}{\Delta t} \int_{t_0}^{t_0 + \Delta t} a''(t) \, dt = 0. \tag{3.3}$$

Applying averaging on the system of Navier-Stokes equations (2.30) and (2.31) one obtains Reynolds Averaged Navier-Stokes equations for the incompressible flow:

$$\frac{\partial \overline{u}_j}{\partial x_j} = 0 \tag{3.4}$$

$$\frac{\partial \overline{u}_i}{\partial t} + \overline{u}_j \frac{\partial \overline{u}_i}{\partial x_j} + \frac{1}{\rho} \frac{\partial \overline{p}}{\partial x_i} = \frac{\partial}{\partial x_j} \left(\nu \frac{\partial \overline{u}_i}{\partial x_j} \right) + \frac{\partial \tau_{ij}}{\partial x_j}, \tag{3.5}$$

where $\tau_{ij} = -\overline{u_i u_j}$ is the ij-component of the turbulent stress tensor. For an incompressible flow holds:

$$\tau_{ij} = -\overline{u_i'' u_j''} = 2\nu_t S_{ij} - \frac{1}{3} \overline{u_k'' u_k''} \delta_{ij} \tag{3.6}$$

where the mean rate of strain tensor S_{ij} is defined as follows:

$$S_{ij} = \frac{1}{2} \left(\frac{\partial \overline{u}_i}{\partial x_j} + \frac{\partial \overline{u}_j}{\partial x_i} \right). \tag{3.7}$$

When the turbulent kinetic energy k for the incompressible flow is introduced as:

$$k = \frac{1}{2} \overline{u_k'' u_k''}, \tag{3.8}$$

one can express the relation for the turbulent stress tensor τ_{ij} (3.6) in a following way:

$$\tau_{ij} = -\overline{u_i'' u_j''} = 2\nu_t S_{ij} - \frac{2}{3} k \delta_{ij}. \tag{3.9}$$

The turbulent viscosity ν_t is going to be modeled by a turbulence model.

The detailed derivation of the Reynolds Averaged Navier-Stokes equations can be found in [9].

3.2 Algebraic Turbulence Model

Algebraic turbulence model is prescribed by an algebraic relation. The turbulent viscosity is computed directly from the flow variables. Algebraic models have been designed for 2D incompressible boundary layer based on so called mixing length, which is proportional to the length that the vortex covers until it disappears by the mixing of the fluid. Turbulent viscosity is given by the following equation:

$$\nu_t = L_m^2 \left| \frac{\partial u}{\partial y} \right|, \tag{3.10}$$

where the mixing length L_m is set by algebraic relation:

$$L_m = \frac{1}{\delta} f \left(\frac{y}{\delta} \right), \tag{3.11}$$

where δ is the boundary layer thickness. More information about algebraic turbulence models could be found in [9] and [54].

3.3 Cebecci-Smith Algebraic Turbulence Model

Presented Cebbeci-Smith algebraic turbulence model has been taken from [51]. Cebecci-Smith algebraic turbulence model could be used to compute the turbulent viscosity ν_t. Domain Ω is divided into two subdomains. In the inner subdomain (near walls) the inner turbulent viscosity ν_{t_i} is computed. In the outer subdomain the outer turbulent viscosity ν_{t_o} is computed. Most common procedure is to compute both turbulent viscosities and then to use the minimal one:

$$\nu_t = \min \left(\nu_{t_i}, \nu_{t_o} \right). \tag{3.12}$$

For turbulent viscosity computing is necessary to use local systems of coordinates (X, Y). Where X is parallel with the nearest wall and Y is perpendicular to the nearest wall (distance from the wall). In the inner subdomain the turbulent viscosity is defined as follows:

$$\nu_{t_i} = L_m^2 \left| \frac{\partial U}{\partial Y} \right|, \tag{3.13}$$

where (U, V) are components of velocity vector in direction of (X, Y) and L_m is given by equation:

$$L_m = \kappa Y F_D, \tag{3.14}$$

where:

$$F_D = 1 - \exp \left(-\frac{1}{A^+} u_r Y Re \right), \tag{3.15}$$

u_r is so called friction velocity:

$$u_r = \left(\nu \left| \frac{\partial U}{\partial Y} \right| \right)_\omega^{\frac{1}{2}}. \tag{3.16}$$

In outer subdomain the turbulent viscosity is defined by Clauser's equation:

$$\nu_{t_o} = \rho \alpha \delta^* U_e F_k, \tag{3.17}$$

where:

$$F_k = \left[1 + 5.5\left(\frac{Y}{\delta}\right)^6\right]^{-1}, \ U_e = U(\delta) \tag{3.18}$$

and δ is the boundary layer thickness and:

$$\delta^* = \int_0^\delta \left(1 - \frac{U}{U_e}\right) dY. \tag{3.19}$$

Following values of the constants have been used:

$$\kappa = 0.4, \ \alpha = 0.0168, \ A^+ = 26. \tag{3.20}$$

3.4 Turbulent Kinetic Energy Transport Turbulence Models

Almost all the turbulence models apart from algebraic ones are based on turbulent kinetic energy k transport equation. There are mentioned two equations turbulence models based on turbulent kinetic energy k transport and turbulent kinetic energy dissipation rate ε transport in the following sections. The variant of $k - \varepsilon$ turbulence model for stratified flows in atmospheric boundary layer is also presented.

3.4.1 Standard k-ε Turbulence Model

The standard $k - \varepsilon$ turbulence model has been taken from [9]. Following equations are transport equations for turbulent kinetic energy k and for turbulent kinetic energy dissipation rate ε:

$$\frac{\partial k}{\partial t} + u_j \frac{\partial k}{\partial x_j} = \frac{\partial}{\partial x_j}\left[\left(\nu + \frac{\nu_t}{\sigma_k}\right)\frac{\partial k}{\partial x_j}\right] + P_k - \varepsilon, \tag{3.21}$$

$$\frac{\partial \varepsilon}{\partial t} + u_j \frac{\partial \varepsilon}{\partial x_j} = \frac{\partial}{\partial x_j}\left[\left(\nu + \frac{\nu_t}{\sigma_\varepsilon}\right)\frac{\partial \varepsilon}{\partial x_j}\right] + \frac{\varepsilon}{k}C_{\varepsilon 1}P_k - \frac{\varepsilon^2}{k}C_{\varepsilon 2}, \tag{3.22}$$

where P_k is production of turbulent kinetic energy for incompressible flow defined as follows:

$$P_k = 2\nu_t S_{ij}\frac{\partial \overline{u}_i}{\partial x_j}. \tag{3.23}$$

Turbulent viscosity is computed from following relation:

$$\nu_t = C_\mu \sqrt{k}L, \tag{3.24}$$

where L is the turbulent length scale defined by Rott's relation:

$$\varepsilon = \frac{k^{3/2}}{L} \Rightarrow L = \frac{k^{3/2}}{\varepsilon}. \tag{3.25}$$

hence

$$\nu_t = C_\mu \frac{k^2}{\varepsilon} \tag{3.26}$$

and model constants are:

$$C_\mu = 0.09, \ \sigma_k = 1.0, \ \sigma_\varepsilon = 1.3, \ C_{\varepsilon 1} = 1.44, \ C_{\varepsilon 2} = 1.92 \tag{3.27}$$

3.4.2 Realizable k-ε Turbulence Model

The model has been introduced in the article [33]. Transport equations for turbulent kinetic energy k and for turbulent kinetic energy dissipation rate ε for the realizable $k - \varepsilon$ turbulence model are:

$$\frac{\partial k}{\partial t} + u_j \frac{\partial k}{\partial x_j} = \frac{\partial}{\partial x_j}\left[\left(\nu + \frac{\nu_t}{\sigma_k}\right)\frac{\partial k}{\partial x_j}\right] + P_k - \varepsilon, \tag{3.28}$$

$$\frac{\partial \varepsilon}{\partial t} + u_j \frac{\partial \varepsilon}{\partial x_j} = \frac{\partial}{\partial x_j}\left[\left(\nu + \frac{\nu_t}{\sigma_\varepsilon}\right)\frac{\partial \varepsilon}{\partial x_j}\right] + C_{\varepsilon 1} S\varepsilon - C_{\varepsilon 2}\frac{\varepsilon^2}{k + \sqrt{\nu\varepsilon}}, \tag{3.29}$$

where $S = \sqrt{2S_{ij}S_{ij}}$.

Turbulent viscosity is computed from the same relation as in standard $k - \varepsilon$ model:

$$\nu_t = C_\mu \sqrt{k} L = C_\mu \frac{k^2}{\varepsilon}, \tag{3.30}$$

but the term C_μ is not constant in this model and is defined by a following relation:

$$C_\mu = \frac{1}{A_0 + A_s U^{(*)} k/\varepsilon}, \tag{3.31}$$

where:

$$U^{(*)} = \sqrt{S_{ij}S_{ij} + \Omega_{ij}\Omega_{ij}}, \tag{3.32}$$

$$\Omega_{ij} = \frac{1}{2}\left(\frac{\partial u_i}{\partial x_j} - \frac{\partial u_j}{\partial x_i}\right), \tag{3.33}$$

$$A_s = \sqrt{6}\cos\phi, \tag{3.34}$$

$$\phi = \frac{1}{3}\arccos(\sqrt{6}W), \tag{3.35}$$

$$W = \frac{S_{ij}S_{jk}S_{ki}}{\tilde{S}^3}, \tag{3.36}$$

$$\tilde{S} = \sqrt{S_{ij}S_{ij}}. \tag{3.37}$$

Also the term $C_{\varepsilon 1}$ is not constant any more in the realizable $k - \varepsilon$ turbulence model:

$$C_{\varepsilon 1} = \max\{0.43, \frac{\eta}{5 + \eta}\}, \tag{3.38}$$

where:

$$\eta = \frac{Sk}{\varepsilon}, \quad S = \sqrt{2S_{ij}S_{ij}}. \tag{3.39}$$

Constants of the model are set as follows:

$$\sigma_k = 1.0, \ \sigma_\varepsilon = 1.2, \ C_{\varepsilon 2} = 1.9, \ A_0 = 4.0 \tag{3.40}$$

3.4.3 Differences between Standard k-ε and Realizable k-ε Turbulence Models

The difference between the standard k-ε and the Realizable k-ε turbulence model is the fact that the standard k-ε turbulence model does not fulfill the realizability condition, i.e. that the shear stress (3.9) has to be non-negative:

$$\tau_{ij} = -\overline{u_i'' u_j''} = 2\nu_t S_{ij} - \frac{2}{3}k\delta_{ij} \geq 0 \tag{3.41}$$

Using the relation (3.30), the realizability condition (3.41) is fulfilled only if:

$$\frac{k}{\varepsilon}S_{ij} \geq \frac{1}{3C_\mu} = \frac{100}{27} \tag{3.42}$$

in case of standard k-ε turbulence model, where $C_\mu = 0.09$. Therefore C_μ is not constant in the Realizable k-ε model and holds the term $2\nu_t S_{ij}$ always greater or equal than the term $\frac{2}{3}k$.

3.4.4 Modification of k-ε turbulence model for stratified flow problems

There have been found several modifications of the standard $k - \varepsilon$ turbulence model. The first one have been published in [16] and [28]:

$$\frac{\partial k}{\partial t} + u_j \frac{\partial k}{\partial x_j} = \frac{\partial}{\partial x_j}\left[\left(\nu + \frac{\nu_t}{\sigma_k}\right)\frac{\partial k}{\partial x_j}\right] + P_k + G_k - \varepsilon, \tag{3.43}$$

$$\frac{\partial \varepsilon}{\partial t} + u_j \frac{\partial \varepsilon}{\partial x_j} = \frac{\partial}{\partial x_j}\left[\left(\nu + \frac{\nu_t}{\sigma_\varepsilon}\right)\frac{\partial \varepsilon}{\partial x_j}\right] + \frac{\varepsilon}{k}C_{\varepsilon 1}\left(P_k + C_{\varepsilon 3}G_k\right) - \frac{\varepsilon^2}{k}C_{\varepsilon 2}, \tag{3.44}$$

where G_k is a production of turbulent kinetic energy arisen from buoyancy effects and is given by:

$$G_k = \beta g \frac{\rho \nu_t}{Pr_t}\frac{\partial T}{\partial z}, \tag{3.45}$$

where Pr_t is the turbulent Prandtl number (3.46) and β is the coefficient of the thermal expansion (3.47).

$$Pr_t = \frac{\mu c_p}{\kappa}, \tag{3.46}$$

where κ is the coefficient of thermal conduction.

$$\beta = -\frac{1}{\rho}\left(\frac{\partial \rho}{\partial T}\right)_p \tag{3.47}$$

Assuming the ideal gas one can substitute β in the production of turbulent kinetic energy arisen from buoyancy effects (3.45) from (3.47) and one obtains:

$$G_k = -g\frac{\nu_t}{Pr_t}\frac{\partial \rho}{\partial z}. \tag{3.48}$$

In [16] has been presented a bit different formulation of G_k which is:

$$G_k = \beta g \frac{\nu_t}{\sigma_T}\frac{\partial T}{\partial z}, \tag{3.49}$$

where σ_T is constant and $\sigma_T = 1.0$
According to [16] and [28] the term $C_{\varepsilon 3}$ is defined as:

$$C_{\varepsilon 3} = \tanh\left|\frac{v}{u}\right|, \tag{3.50}$$

where u is the magnitude of velocity in the direction perpendicular to the gravity vector and v is the magnitude of velocity in the direction parallel to the gravity vector. One can see that the $C_{\varepsilon 3} = 1$ when the velocity vector is aligned with the direction of gravity and i.e. the buoyancy effect is maximized. On the other hand, when the flow is aligned

perpendicular to the gravity direction, then the term $C_{\varepsilon 3} = 0$ and the buoyancy effect disappears.

A slightly different model has been presented in [53] and [34]. Governing equations of the model are:

$$\frac{\partial k}{\partial t} + u_j \frac{\partial k}{\partial x_j} = \frac{\partial}{\partial x_j}\left[\left(\nu + \frac{\nu_t}{\sigma_k}\right)\frac{\partial k}{\partial x_j}\right] + P_k + G_k - \varepsilon, \tag{3.51}$$

$$\frac{\partial \varepsilon}{\partial t} + u_j \frac{\partial \varepsilon}{\partial x_j} = \frac{\partial}{\partial x_j}\left[\left(\nu + \frac{\nu_t}{\sigma_\varepsilon}\right)\frac{\partial \varepsilon}{\partial x_j}\right] + \frac{\varepsilon}{k}C_{\varepsilon 1}\left(1 + C_{\varepsilon 3}R_f\right)\left(P_k + G_k\right) - \frac{\varepsilon^2}{k}C_{\varepsilon 2} \tag{3.52}$$

where $R_f = -G_k/P_k$ and production of turbulent kinetic energy arisen from buoyancy effects G_k and the coefficient of the thermal expansion β are adjusted for potential temperature calculation instead of calculation with temperature in a following way:

$$G_k = -\beta g \frac{\nu_t}{\sigma_\Theta}\frac{\partial \Theta}{\partial z}, \tag{3.53}$$

$$\beta = -\frac{1}{\rho}\frac{\partial \rho}{\partial \Theta}, \tag{3.54}$$

where σ_Θ is constant $\sigma_\Theta = 1.0$. The term $C_{\varepsilon 3}$ is constant $C_{\varepsilon 3} = 0.7$. All other model constants are the same for all presented $k - \varepsilon$ type turbulence models:

$$C_\mu = 0.09, \quad \sigma_k = 1.0, \quad \sigma_\varepsilon = 1.3, \quad C_{\varepsilon 1} = 1.44, \quad C_{\varepsilon 2} = 1.92. \tag{3.55}$$

3.4.5 Near Wall Treatment

All the presented $k - \varepsilon$ type turbulence models are not valid in near wall regions due to anisotropy of the turbulence in these regions. This problem is typically solved by introduction of so called wall functions. Where the boundary condition for the variable is not prescribed on the wall but in the logarithmic domain of the law of the wall, which is for boundary layer with constant pressure when $30 < y^+ < 200$.

The turbulent kinetic energy transport turbulence models for buoyant flows, which model the turbulence also in near wall regions and do not use wall functions are presented in [32].

Part II

Numerical Solution

Chapter 4

Numerical Solution

Contents

The choice of the governing equations and the numerical model are presented in this chapter. All the numerical methods that has been chosen are introduced and their advantages and limitations are discussed.

4.1 Governing Equations

4.1.1 Turbulent stably stratified flows in atmospheric boundary layer

The first mathematical model that will be introduced in this section has been used for simulation of turbulent stratified atmospheric boundary layer flows. The system of incompressible Reynolds averaged Navier-Stokes (RANS) equations completed by the transport equation for density and coupled with this density equation by the source term in the momentum equation has been used:

$$\frac{\partial u_j}{\partial x_j} = 0, \tag{4.1}$$

$$\frac{\partial u_i}{\partial t} + u_j \frac{\partial u_i}{\partial x_j} = \frac{\partial}{\partial x_j}\left(\nu_e \frac{\partial u_i}{\partial x_j}\right) - \frac{1}{\rho_0}\frac{\partial p''}{\partial x_i} + \frac{\rho''}{\rho_0} g_i, \tag{4.2}$$

$$\frac{\partial \rho}{\partial t} + u_j \frac{\partial \rho}{\partial x_j} = 0, \tag{4.3}$$

where $\nu_e = \nu + \nu_t$ is the sum of laminar and turbulent kinematic viscosity, p'' and ρ'' are pressure and density perturbations and p_0 and ρ_0 are the reference pressure and density distributions, firstly defined in section 2.4.2.3:

$$p''(z) = p(z) - p_0(z), \tag{4.4}$$

$$\rho''(z) = \rho(z) - \rho_0(z). \tag{4.5}$$

This system (in conservative form) of Reynolds averaged Navier-Stokes equations has been used in a numerical model for all the computations of stratified flows that have been presented in this thesis, where the turbulent viscosity ν_t has been computed using algebraic turbulence model Cebecci-Smith.

It will be advantageous to introduce the vector form of previously mentioned RANS equations in conservative form at this place:

$$\mathbb{M} \cdot \mathbf{W}_t + \mathbf{F}_x + \mathbf{G}_y + \mathbf{H}_z = \mathbf{R}_x + \mathbf{S}_y + \mathbf{T}_z + \mathbf{K}, \tag{4.6}$$

where $\mathbb{M}$ is diagonal matrix with following entries:

$$\mathbb{M} = diag \parallel 0, \ 1, \ 1, \ 1, \ 1 \parallel, \tag{4.7}$$

$\mathbf{W}$ is a vector of conservative variables:

$$\mathbf{W} = \parallel p, \ u, \ v, \ w, \ \rho \parallel^T, \tag{4.8}$$

$\mathbf{F}, \mathbf{G}, \mathbf{H}$ are vectors of convective fluxes:

$$\mathbf{F} = \left\|\begin{array}{c} u \\ u^2 + p'' \\ u \cdot v \\ u \cdot w \\ u \cdot \rho \end{array}\right\|, \quad \mathbf{G} = \left\|\begin{array}{c} v \\ v \cdot u \\ v^2 + p'' \\ v \cdot w \\ v \cdot \rho \end{array}\right\|, \quad \mathbf{H} = \left\|\begin{array}{c} w \\ w \cdot u \\ w \cdot v \\ w^2 + p'' \\ w \cdot \rho \end{array}\right\|, \tag{4.9}$$

48

R, **S**, **T** are vectors of diffusive fluxes:

$$\mathbf{R} = \nu_e \left\| \begin{array}{c} 0 \\ u_x \\ v_x \\ w_x \\ 0 \end{array} \right\|, \quad \mathbf{S} = \nu_e \left\| \begin{array}{c} 0 \\ u_y \\ v_y \\ w_y \\ 0 \end{array} \right\|, \quad \mathbf{T} = \nu_e \left\| \begin{array}{c} 0 \\ u_z \\ v_z \\ w_z \\ 0 \end{array} \right\| \tag{4.10}$$

and **K** is the source term defined as follows in this case:

$$\mathbf{K} = \frac{\rho''}{\rho_0} \left\| \, 0, \ 0, \ 0, \ -g, \ 0 \, \right\|^T . \tag{4.11}$$

The subscripts $_t$ and $_x$ $_y$ $_z$ denotes the derivative with respect to time $\partial/\partial t$ and the derivative with respect to space coordinates $\partial/\partial x$, $\partial/\partial y$, $\partial/\partial z$.

4.1.2 Turbulent neutrally stratified flows in atmospheric boundary layer

The second model that has been used for simulation of neutrally stratified turbulent flows in atmospheric boundary layer is the system of incompressible Reynolds averaged Navier-Stokes completed by standard $k-\varepsilon$ turbulence model used for the computation of turbulent viscosity (the system has been used in conservative form):

$$\frac{\partial u_j}{\partial x_j} = 0, \tag{4.12}$$

$$\frac{\partial u_i}{\partial t} + u_j \frac{\partial u_i}{\partial x_j} = \frac{\partial}{\partial x_j}\left((\nu + \nu_t)\frac{\partial u_i}{\partial x_j} \right) - \frac{1}{\rho_0}\frac{\partial p}{\partial x_i}, \tag{4.13}$$

$$\frac{\partial k}{\partial t} + u_j \frac{\partial k}{\partial x_j} = \frac{\partial}{\partial x_j}\left[\left(\nu + \frac{\nu_t}{\sigma_k}\right)\frac{\partial k}{\partial x_j} \right] + P_k - \varepsilon, \tag{4.14}$$

$$\frac{\partial \varepsilon}{\partial t} + u_j \frac{\partial \varepsilon}{\partial x_j} = \frac{\partial}{\partial x_j}\left[\left(\nu + \frac{\nu_t}{\sigma_\varepsilon}\right)\frac{\partial \varepsilon}{\partial x_j} \right] + \frac{\varepsilon}{k}C_{\varepsilon 1}P_k - \frac{\varepsilon^2}{k}C_{\varepsilon 2}, \tag{4.15}$$

Let me introduce a conservative vector form of the previously stated system at this place:

$$\mathbb{M} \cdot \mathbf{W}_t + \mathbf{F}_x + \mathbf{G}_y + \mathbf{H}_z = \mathbf{R}_x + \mathbf{S}_y + \mathbf{T}_z + \mathbf{K}, \tag{4.16}$$

where $\mathbb{M}$ is diagonal matrix with following entries:

$$\mathbb{M} = diag \left\| \, 0, \ 1, \ 1, \ 1, \ 1, \ 1 \, \right\|, \tag{4.17}$$

W is a vector of conservative variables:

$$\mathbf{W} = \left\| \, p, \ u, \ v, \ w, \ k, \ \varepsilon \, \right\|^T , \tag{4.18}$$

F, **G**, **H** are vectors of convective fluxes:

$$\mathbf{F} = \left\| \begin{array}{c} u \\ u^2 + p \\ u \cdot v \\ u \cdot w \\ u \cdot k \\ u \cdot \varepsilon \end{array} \right\|, \quad \mathbf{G} = \left\| \begin{array}{c} v \\ v \cdot u \\ v^2 + p \\ v \cdot w \\ v \cdot k \\ v \cdot \varepsilon \end{array} \right\|, \quad \mathbf{H} = \left\| \begin{array}{c} w \\ w \cdot u \\ w \cdot v \\ w^2 + p \\ w \cdot k \\ w \cdot \varepsilon \end{array} \right\|, \tag{4.19}$$

R, **S**, **T** are vectors of diffusive fluxes:

$$
\mathbf{R} = \left\| \begin{array}{c} 0 \\ \nu_e \cdot u_x \\ \nu_e \cdot v_x \\ \nu_e \cdot w_x \\ \nu_{ek} \cdot k_x \\ \nu_{e\varepsilon} \cdot \varepsilon_x \end{array} \right\|, \quad
\mathbf{S} = \left\| \begin{array}{c} 0 \\ \nu_e \cdot u_y \\ \nu_e \cdot v_y \\ \nu_e \cdot w_x \\ \nu_{ek} \cdot k_x \\ \nu_{e\varepsilon} \cdot \varepsilon_y \end{array} \right\|, \quad
\mathbf{T} = \left\| \begin{array}{c} 0 \\ \nu_e \cdot u_z \\ \nu_e \cdot v_z \\ \nu_e \cdot w_x \\ \nu_{ek} \cdot k_x \\ \nu_{e\varepsilon} \cdot \varepsilon_z \end{array} \right\|,
\tag{4.20}
$$

and **K** is the source term defined as follows in this case:

$$
\mathbf{K} = \left\| \begin{array}{c} 0 \\ 0 \\ 0 \\ 0 \\ P_k - \varepsilon \\ \frac{\varepsilon}{k} C_{\varepsilon 1} P_k - \frac{\varepsilon^2}{k} C_{\varepsilon 2} \end{array} \right\|.
\tag{4.21}
$$

where

$$
\nu_e = \nu + \nu_t,
\tag{4.22}
$$

$$
\nu_{ek} = \nu + \frac{\nu_t}{\sigma_k},
\tag{4.23}
$$

$$
\nu_{e\varepsilon} = \nu + \frac{\nu_t}{\sigma_\varepsilon}.
\tag{4.24}
$$

4.2 Artificial Compressibility Method

The artificial compressibility method is one of the pressure velocity coupling methods for incompressible flows. This method has firstly used by Chorin in 1967 [25].

The artificial compressibility method lies in adding the term with the time derivative of pressure into the continuity equation. Following equation is used instead of incompressible continuity equation e.g. in the form (4.1):

$$
\frac{1}{\tilde{\beta}^2} \frac{\partial p}{\partial t} + \frac{\partial u_j}{\partial x_j} = 0,
\tag{4.25}
$$

where $\tilde{\beta} \in \mathbb{R}^+$ is the artificial speed of sound. The method like it is presented is valid only for steady state solutions, because only in steady state holds:

$$
\frac{\partial p}{\partial t} = 0
\tag{4.26}
$$

Using artificial compressibility method the system (4.6) comes into following:

$$
\tilde{\mathbb{M}} \cdot \mathbf{W}_t + \mathbf{F}_x + \mathbf{G}_y + \mathbf{H}_z = \mathbf{R}_x + \mathbf{S}_y + \mathbf{T}_z + \mathbf{K},
\tag{4.27}
$$

where

$$
\tilde{\mathbb{M}} = diag \left\| \frac{1}{\tilde{\beta}^2}, \ 1, \ 1, \ 1, \ 1, \ 1 \right\|.
\tag{4.28}
$$

Let's consider now only the inviscid part of governing equations (4.27) without any source term multiplied by $\tilde{\mathbb{M}}^{-1}$ from left side:

$$
\mathbf{W}_t + \tilde{\mathbb{M}}^{-1} \cdot (\mathbf{F}_x + \mathbf{G}_y + \mathbf{H}_z) = 0,
\tag{4.29}
$$

i.e. that the continuity equation (4.25) become:

$$\frac{\partial p}{\partial t} + \tilde{\beta}^2 \frac{\partial u_j}{\partial x_j} = 0, \tag{4.30}$$

and let's consider just a continuity equation in the form (4.30) and the inviscid part of the incompressible momentum equation (4.2) for simplicity.

Because one can say that inviscid fluxes **F**, **G**, **H** are functions of conservative variables then one can express equation (4.29) in a following way:

$$\frac{\partial \mathbf{W}}{\partial t} + \mathbb{A}\frac{\partial \mathbf{W}}{\partial x} + \mathbb{B}\frac{\partial \mathbf{W}}{\partial y} + \mathbb{C}\frac{\partial \mathbf{W}}{\partial z} = 0, \tag{4.31}$$

where $\mathbb{A}$, $\mathbb{B}$, $\mathbb{C}$ are Jacobi matrices of inviscid fluxes

$$\mathbb{A} = \frac{\partial \mathbf{F}}{\partial \mathbf{W}} = \begin{pmatrix} 0 & \tilde{\beta}^2 & 0 & 0 \\ 1 & 2u & 0 & 0 \\ 0 & v & u & 0 \\ 0 & w & 0 & u \end{pmatrix}, \tag{4.32}$$

$$\mathbb{B} = \frac{\partial \mathbf{G}}{\partial \mathbf{W}} = \begin{pmatrix} 0 & 0 & \tilde{\beta}^2 & 0 \\ 0 & v & u & 0 \\ 1 & 0 & 2v & 0 \\ 0 & 0 & w & v \end{pmatrix}, \tag{4.33}$$

$$\mathbb{C} = \frac{\partial \mathbf{H}}{\partial \mathbf{W}} = \begin{pmatrix} 0 & 0 & 0 & \tilde{\beta}^2 \\ 0 & w & 0 & u \\ 0 & 0 & w & v \\ 1 & 0 & 0 & 2w \end{pmatrix}. \tag{4.34}$$

$$\mathbb{F} = \omega_1\mathbb{A} + \omega_2\mathbb{B} + \omega_3\mathbb{C} = \begin{pmatrix} 0 & \omega_1\tilde{\beta}^2 & \omega_2\tilde{\beta}^2 & \omega_3\tilde{\beta}^2 \\ \omega_1 & 2\omega_1 u_+\omega_2 v + \omega_3 w & \omega_2 u & \omega_3 u \\ \omega_2 & \omega_1 v & \omega_1 u_+ 2\omega_2 v + \omega_3 w & \omega_3 v \\ \omega_3 & \omega_1 w & \omega_2 w & \omega_1 u_+\omega_2 v + 2\omega_3 w \end{pmatrix}.$$

Eigenvalues of the matrix $\mathbb{F}$ are:

$$\begin{aligned} \lambda_{1,2} &= \omega_1 u + \omega_2 v + \omega_3 w \\ \lambda_{3,4} &= \omega_1 u + \omega_2 v + \omega_3 w \pm \sqrt{(\omega_1 u + \omega_2 v + \omega_3 w)^2 + \tilde{\beta}^2} \end{aligned}$$

All the eigenvalues do not depend on choice of ω_1, ω_2, ω_3 and all are real. It means that the inviscid part of modified Navier-Stokes equations (4.31) is fully hyperbolic and can be solved by standard methods for hyperbolic conservation laws.

4.3 Finite Volume Method

Finite volume method is a spatial discretization method for solving partial differential equations. This method had been used for discretization of CFD problems for a first time by McDonald (1971) [31] and by MacCormack and Pullay (1972) [29]. The name of

the method comes from the fact, that the the computational domain is divided into the finite number of volumes, that have an empty intersection but the union of all these finite volumes is the whole domain.

Lets denote the domain Ω, its finite volumes Ω_i and A the set of all indices of finite volumes, then the following has to be satisfied in order to use finite volume method:

$$\Omega = \bigcup_{i \in A} \Omega_i \tag{4.35}$$

$$\Omega_i \bigcap \Omega_j = \varnothing \text{ for } i,\, j \in A,\ i \neq j \tag{4.36}$$

The method is based on the integral formulation of the conservation laws. The main idea is that the integral form of conservation laws has to be satisfied in each finite volume of the domain. It allows to discretize the domain to finite number of volumes in the most suitable way according to the shape of the computational domain without changing the exact formulation of the method. The method could be used on structured orthogonal, structured non-orthogonal and completely unstructured computational grids.
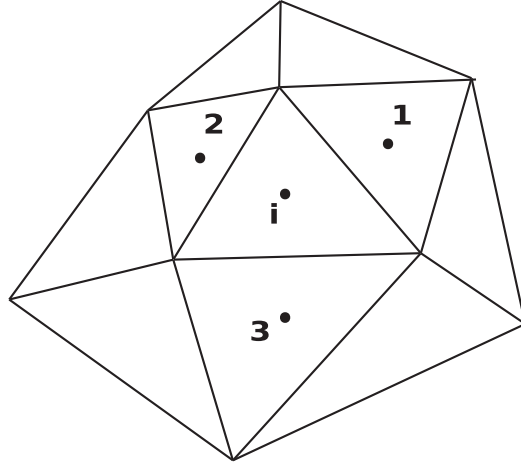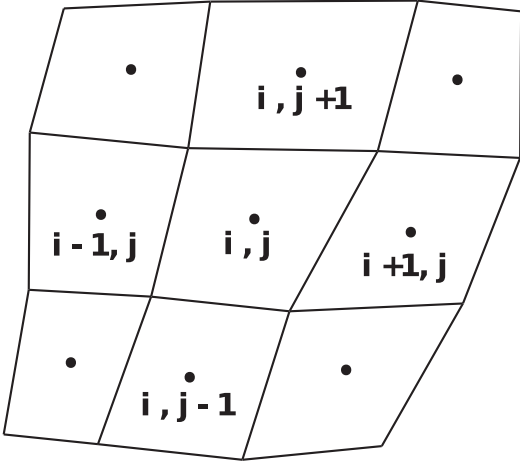
Figure 4.1: Structured grid example   **Figure 4.2:** Unstructured grid example

The integral form of conservation law for a scalar variable U with volume sources/sinks Q on the domain Ω can be expressed by a following integral equation:

$$\frac{\partial}{\partial t} \int_{\Omega} U \, d\Omega + \oint_{\partial \Omega} F \, dS = \int_{\Omega} Q \, d\Omega, \tag{4.37}$$

where F is the flux of the variable U through the boundary of the domain $\partial \Omega$.

Lets suppose that the domain Ω is divided into two subdomains Ω_1 and Ω_2 (see figure (4.3)), and simultaneously holds the (4.35) and (4.36) for those two subdomains. Then one can write the integral equation for the conservation of U for each subdomain independently:

$$\frac{\partial}{\partial t} \int_{\Omega_1} U \, d\Omega + \oint_{ABC} F \, dS \;=\; \int_{\Omega_1} Q \, d\Omega, \tag{4.38}$$

$$\frac{\partial}{\partial t} \int_{\Omega_2} U \, d\Omega + \oint_{BDC} F \, dS \;=\; \int_{\Omega_2} Q \, d\Omega. \tag{4.39}$$

Surface integrals over the new boundary **BC** appear twice the same in absolute value, but with different signs, so the sum of them is zero. This property is called conservation
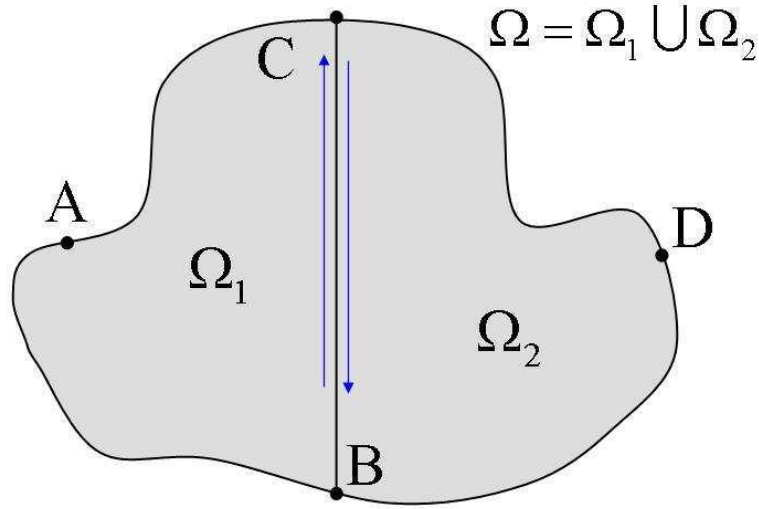
Figure 4.3: Conservation property of the finite volume method

and should be satisfied by the numerical discretization of the fluxes. If numerical scheme satisfies the conservativeness then it is called conservative scheme. When the scheme is non-conservative, then the numerical sources are rising there from the inequalities of fluxes from the neighboring cells and the computation is less stable and less accurate than the computation with the conservative ones.

4.4 Spatial discretization

The spatial discretization for the governing equations presented in sections 4.1.1 and 4.1.2 will be derived using the finite volume method and the artificial compressibility method. The spatial discretization will be derived in so called cell center form. It means that the resulting values are located in cell centers (center of gravity of the cell) of the computational mesh.

Lets take the system (4.6) or (4.29) and lets integrate it over the one of the finite volumes Ω_i:

$$\iiint_{\Omega_i} \tilde{\mathbb{M}} \cdot \mathbf{W}_t d\Omega + \iiint_{\Omega_i} (\mathbf{F}_x + \mathbf{G}_y + \mathbf{H}_z)\, d\Omega = \iiint_{\Omega_i} (\mathbf{R}_x + \mathbf{S}_y + \mathbf{T}_z)\, d\Omega + \iiint_{\Omega_i} \mathbf{K} d\Omega. \tag{4.40}$$

Applying the mean value theorem on the first and last integral from equation (4.40) one obtains the mean values of the conservative variables and source terms in the finite volumes Ω_i:

$$\mathbf{W}_i = \mathbf{W}_i(t) \;=\; \frac{1}{V_i} \iiint_{\Omega_i} \tilde{\mathbb{M}} \cdot \mathbf{W}(x,\, y,\, z,\, t) d\Omega, \tag{4.41}$$

$$\mathbf{K}_i = \mathbf{K}_i(t) \;=\; \frac{1}{V_i} \iiint_{\Omega_i} \mathbf{K}(x,\, y,\, z,\, t) d\Omega. \tag{4.42}$$

Lets make a substitution in equation (4.40) using these two last-defined relations:

$$\frac{d\mathbf{W}_i}{dt} = -\frac{1}{V_i}\iiint_{\Omega_i}(\mathbf{F}_x + \mathbf{G}_y + \mathbf{H}_z)\,d\Omega + \frac{1}{V_i}\iiint_{\Omega_i}(\mathbf{R}_x + \mathbf{S}_y + \mathbf{T}_z)\,d\Omega + \mathbf{K}_i, \quad (4.43)$$

and lets put all the rest integrals under one integral:

$$\frac{d\mathbf{W}_i}{dt} = -\frac{1}{V_i}\iiint_{\Omega_i}[(\mathbf{F}-\mathbf{R})_x + (\mathbf{G}-\mathbf{S})_y + (\mathbf{H}-\mathbf{T})_z]\,d\Omega + \mathbf{K}_i, \quad (4.44)$$

Now, lets use a Green-Gauss theorem to transform the last volume integral into the surface integral:

$$\frac{d\mathbf{W}_i}{dt} = -\frac{1}{V_i}\oint_{\partial\Omega_i}[(\mathbf{F}-\mathbf{R})_x + (\mathbf{G}-\mathbf{S})_y + (\mathbf{H}-\mathbf{T})_z]\,\vec{n}dS + \mathbf{K}_i, \quad (4.45)$$

where $\vec{n}$ is the outer normal vector and the S is the surface of the finite volume boundary $\partial\Omega_i$. Applying the space discretization to the surface integral from the last-mentioned equation, one obtains following:

$$\oint_{\partial\Omega_i}[(\mathbf{F}-\mathbf{R})_x + (\mathbf{G}-\mathbf{S})_y + (\mathbf{H}-\mathbf{T})_z]\,\vec{n}dS = \sum_{j\in A_i}(\tilde{\mathbf{F}}_{ij}-\tilde{\mathbf{R}}_{ij},\ \tilde{\mathbf{G}}_{ij}-\tilde{\mathbf{S}}_{ij},\ \tilde{\mathbf{H}}_{ij}-\tilde{\mathbf{T}}_{ij})\vec{n}_{ij}\Delta S_{ij},$$
$$(4.46)$$

where $\tilde{\mathbf{F}}$, $\tilde{\mathbf{G}}$, $\tilde{\mathbf{H}}$ are numerical convective fluxes and $\tilde{\mathbf{R}}$, $\tilde{\mathbf{S}}$, $\tilde{\mathbf{T}}$ are numerical diffusive fluxes, $\vec{n}_{ij}$ is the outer normal of the j$^{\text{th}}$ face of the i$^{\text{th}}$ cell and ΔS_{ij} is the surface if the j$^{\text{th}}$ face of the i$^{\text{th}}$ cell and A_i is the set of neighbor cell indices of the i$^{\text{th}}$ cell.

Let's substitute the surface integral in (4.45) by the sum from (4.46) and write the resulting equation:

$$\frac{d\mathbf{W}_i}{dt} = -\frac{1}{V_i}\sum_{j\in A_i}(\tilde{\mathbf{F}}_{ij}-\tilde{\mathbf{R}}_{ij},\ \tilde{\mathbf{G}}_{ij}-\tilde{\mathbf{S}}_{ij},\ \tilde{\mathbf{H}}_{ij}-\tilde{\mathbf{T}}_{ij})\vec{n}_{ij}\Delta S_{ij} + \tilde{\mathbf{K}}_i. \quad (4.47)$$

One can see that the last mentioned equation is the ordinary differential equation for the i$^{\text{th}}$ cell of the finite volume grid. The time discretization method should be applied in order to obtain the fully discretized system of equations solvable by computer.

4.4.1 Convective fluxes

Evaluation of the numerical convective fluxes on the boundary (face) of the cell is usually done by the averaging of the convective fluxes computed in the cell centers:

$$\tilde{\mathbf{F}}_{ij} = \frac{1}{2}(\mathbf{F}_i + \mathbf{F}_j), \quad (4.48)$$

$$\tilde{\mathbf{G}}_{ij} = \frac{1}{2}(\mathbf{G}_i + \mathbf{G}_j), \quad (4.49)$$

$$\tilde{\mathbf{H}}_{ij} = \frac{1}{2}(\mathbf{H}_i + \mathbf{H}_j). \quad (4.50)$$

Another approach is applicable on the structured computational grids. This approach is used in further mentioned MacCormack scheme (two stage scheme - predictor corrector type scheme). It lies in the computation of the convective fluxes in a forward direction in a predictor step and in a backward direction in a corrector step. Combination of predictor and corrector step guarantees that the fluxes are computed and averaged from both sides

of the cell face (see figure (4.4)).

Numerical fluxes for MacCormack scheme (superscript ^{p} denotes predictor, ^{c} denotes corrector):

$$\tilde{\mathbf{F}}_1^p = \mathbf{F}_{i+1,j}, \ \tilde{\mathbf{F}}_2^p = \mathbf{F}_{i,j+1}, \ \tilde{\mathbf{F}}_3^p = \mathbf{F}_{i,j}, \ \tilde{\mathbf{F}}_4^p = \mathbf{F}_{i,j}, \tag{4.51}$$

$$\tilde{\mathbf{G}}_1^p = \mathbf{G}_{i+1,j}, \ \tilde{\mathbf{G}}_2^p = \mathbf{G}_{i,j+1}, \ \tilde{\mathbf{G}}_3^p = \mathbf{G}_{i,j}, \ \tilde{\mathbf{G}}_4^p = \mathbf{G}_{i,j}, \tag{4.52}$$

$$\tilde{\mathbf{H}}_1^p = \mathbf{H}_{i+1,j}, \ \tilde{\mathbf{H}}_2^p = \mathbf{H}_{i,j+1}, \ \tilde{\mathbf{H}}_3^p = \mathbf{H}_{i,j}, \ \tilde{\mathbf{H}}_4^p = \mathbf{H}_{i,j} \tag{4.53}$$

$$\tilde{\mathbf{F}}_1^c = \mathbf{F}_{i,j}, \ \tilde{\mathbf{F}}_2^c = \mathbf{F}_{i,j}, \ \tilde{\mathbf{F}}_3^c = \mathbf{F}_{i-1,j}, \ \tilde{\mathbf{F}}_4^c = \mathbf{F}_{i,j-1}, \tag{4.54}$$

$$\tilde{\mathbf{G}}_1^c = \mathbf{G}_{i,j}, \ \tilde{\mathbf{G}}_2^c = \mathbf{G}_{i,j}, \ \tilde{\mathbf{G}}_3^c = \mathbf{G}_{i-1,j}, \ \tilde{\mathbf{G}}_4^c = \mathbf{G}_{i,j-1}, \tag{4.55}$$

$$\tilde{\mathbf{H}}_1^c = \mathbf{H}_{i,j}, \ \tilde{\mathbf{H}}_2^c = \mathbf{H}_{i,j}, \ \tilde{\mathbf{H}}_3^c = \mathbf{H}_{i-1,j}, \ \tilde{\mathbf{H}}_4^c = \mathbf{H}_{i,j-1} \tag{4.56}$$
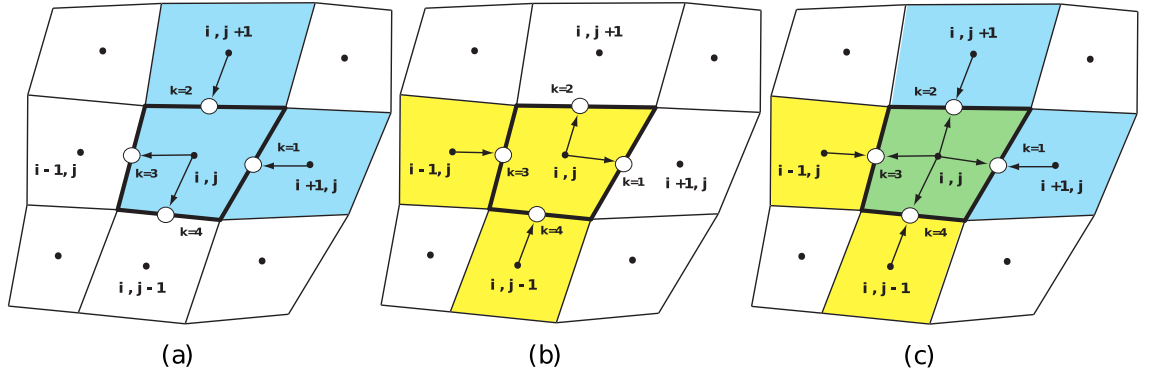
Figure 4.4: Stencil for inviscid fluxes computation, (a) predictor step, (b) corrector step, (c) predictor + corrector

Both the methods for computation of the numerical flux mentioned above are called central schemes. The computation of fluxes in the first case (see relations (4.48) (4.49) (4.50)) is done centrally at the first sight. The MacCormack scheme is also the central scheme due to the fact that it averages the forward and backward flux computation. Central schemes usually oscillates in the regions where the high gradients appear and some so called artificial dissipation has to be added in order to stabilize the solution. Instead of central schemes there could be used the upwind type schemes that do not need to add the artificial dissipation because it contains the artificial dissipation within itself.

4.4.2 Diffusive fluxes

It is necessary to know the spatial derivatives of the velocity components on the cell faces for the computation of diffusive (viscous) fluxes. One can compute their values by integration over the cells of so called dual grid. Lets consider now a structured haxahedral mesh in 3D. The dual mesh in 3D structured grid case consists of octahedral diamond shaped control volumes (see figure (4.5)).
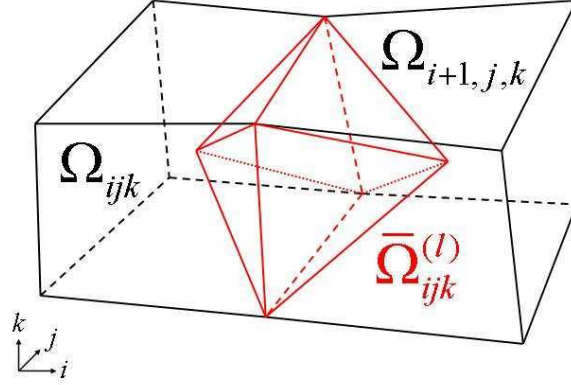
Figure 4.5: Stencil for viscous fluxes computation 3D (dual cells)

Dual volume cells have a centers in a face centers of original cells and their vertices are located in vertices of original cells and in original cell centers. One can use a mean value theorem for computations of the spatial derivative of velocity components. For example for the computation of the x velocity derivative u with respect to the x coordinate in the center of the dual volume cell $\overline{\Omega}_{ijk}^{(l)}$:

$$u_x|_{ijk}^{(l)} = \frac{1}{\overline{V}_{ijk}^{(l)}} \iiint_{\overline{\Omega}_{ijk}^{(l)}} u_x(x,\, y,\, z) d\overline{\Omega} \quad l = 1, ..., 6, \tag{4.57}$$

applying the Green-Gauss theorem on previously mentioned integral equation one obtains:

$$\iiint_{\overline{\Omega}_{ijk}^{(l)}} u_x(x,\, y,\, z) d\overline{\Omega} = \oint_{\partial\overline{\Omega}_{ijk}^{(l)}} u \cdot n_x d\overline{S} \approx \sum_{k=1}^{8} \tilde{u}_k^{(l)} \Delta \overline{S}_{xk}^{(l)} \quad l = 1, ..., 6 \tag{4.58}$$

where $\tilde{u}_k^{(l)}$ is the approximation of the x velocity u on the k$^{\text{th}}$ face of the dual cell related to the l$^{\text{th}}$ face of the original cell. $\Delta\overline{S}_{xk}^{(l)}$ is the projection in x direction of the surface of the k$^{\text{th}}$ face of the dual cell related to the l$^{\text{th}}$ face of the original cell. The discretized expression of the evaluation of the derivative of the x velocity u with respect to x coordinate could be written as follows:

$$u_x|_{ijk}^{(l)} = \frac{1}{\overline{V}_{ijk}^{(l)}} \sum_{k=1}^{8} \tilde{u}_k^{(l)} \Delta \overline{S}_{xk}^{(l)} \quad l = 1, ..., 6, \tag{4.59}$$

similarly for other spatial derivatives:

$$u_y|_{ijk}^{(l)} = \frac{1}{\overline{V}_{ijk}^{(l)}} \sum_{k=1}^{8} \tilde{u}_k^{(l)} \Delta \overline{S}_{yk}^{(l)}, \tag{4.60}$$

$$u_z|_{ijk}^{(l)} = \frac{1}{\overline{V}_{ijk}^{(l)}} \sum_{k=1}^{8} \tilde{u}_k^{(l)} \Delta \overline{S}_{zk}^{(l)}. \tag{4.61}$$

56

4.5 Time discretization

There have been discretized the spatial derivatives in the previous sections. Let's remember the equation (4.47):

$$\frac{d\mathbf{W}_i}{dt} = -\frac{1}{V_i} \sum_{j \in A_i} (\tilde{\mathbf{F}}_{ij} - \tilde{\mathbf{R}}_{ij}, \tilde{\mathbf{G}}_{ij} - \tilde{\mathbf{S}}_{ij}, \tilde{\mathbf{H}}_{ij} - \tilde{\mathbf{T}}_{ij}) \vec{n}_{ij} \Delta S_{ij} + \tilde{\mathbf{K}}_i, \qquad (4.62)$$

that is the ordinary differential equation for the i$^{\text{th}}$ cell of the finite volume grid. Let me introduce now the two time discretization methods that have been used in computations of results that are presented in the following part of this thesis. They are the well known Runge-Kutta method and the Lax-Wendroff scheme in MacCormack form. All the numerical convective and diffusive fluxes are functions of the conservative variables. So let's denote the sum from (4.62) as follows:

$$\mathbf{L}(\mathbf{W}_{ij}) = \frac{1}{V_i} \sum_{j \in A_i} (\tilde{\mathbf{F}}_{ij} - \tilde{\mathbf{R}}_{ij}, \tilde{\mathbf{G}}_{ij} - \tilde{\mathbf{S}}_{ij}, \tilde{\mathbf{H}}_{ij} - \tilde{\mathbf{T}}_{ij}) \vec{n}_{ij} \Delta S_{ij} + \tilde{\mathbf{K}}_i. \qquad (4.63)$$

The forward Euler discretization of the time derivative has been considered in all cases:

$$\frac{d\mathbf{W}_i}{dt} \approx \frac{\mathbf{W}_i^{n+1} - \mathbf{W}_i^n}{\Delta t} \qquad (4.64)$$

4.5.1 Multistage Runge-Kutta method

The multistage Runge-Kutta scheme could be written in a following form:

$$\begin{aligned}
\mathbf{W}_{ij}^0 &= \mathbf{W}_{ij}^n, \\
\mathbf{W}_{ij}^{r+1} &= \mathbf{W}_{ij}^0 - \alpha_{(r)} \Delta t \, \mathbf{L}(\mathbf{W}_{ij}^{(r)}), \\
\mathbf{W}_{ij}^{n+1} &= \mathbf{W}_{ij}^m,
\end{aligned} \qquad (4.65)$$

where r is the stage index $r \in 0, ..., m-1$, where m is the number of stages. $\alpha_{(r)}$ is constant different for each stage. Usually the 3-stage or 4-stage Runge-Kutta scheme is used with following $\alpha_{(r)}$:

$$\alpha_{(1)} = \frac{1}{2}, \ \alpha_{(2)} = \frac{1}{2}, \ \alpha_{(3)} = 1, \qquad (4.66)$$

for 3-stage Runge-Kutta scheme and:

$$\alpha_{(1)} = \frac{1}{4}, \ \alpha_{(2)} = \frac{1}{3}, \ \alpha_{(3)} = \frac{1}{2}, \ \alpha_{(4)} = 1, \qquad (4.67)$$

for 4-stage Runge-Kutta scheme.

4.5.2 Lax-Wendroff (MacCormack) scheme

Lax-Wendroff predictor-corrector scheme (MacCormack form) firstly presented in [30] has been used in a following form:

$$\begin{aligned}
\mathbf{W}_i^{n+\frac{1}{2}} &= \mathbf{W}_i^n - \Delta t \, \mathbf{L}(\mathbf{W}_{ij}^n), &(4.68) \\
\mathbf{W}_i^{n+1} &= \frac{1}{2}(\mathbf{W}_i^{n+\frac{1}{2}} + \mathbf{W}_i^n) - \frac{\Delta t}{2} \mathbf{L}(\mathbf{W}_{ij}^{n+\frac{1}{2}}). &(4.69)
\end{aligned}$$

4.6 Artificial dissipation (viscosity)

When the discretization of convective fluxes is based on the central differencing the so called artificial dissipation (diffusion, viscosity) has to be introduced in order to damp the spurious oscillations in solution. These oscillations usually appear in the regions with high gradients and if they are not damped, they can spread all over the domain and can completely destroy the solution. The Jameson's type artificial dissipation has been used as it was presented in [12]. For simplicity let's suppose the hexahedral structured grid, then the artificial dissipation will be defined as follows:

$$\mathbf{DW}_{i,j,k} = \mathbf{D}_x \mathbf{W}^r_{i,j,k} + \mathbf{D}_y \mathbf{W}^r_{i,j,k} + \mathbf{D}_z \mathbf{W}^r_{i,j,k}, \tag{4.70}$$

where

$$
\begin{aligned}
\mathbf{D}_x(\mathbf{W}^r_{i,j,k}) &= \varepsilon^{(2)}_{x_i} \left(\mathbf{W}^r_{i+1,j,k} - 2\mathbf{W}^r_{i,j,k} + \mathbf{W}^r_{i-1,j,k} \right) + \\
&= \varepsilon^{(4)}_{x_i} \left(\mathbf{W}^r_{i+2,j,k} - 4\mathbf{W}^r_{i+1,j,k} + 6\mathbf{W}^r_{i,j,k} - 4\mathbf{W}^r_{i-1,j,k} + \mathbf{W}^r_{i-2,j,k} \right),
\end{aligned} \tag{4.71}
$$

$$
\begin{aligned}
\mathbf{D}_y(\mathbf{W}^r_{i,j,k}) &= \varepsilon^{(2)}_{y_i} \left(\mathbf{W}^r_{i,j+1,k} - 2\mathbf{W}^r_{i,j,k} + \mathbf{W}^r_{i,j-1,k} \right) + \\
&= \varepsilon^{(4)}_{y_i} \left(\mathbf{W}^r_{i,j+2,k} - 4\mathbf{W}^r_{i,j+1,k} + 6\mathbf{W}^r_{i,j,k} - 4\mathbf{W}^r_{i,j-1,k} + \mathbf{W}^r_{i,j-2,k} \right),
\end{aligned} \tag{4.72}
$$

$$
\begin{aligned}
\mathbf{D}_z(\mathbf{W}^r_{i,j,k}) &= \varepsilon^{(2)}_{z_i} \left(\mathbf{W}^r_{i,j,k+1} - 2\mathbf{W}^r_{i,j,k} + \mathbf{W}^r_{i,j,k-1} \right) + \\
&= \varepsilon^{(4)}_{z_i} \left(\mathbf{W}^r_{i,j,k+2} - 4\mathbf{W}^r_{i,j,k+1} + 6\mathbf{W}^r_{i,j,k} - 4\mathbf{W}^r_{i,j,k-1} + \mathbf{W}^r_{i,j,k-2} \right),
\end{aligned} \tag{4.73}
$$

where the coefficients e.g. in x direction $\varepsilon^{(2)}_{x_i}$ and $\varepsilon^{(4)}_{x_i}$ are defined as follows:

$$\varepsilon^{(2)}_{x_i} = k_1 \cdot \gamma_{i,j,k},$$

$$\varepsilon^{(4)}_{x_i} = k_2 \max(0, \ (k_3 - \tilde{\varepsilon}^1_{x_i})), \quad \tilde{\varepsilon}^1_{x_i} = \max(\gamma_{i-1,j,k}, \ \gamma_{i,j,k}, \ \gamma_{i+1,j,k}),$$

and

$$\gamma_{i,j,k} = \frac{|p_{i+1,j,k} - 2p_{i,j,k} + p_{i-1,j,k}|}{|p_{i+1,j,k} + 2p_{i,j,k} + p_{i-1,j,k}|},$$

k_1, k_2 k_3 are experimentally tuned constants.
Using the artificial dissipation the residual operator $\mathbf{L}(\mathbf{W}^r_{i,j,k})$ is substituted in the previously mentioned numerical schemes by the $\tilde{\mathbf{L}}(\mathbf{W}^r_{i,j,k})$ operator, which is defined as follows:

$$\tilde{\mathbf{L}}(\mathbf{W}^r_{i,j,k}) = \mathbf{L}(\mathbf{W}^r_{i,j,k}) + \mathbf{D}(\mathbf{W}^r_{i,j,k}). \tag{4.74}$$

4.7 Stability condition

The presented explicit schemes are only conditionally stable. It has to satisfy the stability condition for explicit schemes, which is valid only for regular orthogonal computational grids:

$$\Delta t \leq \min_{\Omega_i, i \in A} \frac{CFL}{\frac{\rho_A}{\Delta x} + \frac{\rho_B}{\Delta y} + \frac{\rho_C}{\Delta z} + \frac{1}{Re} \left(\frac{1}{\Delta x^2} + \frac{1}{\Delta y^2} + \frac{1}{\Delta z^2} \right)} \tag{4.75}$$

where $CFL = 2$ (Courant-Fridrichs-Levy number) in case of 3-stage Runge-Kutta scheme with coefficients $\alpha = (1/2, 1/2, 1)$, $CFL = 2 \cdot \sqrt{2}$ in case of 4-stage Runge-Kutta scheme

with coefficients $\alpha = (1/4, 1/3, 1/2, 1)$ and $CFL = 1$ in case of Lax-Wendroff (MacCormack form) scheme and ρ_A, ρ_B, ρ_C are spectral radii of the Jacobi matrices of the inviscid fluxes **F**, **G**, **H**, that are:

$$\rho_A \leq |u| + \sqrt{u^2 + \tilde{\beta}^2} \tag{4.76}$$

$$\rho_B \leq |v| + \sqrt{v^2 + \tilde{\beta}^2} \tag{4.77}$$

$$\rho_C \leq |w| + \sqrt{w^2 + \tilde{\beta}^2} \tag{4.78}$$

Reader can find more information and the derivation of this stability condition in [7].

4.8 Computational domain

4.8.1 Cosine shaped hill

Symmetrical cosine shaped hill has been used for 2D and 3D simulations of atmospheric boundary layer flows. The hill has been defined by a following function (in 3D):

$$z_0(x,y) = \begin{cases} \frac{h}{2}\left(\cos r + 1\right) & \text{if} \quad r \leq \pi \\ 0 & \text{if} \quad r > \pi \end{cases} \text{, where } r = 2\pi\sqrt{x^2 + y^2} \tag{4.79}$$

in 2D there has been taken just a middle part of the 3D domain running through the center of the hill in XZ plane.
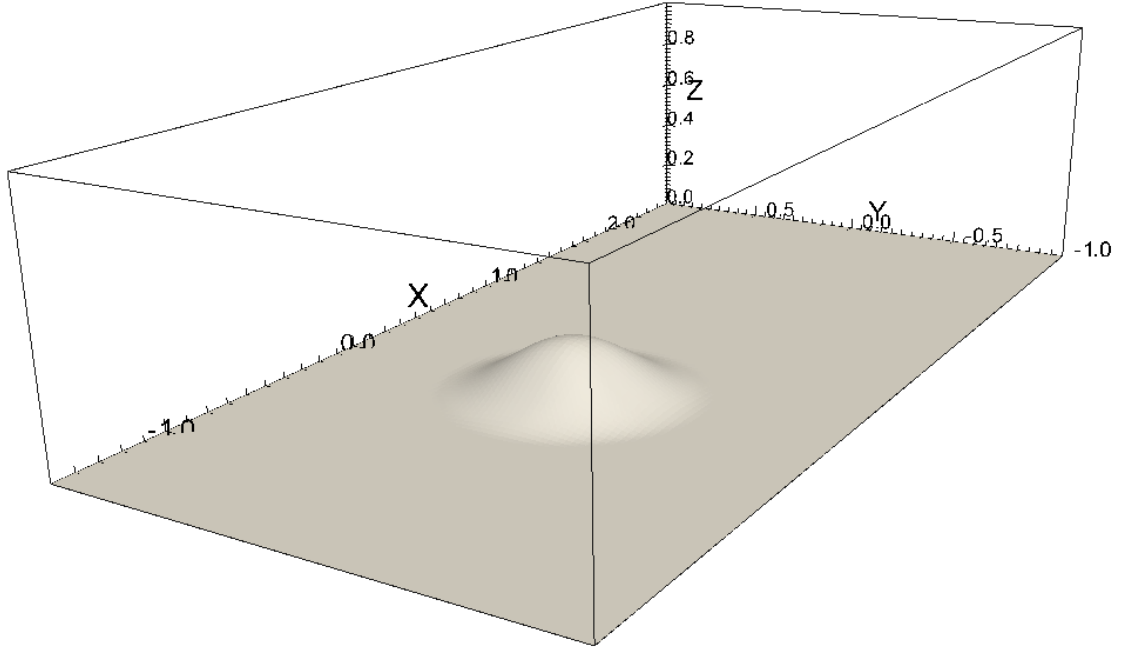
Figure 4.6: 3D Computational domain - one cosine shaped hill
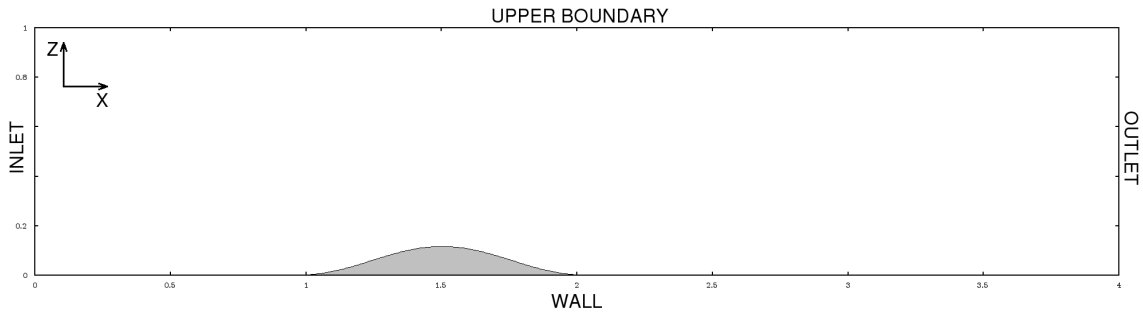
Figure 4.7: 2D/3D Computational domain - one cosine shaped hill
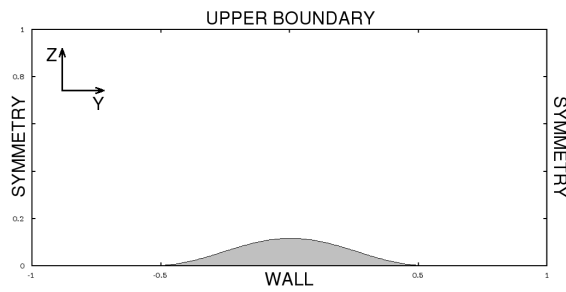
Figure 4.8: 3D Computational domain - one cosine shaped hill - YZ slice
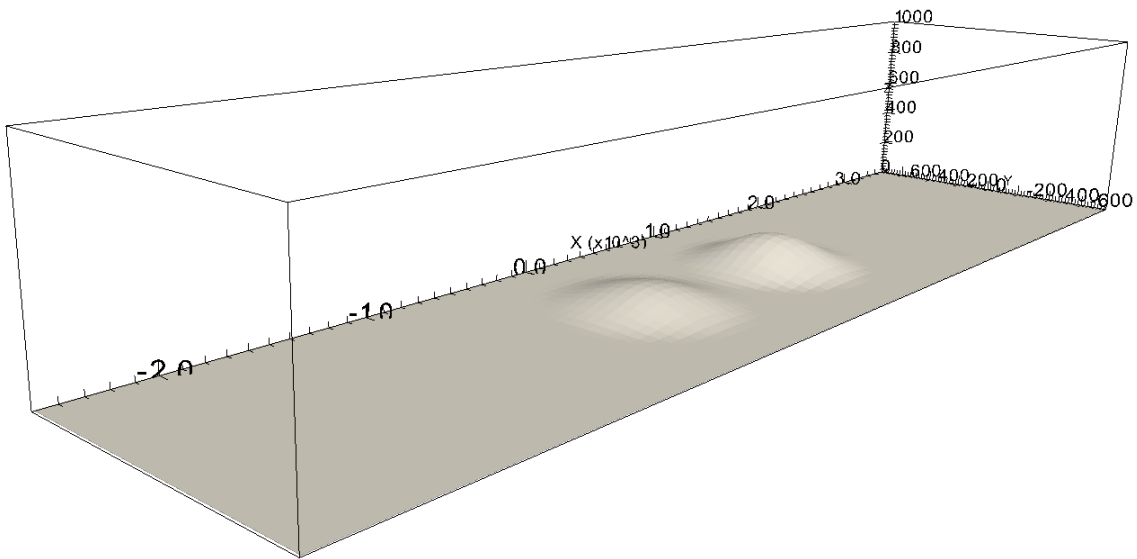
Figure 4.9: 3D Computational domain - two cosine shaped hills case 1
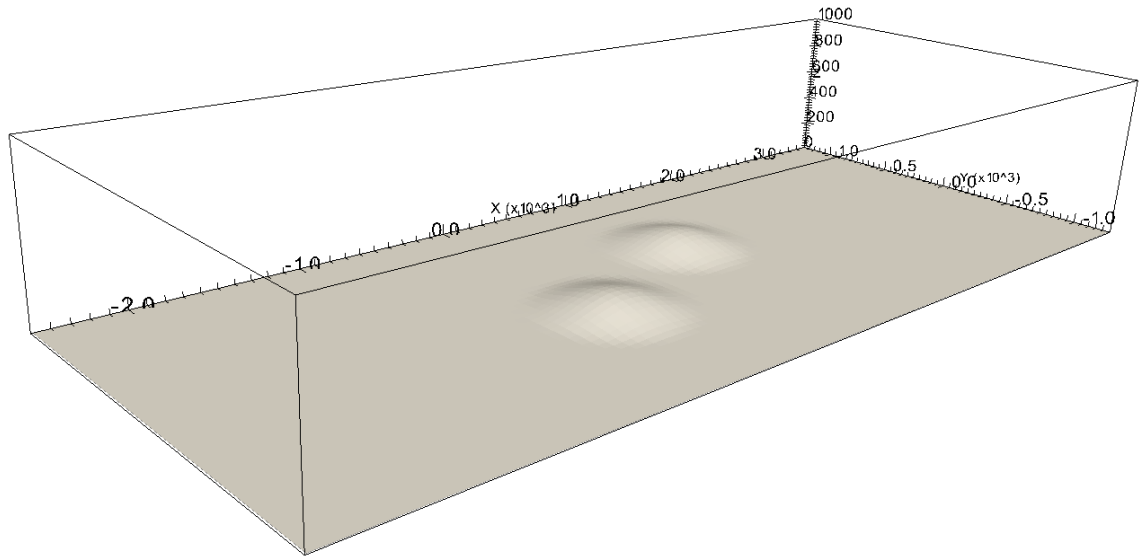
Figure 4.10: 3D Computational domain - two cosine shaped hills case 2

4.8.2 Witch of Agnesi hill

So called Witch of Agnesi hill has been used for 2D computations. The geometry is given by a following equation:

$$z_0(x) = \frac{8\left(\frac{h}{2}\right)^3}{x^2 + \left(\frac{h}{2}\right)^2}, \tag{4.80}$$

where h is the height of the hill. The only geometry with $h = 1000\,[m]$ has been taken into account.
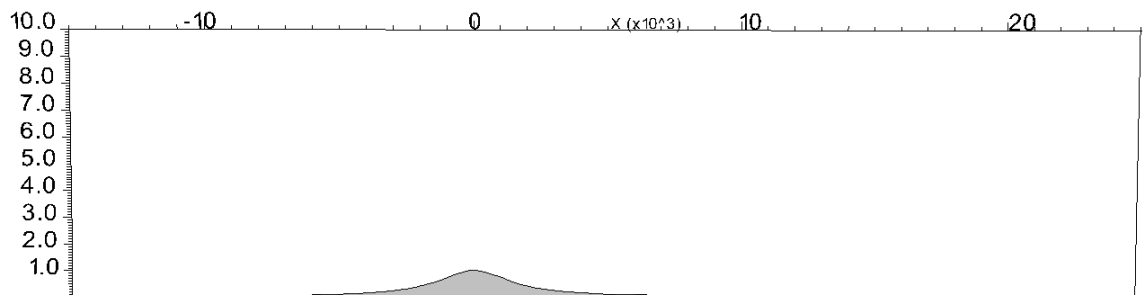
Figure 4.11: Witch of Agnesi - Computational domain

4.9 Boundary Conditions

4.9.1 Inlet

There have been used the Dirichlet boundary conditions for all the quantities u, v, w, ρ, k, ε except pressure p or the pressure perturbations p'' at the inlet of the domain. The density ρ has been set as linear decreasing function with the increasing height, going from ρ_{0_w}

(density on the ground where $z = 0$) to ρ_H (density in the upper boundary where $z = H$):

$$\rho(z) = \frac{\rho_H - \rho_{0_w}}{H} z + \rho_{0_w},\qquad(4.81)$$

where H is the height of the domain. Pressure (or pressure perturbations) has been extrapolated at the inlet.

4.9.2 Outlet

At the outlet the pressure p or the pressure perturbations have been set by Dirichlet boundary condition. $p = p'' = 0$. All the other quantities have been extrapolated at the outlet.

4.9.3 Wall

On the wall the no-slip boundary condition for velocity vector $\mathbf{U} = 0$ has been applied. The pressure p or the pressure perturbations p'' have been extrapolated on the wall. There was tested a couple of boundary conditions for density ρ_w. The first one has been the Dirichlet boundary condition i.e. $\rho_w = \rho_w(x, y)$ on the ground wall by a following relation:

$$\rho_w(x, y) = \frac{\rho_H - \rho_{0_w}}{H} z_0(x, y) + \rho_{0_w},\qquad(4.82)$$

where H is the height of the domain, $z_0(x, y)$ is the absolute z coordinate of the ground (let's say altitude) and ρ_{0_w} is the density in $z = 0$. And the second choice was the extrapolation of density from the inner flow field to the wall.

4.9.4 Upper Boundary

The free stream flow has to be simulated. There have been set the Dirichlet boundary condition for the x velocity component $u = const.$. And for the other velocity components have been the homogeneous Neumann boundary condition i.e.:

$$\frac{\partial v}{\partial \mathbf{n}} = 0 \qquad(4.83)$$

$$\frac{\partial w}{\partial \mathbf{n}} = 0 \qquad(4.84)$$

4.9.5 Lateral sides of the Domain

The lateral sides of the domain play a role just in 3D case. The symmetry boundary conditions have been applied to the lateral sides of the domain in all computed cases. But, there is also a possibility to use a periodic boundary conditions on lateral sides of the domain.

4.10   Computational grid
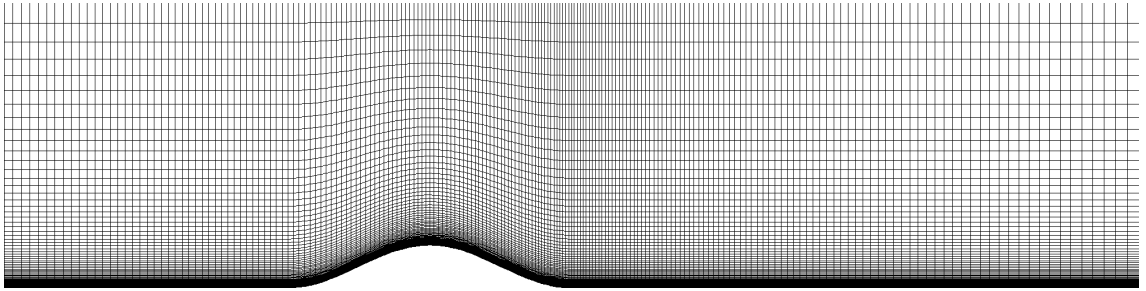
Figure 4.12: Computational grid (cosine hill)

The structured quadrilateral computation grid has been used in 2D computations and the structured hexahedral grid has been used in 3D simulations.

The grid pattern is presented in the figure (4.12). The grid has been refined near and around the obctacle (cosine hill, Witch of Agnesi hill) and also refined near the ground wall up to the $\Delta z_{min} < 1/\sqrt{Re}$.

Part III

Numerical Results

Chapter 5

Numerical Results 2D

Contents

All the presented results have been computed using a finite volume solver written in C++ programming language by the author of this thesis. The computational grids have been prepared in author's own grid generator. All the grids are structured quadrilateral grids refined in x,y direction around the hill and refined in z direction near the ground.

Convergence of all the computations has been monitored on the course of the residuals. The residuals have been computed by a following formula:

$$\mathbf{RES}(\mathbf{W}) = \log_{10}\left(\frac{1}{N}\sqrt{\sum_{j=1}^{N}(\tilde{\mathbf{L}}\mathbf{W}_j)^2} \right), \tag{5.1}$$

where N is the count of all the cells in the computational grid.

5.1 Standard k-ε and Realizable k-ε turbulence models validation

The flat plate test case has been chosen for validation of the implementation of the standard and Realizable k-ε turbulence models.
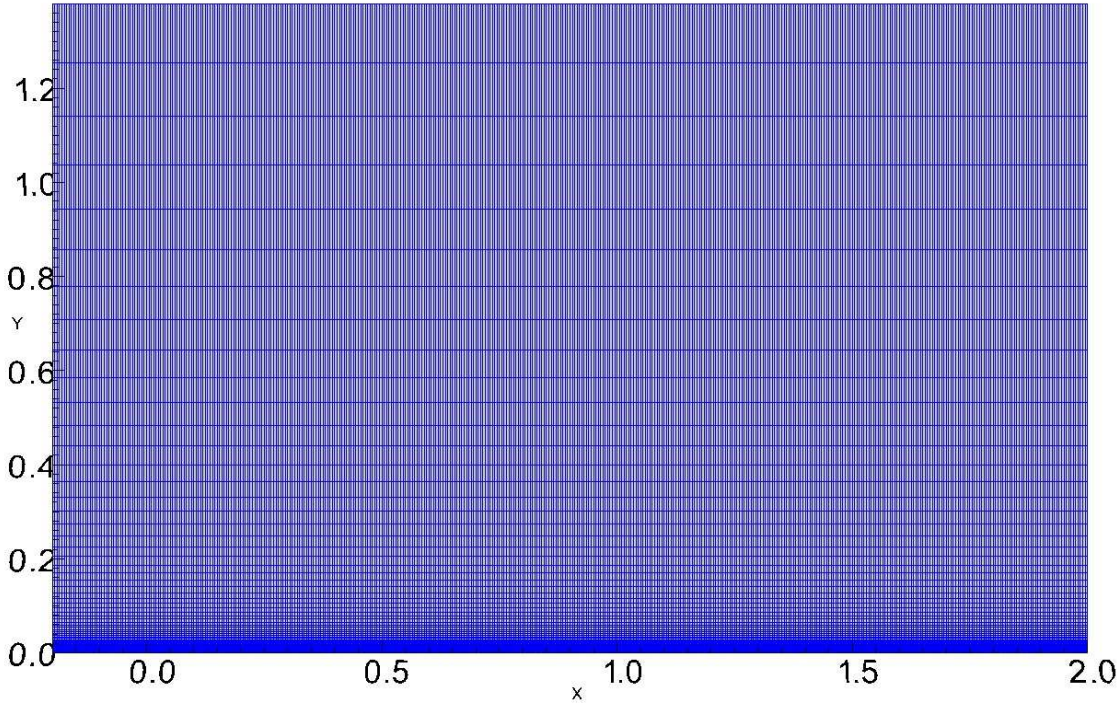
Figure 5.1: Flat Plate - Computational domain geometry and computational grid

Validation has been done on a rectangular domain 2.2 x 1.4 m. The lower boundary has been divided into two parts. The symmetry boundary condition for all variables has been used on a first part [-0.2; 0.0] m of the lower boundary and no-slip boundary condition for velocity, $k = 0$ and $\varepsilon = 2\nu\frac{k}{y^2}$ have been used on the rest of the lower boundary (the flat plate). The upper boundary has been modeled with the symmetry boundary conditions for all variables. The inlet part boundary conditions have been set as follows:

$$U_\infty = 5.4\frac{m}{s}, \ k_\infty = \frac{3}{2}(UI)^2, \ \varepsilon_\infty = C_\mu^{\frac{3}{4}}\frac{k^{\frac{3}{2}}}{l}, \tag{5.2}$$

where $I = 3\%$ is the turbulence intensity and $l = 0.07d_h$ is the turbulence length-scale and $d_h = \frac{inlet\ area}{inlet\ circumference}$ is the hydraulic diameter. The hydraulic diameter has been computed as follows:

$$d_h = 2 \lim_{a \to \infty} \frac{1.4\,a}{2.8 + 2a} = 1.4\,m \tag{5.3}$$

Constant atmospheric pressure has been prescribed on outlet.

Values of the inlet boundary conditions have been chosen as in the experiment which is available. And the comparison of the skin friction coefficient on the flat plate with the experimental data and the Blasius and White solution has been done for both presented models. Both models show the good match with the theory and experiment, as one can se in the figure (5.3), which shows the development of the skin friction coefficient depending on Reynolds number in the x direction of the flat plate. As one can see the standard $k - \varepsilon$ model predicts the turbulent flow earlier and the realizable $k - \varepsilon$ predicts the turbulent flow later than the experiment.
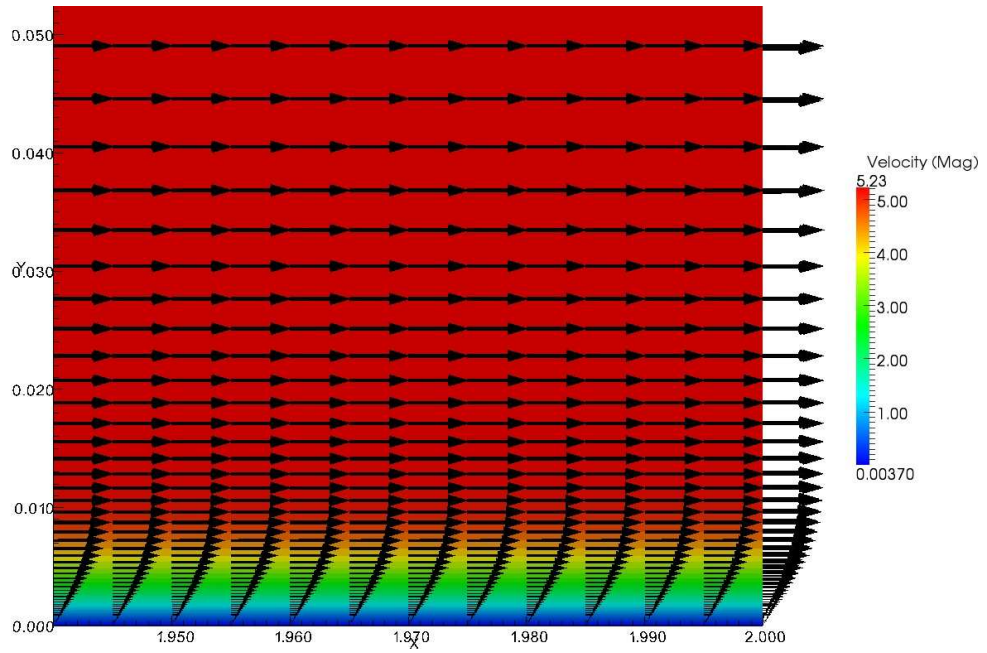
Figure 5.2: Flat Plate - Realizable k-ε turbulence model - Velocity vectors at the outlet $[m \cdot s^{-1}]$
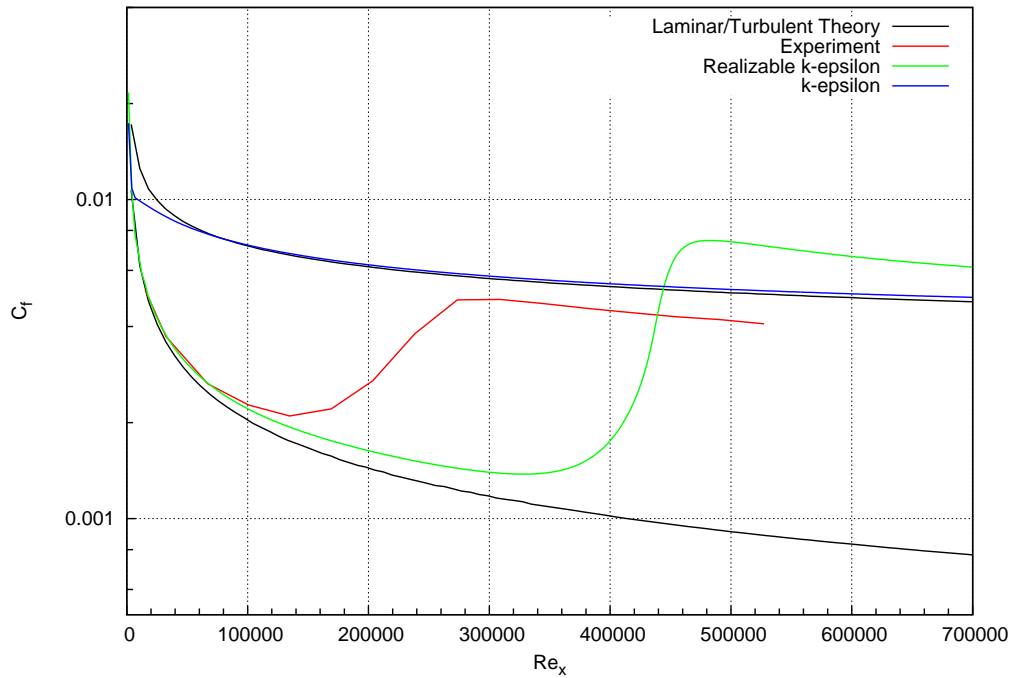
Figure 5.3: Flat Plate - Comparison of k-ε and Realizable k-ε turbulence models - Skin friction coefficient (C_f)

5.2 Witch of Agnesi hill computation and comparison

Two 2D cases with the Witch of Agnesi hill geometry (see figure (4.11)) have been performed and compared with the results of Ivo Sládek [34] and Eidsvik and Utnes [26].

The first case was the computation of the neutrally stratified incompressible turbulent flow over the hill using the Cebecci-Smith algebraic turbulence model. The second case was the computation of the neutrally stratified incompressible turbulent flow using the standard $k - \varepsilon$ turbulence model. The second case has been set up very similar to the computation of Ivo Sládek to compare the same cases. Both cases have been computed using Lax-Wendroff (MacCormack) scheme.

Grid parameters have been set similarly as in the computation performed by Sládek. The computational grid size has been set to 100x40 cells and the smallest cell dimension in the z axis direction has been set as $\Delta z_{min} = 20 \, [m]$. Assuming that the height of the domain is $H = 10\,000 \, [m]$, the main stream inlet velocity is $u_\infty = 10.05 \, [m \cdot s^{-1}]$, and the kinematic viscosity of the air is approximately $\nu = 1.5 \cdot 10^{-5}$ then the resulting Reynolds number is $Re = 6.7 \cdot 10^9$. The coarse grid resolution allows to use the $k - \varepsilon$ model, that is designed for corse grid resolution near the walls, but the usage of the Cebecci-Smith model on such a coarse grid could not give the good results. This model needs the near wall grid resolution $\Delta z \approx 1/\sqrt{Re}$, which is not satisfied in this case.

Boundary conditions for both cases have been set as follows:

- Inlet:

$$
\begin{aligned}
u_\infty &= \begin{cases} \frac{u^*}{\kappa} \ln\left(\frac{z}{z_0}\right) & \text{if} \quad z < 100 \, [m] \\ 10.05 & \text{if} \quad z \geq 100 \, [m] \end{cases}, \\
w_\infty &= 0, \\
k_\infty &= \frac{(u^*)^2}{\sqrt{C_\mu}} \left(1 - \frac{z}{H}\right), \\
\varepsilon_\infty &= \frac{C_\mu^{3/4} \cdot k_\infty(z)^{3/2}}{\kappa \cdot z},
\end{aligned}
$$

where $u^* = 0.4059 \, [m \cdot s^{-1}]$, $\kappa = 0.41$ is the von Karman's constant, $C_\mu = 0.09$ is the constant of the $k - \varepsilon$ turbulence model and $H = 10\,000 \, [m]$ is the height of the domain.

- Upper boundary:

$$
\begin{aligned}
u &= u(H), \\
\frac{\partial w}{\partial z} &= 0, \\
k &= k_\infty(H), \\
\varepsilon &= \varepsilon_\infty(H).
\end{aligned}
$$

- Ground wall:

$$
\begin{aligned}
u_w = w_w &= 0 \\
k_w &= 0 \\
\varepsilon_w &= 2\nu \frac{k}{d_w^2}
\end{aligned}
$$

where d_w is the distance of the first wall neighboring cell center from the wall.

- Outlet:

$$
p_\infty = 0
$$
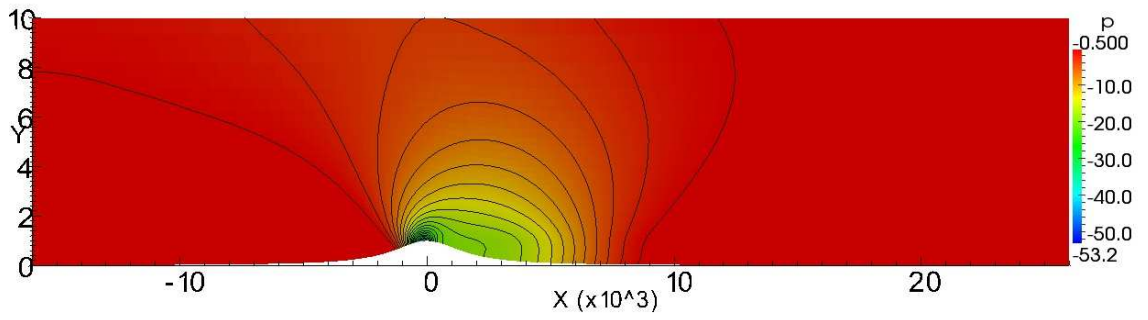
Figure 5.4: Witch of Agnesi Hill - algebraic - Contours of pressure $[Pa]$
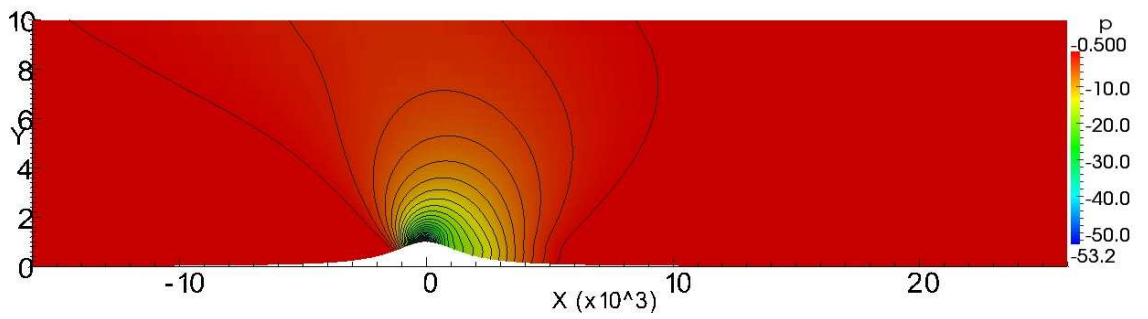
Figure 5.5: Witch of Agnesi Hill $k - \varepsilon$ - Contours of pressure $[Pa]$
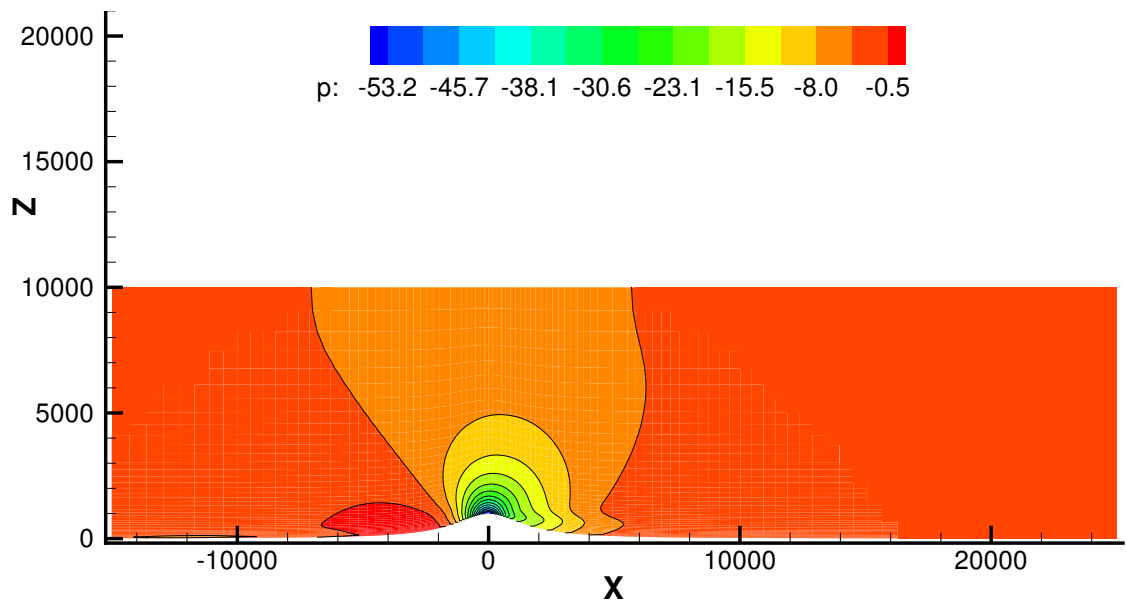
Figure 5.6: Witch of Agnesi Hill - Ivo Sládek's results - Contours of pressure $[Pa]$
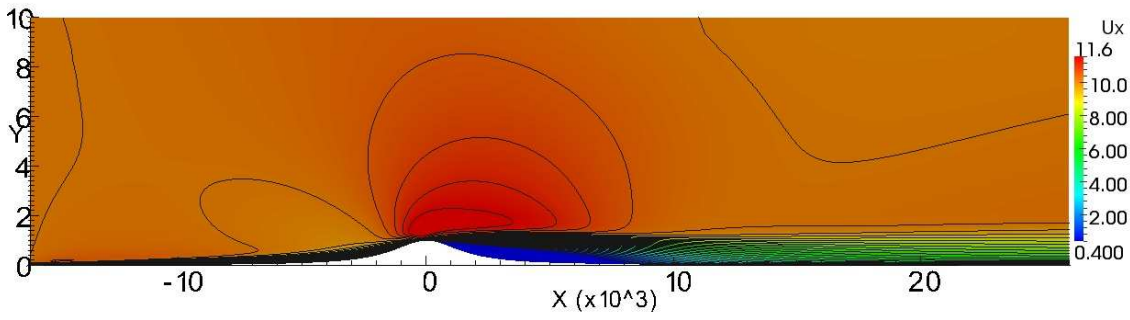
Figure 5.7: Witch of Agnesi Hill - algebraic - Contours of x velocity component $[m \cdot s^{-1}]$
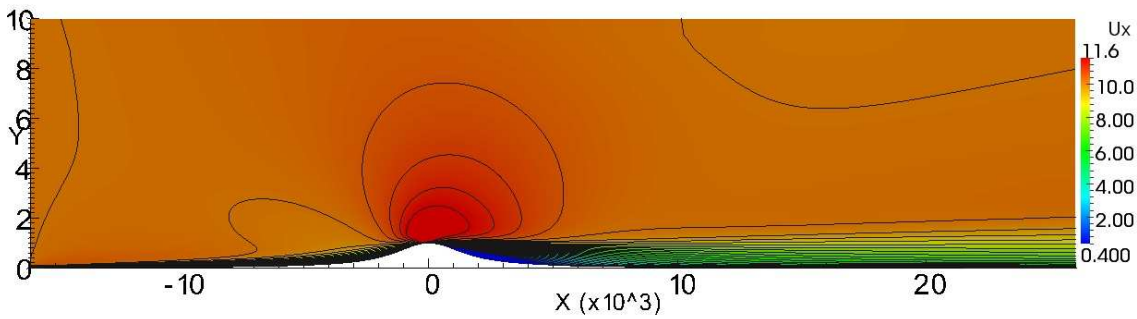
Figure 5.8: Witch of Agnesi Hill $k - \varepsilon$ - Contours of x velocity component $[m \cdot s^{-1}]$
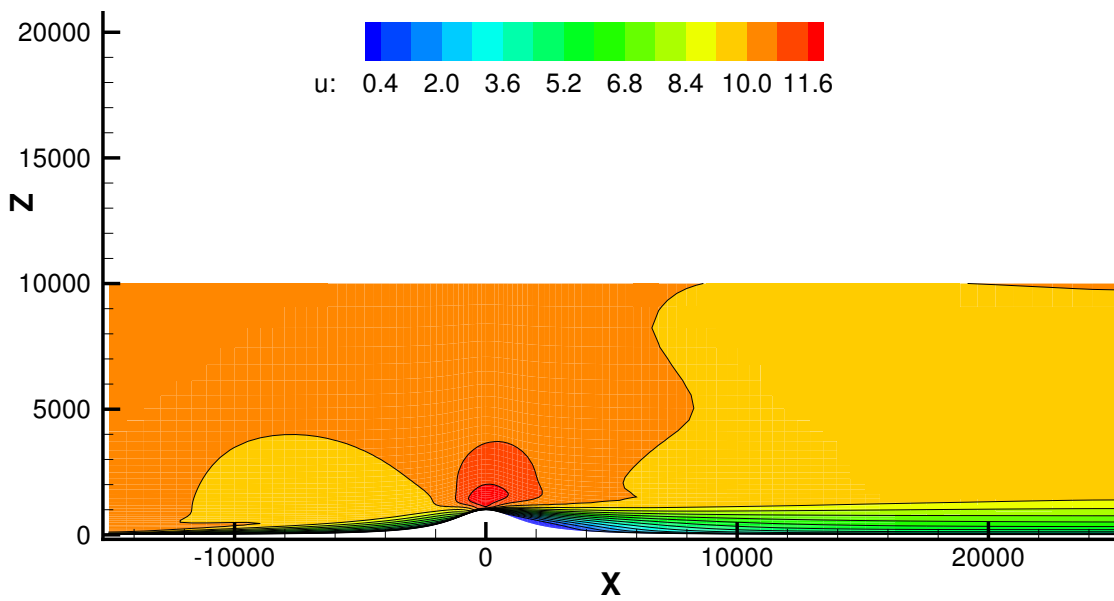
Figure 5.9: Witch of Agnesi Hill - Ivo Sládek's results - Contours of x velocity component $[m \cdot s^{-1}]$
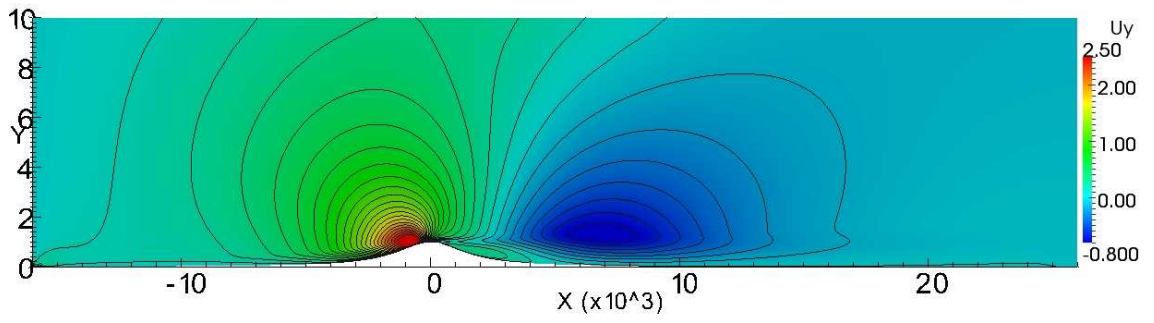
Figure 5.10: Witch of Agnesi Hill - algebraic - Contours of z velocity component $[m \cdot s^{-1}]$
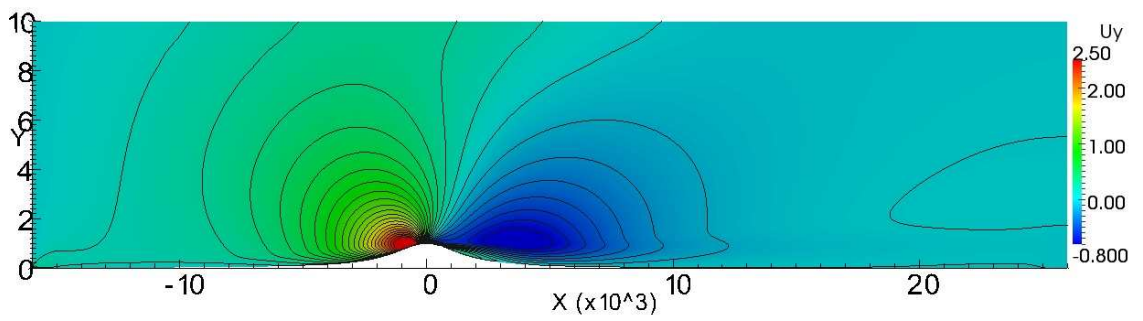
Figure 5.11: Witch of Agnesi Hill $k - \varepsilon$ - Contours of z velocity component $[m \cdot s^{-1}]$
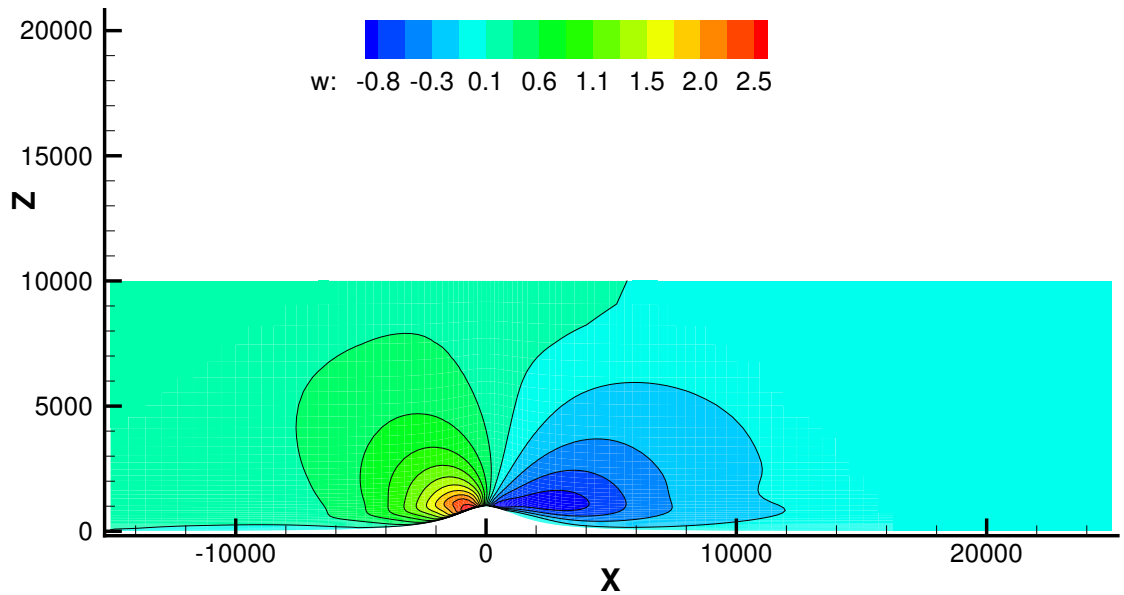
Figure 5.12: Witch of Agnesi Hill - Ivo Sládek's results - Contours of z velocity component $[m \cdot s^{-1}]$
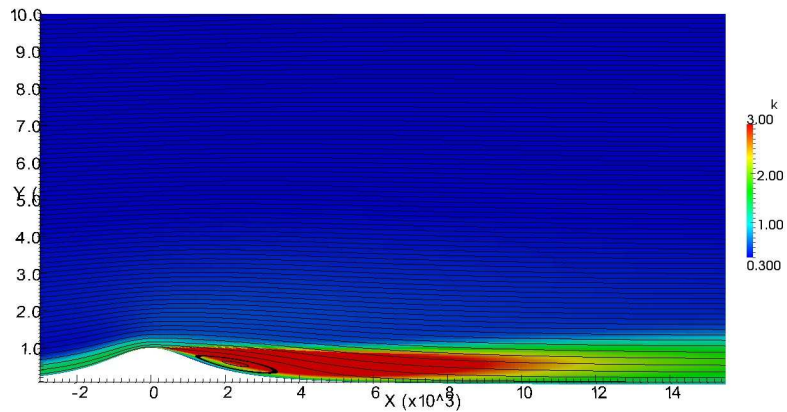
Figure 5.13: Witch of Agnesi Hill $k - \varepsilon$ - Contours of turbulent kinetic energy $[m^2 \cdot s^{-2}]$
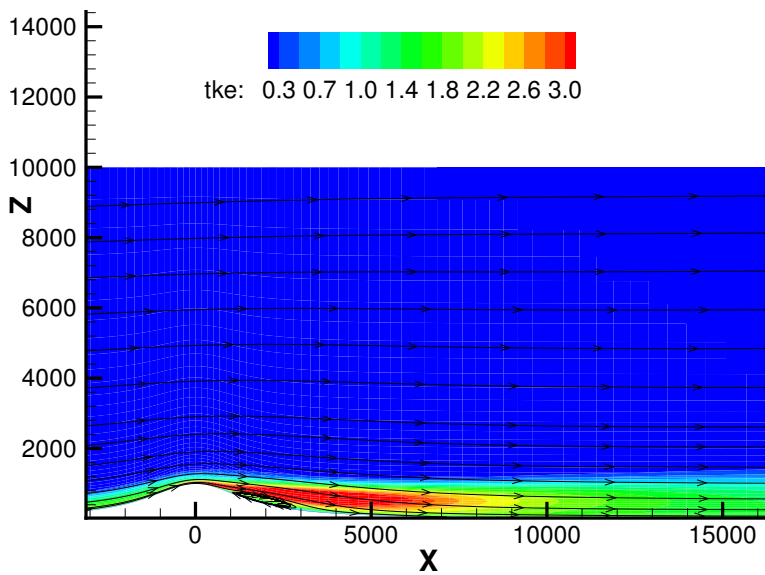
Figure 5.14: Witch of Agnesi Hill - Ivo Sládek's results - Contours of turbulent kinetic energy $[m^2 \cdot s^{-2}]$
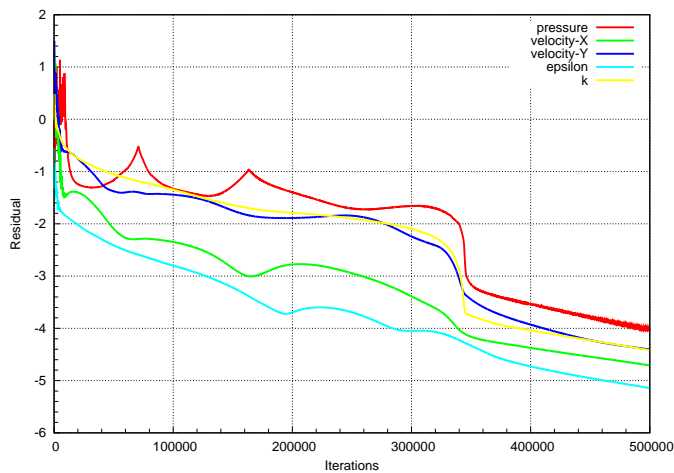
Figure 5.15: Witch of Agnesi Hill $k - \varepsilon$ - Convergence of the computation

Presented results of the computation with the standard $k - \varepsilon$ turbulence model correspond each other very well with the results obtained by Ivo Sládek et al. [34], as one can see in the presented figures. The computation performed with the Cebecci-Smith algebraic turbulence model does not correspond each other so well. On the one hand algebraic turbulence models in general are not suitable to the cases where occures the separation of the flow. They usually over predict the size of separation zone behind the obstacle. Exactly the same situation came in our case. As one can see in the presented figures, the separation zone behind the hill is much larger in case with Cebecci-Smith algebraic turbulence model than in the case with the standard $k - \varepsilon$ turbulence model, which was expected. On the other hand, the solution obtained using the algebraic turbulence model could be influenced by the usage of the computational grid that is coarse in the near wall regions and does not satisfy the recommended near wall resolution.

5.3 Stratified incompressible turbulent results of the flow over 2D cosine shaped hill

The 2D flow past one cosine shaped hill is considered in this case. The height of the hill is 10% of its basis length. The basis length of the hill is $1000\,[m]$ so the height h of the hill is $h = 100\,[m]$.

Lax-Wendroff (MacCormack) scheme have been used to compute following results. The Boussinesq density based model together with the Cebecci-Smith algebraic turbulence model has been used in all three following cases. The gravitational acceleration vector has been set to $\mathbf{g} = (0,\,0,\,-10)$ approximately as the gravitational acceleration of the Earth for all cases.

All the following computations have been performed using the same computational domain (see figure (4.7)). The cases differ in the computational grid parameters, the inlet boundary condition for the density and the values of inlet velocity (or one can say in the values of Reynolds number). The stable stratification condition has been set in all simulations but with different density ranges (different values of ρ_H and ρ_{0_w}). The inlet boundary condition has been set according to (4.81), where the height of the domain has been $H = 1000\,[m]$ in all following cases.

5.3.1 Case 1

The fine computational mesh (300 cells in x direction, 100 cells in z direction), with the near wall resolution $\Delta z_{min} < 1/\sqrt{Re}$, has been considered in the first case.
The inlet boundary condition for density has been set according to the equation (4.81) and its range has been chosen as follows:

  - density near the ground $\rho_{0_w} = 1.2 \left[\frac{kg}{m^3} \right]$

  - density at the top of the domain $\rho_H = 1.1 \left[\frac{kg}{m^3} \right]$.
No boundary condition for density ρ_w on the ground has been set and the density has been extrapolated on the ground wall.

The Reynolds number has been set to $Re = 10^8$ which corresponds approximately to the inlet velocity $u_\infty = 1.5\,[m \cdot s^{-1}]$, if one considers that the kinematic viscosity of the air is about $\nu = 1.5 \cdot 10^{-5}\,[m^2 \cdot s^{-1}]$. The uniform velocity distribution in the inlet has been considered there.

The figure (5.16) shows results of the first case the distribution of the velocity magnitude.
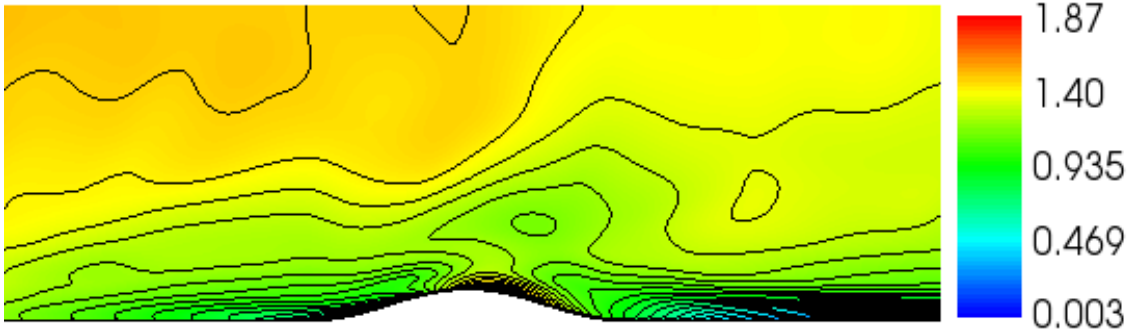
Figure 5.16: 2D cosine 10% - Velocity magnitude $[m \cdot s^{-1}]$
($\rho \in [1.1; 1.2]$, $Re = 10^8 \approx U_\infty = 1.5~m \cdot s^{-1}$)

5.3.2 Case 2

The same fine computational mesh as in the Case 1 (300 cells in x direction, 100 cells in z direction), with the near wall resolution $\Delta z_{min} < 1/\sqrt{Re}$, has been considered also in the second case.

The inlet boundary condition for the density has been set according to the equation (4.81) and the same range as in the first case has been chosen:

- density near the ground $\rho_{0_w} = 1.2 \left[\frac{kg}{m^3}\right]$

- density at the top of the domain $\rho_H = 1.1 \left[\frac{kg}{m^3}\right]$.

No boundary condition for density ρ_w on the ground has been set and the density has been extrapolated on the ground wall.

The Reynolds number has been set to $Re = 5 \cdot 10^8$ which corresponds approximately to the inlet velocity $u_\infty = 7.5~[m \cdot s^{-1}]$, if one considers that the kinematic viscosity of the air is about $\nu = 1.5 \cdot 10^{-5}~[m^2 \cdot s^{-1}]$. The uniform velocity distribution in the inlet has been considered there.

The figure (5.17) shows results of the first case the distribution of the velocity magnitude.
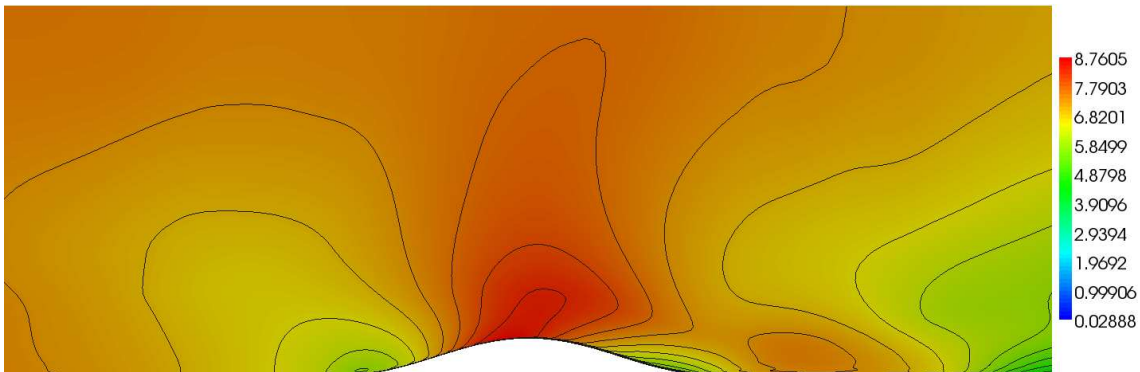
Figure 5.17: 2D cosine 10% - Velocity magnitude $[m \cdot s^{-1}]$
($\rho \in [1.1; 1.2]$, $Re = 5 \cdot 10^8 \approx U_\infty = 7.5~m \cdot s^{-1}$)

5.3.3 Case 3

The much coarser computational mesh as in the Case 1 and 2 (100 cells in x direction, 40 cells in z direction), with the near wall resolution $\Delta z_{min} \approx 10/\sqrt{Re}$, has been considered in this last case.

The inlet boundary condition for density has been set according to the equation (4.81) but the much larger range than in the first and second case has been chosen:

- density near the ground $\rho_{0_w} = 1.2 \left[\frac{kg}{m^3} \right]$

- density at the top of the domain $\rho_H = 0.6 \left[\frac{kg}{m^3} \right]$.

No boundary condition for density ρ_w on the ground has been set and the density has been extrapolated on the ground wall.

The Reynolds number has been set to lower value $Re = 6.67 \cdot 10^7$ which corresponds approximately to the inlet velocity $u_\infty = 1.0 \ [m \cdot s^{-1}]$, if one considers that the kinematic viscosity of the air is about $\nu = 1.5 \cdot 10^{-5} \ [m^2 \cdot s^{-1}]$. The uniform velocity distribution in the inlet has been considered there same as in previous two cases.

Figures (5.18), (5.20) show results of the third case the distribution of the velocity magnitude without and with stream lines and the figure (5.19) shows the the z velocity component distribution in the computational domain.
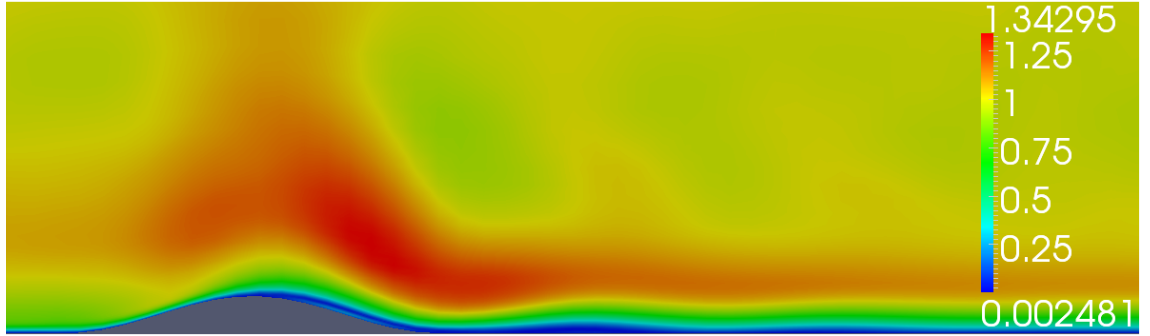
Figure 5.18: 2D cosine 10% - Velocity magnitude $[m \cdot s^{-1}]$
($\rho \in [0.6; 1.2]$, $Re = 6.67 \cdot 10^7 \approx U_\infty = 1.0 \ m \cdot s^{-1}$)
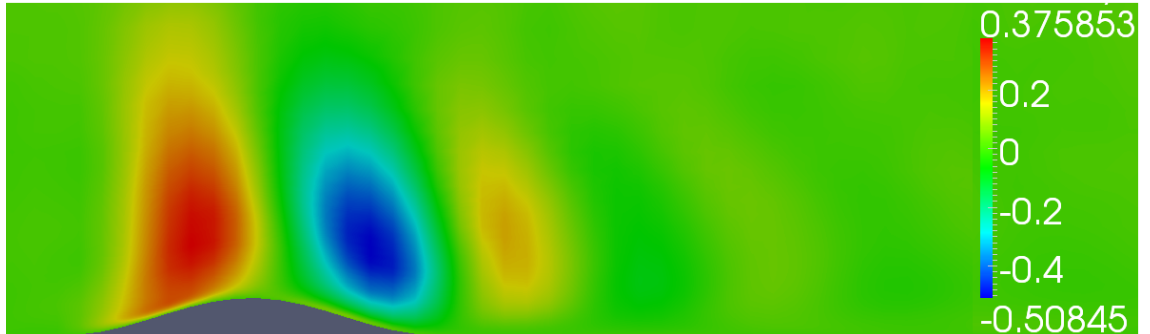
Figure 5.19: 2D cosine 10% - Velocity Z $[m \cdot s^{-1}]$
($\rho \in [0.6; 1.2]$, $Re = 6.67 \cdot 10^7 \approx U_\infty = 1.0 \ m \cdot s^{-1}$)
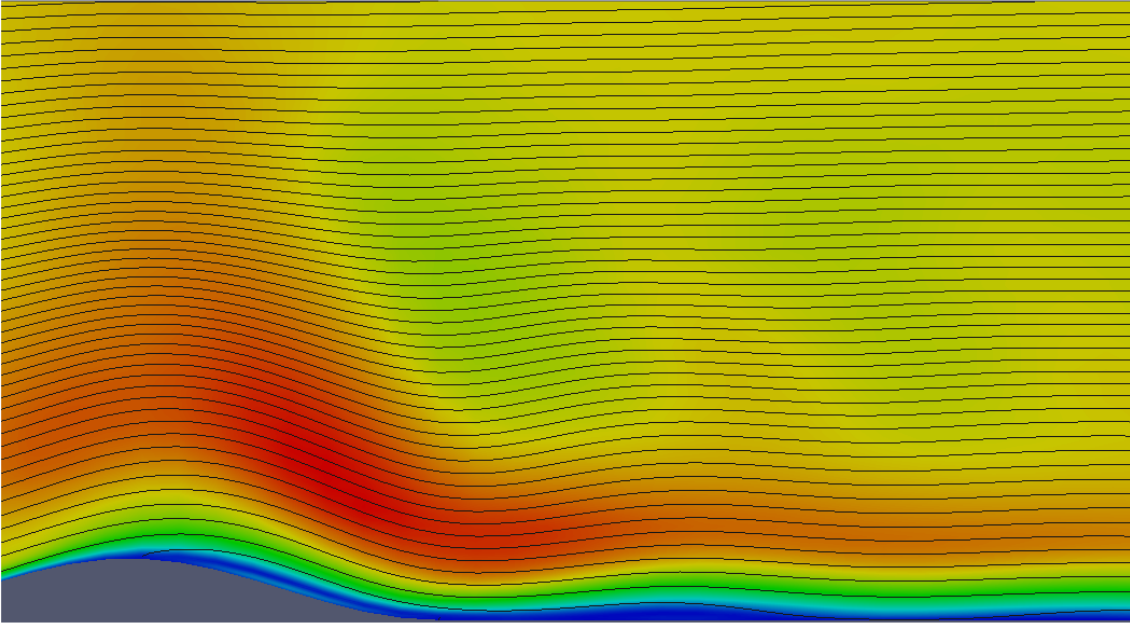
Figure 5.20: 2D cosin 10% - Stream lines
($\rho \in [0.6; 1.2]$, $Re = 6.67 \cdot 10^7 \approx U_\infty = 1.0 \ m \cdot s^{-1}$)

5.3.4 Concluding remarks

The so called "lee waves" should appear in stratified flows. Lee waves are atmospheric standing waves, that are created behind the obstacles (on the lee sides of hills, mountains), that stays on the ground, due to the non constant density (stratification of the fluid) in atmospheric boundary layer flows. They are periodic changes of atmospheric pressure, temperature (density). The more information about the creation of lee waves can be found in [52] and [55].

One can see the creation of lee waves just in the last case, especially in the figure with stream lines (5.20) and also in the figure (5.19), where the z velocity component is shown. One can see the periodic changes of the vertical direction of the flow, that are damped because of the presence of viscous forces in the fluid.

In the last case where the inlet velocity is the lowest from all three cases, the density range is the highest and the grid is much coarser. The high inlet velocity of the flow lowers the influence of the source term related to the gravity. The higher inlet velocity the lower gravity influence. The range of the density, i.e. the measure of stratification (the density gradient) influences the effect of the gravity source term. The lower density gradient (density gradient is negative in case of stable stratification) the greater effect of the gravity source term.

The influence of the inlet velocity and inlet density gradient could be expressed through the dimensionless numbers: Froude number Fr (the ratio of a body's inertia to gravitational force) or Richardson number Ri (the ratio of potential to kinetic energy), ($Fr = 1/\sqrt{Ri}$). Usually the reciprocal of the Froude number (square root of the Richardson number) K is used in literature [26], [50]:

$$K = \frac{1}{Fr} = \sqrt{Ri} = \frac{Nh}{u_\infty}, \qquad N = \sqrt{-\frac{g}{\rho_{0_w}}\frac{\partial \rho}{\partial z}}, \tag{5.4}$$

where h is the height of the hill, N is the so called Brunt-Väisälä frequency, u_∞ inlet velocity, ρ density, ρ_{0_w} reference density and g is the gravitational acceleration. K is zero for neutrally stratified flows.

If one computes K according to equation (5.4), one obtains $K = 1.92$ for the Case 1, $K = 0.38$ for the Case 2 and finally $K = 7.07$ for the Case 3. Presented results show the same phenomenon as it is published in all reference papers [26], [34] and [50]. Lee waves appear and its frequency increases with increasing dimensionless number K. Lee waves do not appear in Case 1 and in Case 2 even thought the dimensionless number K is greater than zero. They appear only in the Case 3, where K is much higher. The properties of the computational grid could play role in these cases. The coarser grid the less dissipative simulation, i.e. the artificial dissipation added to the solution by the grid is lower on the coarse mesh.

The combination of all these effects could be the cause of the fact that there were no lee waves present in the first and second case, because the high velocity, the high vertical gradient of the density (low dimensionless number K) and the fine mesh can smooth lee waves.

5.4 Stratified incompressible turbulent results of the flow over two 2D cosine shaped hills

The same mathematical model and fluid properties have been chosen as in the Case 3 in the previous section (see section 5.3 and 5.3.3). The the same grid resolution has been taken there $\Delta z_{min} \approx 10/\sqrt{Re}$. The difference is in the geometry configuration. The flow past two cosine shaped hills is considered in this case. The height of the first hill (meant in direction of the flow) is 10% of its basis length and the height of the second hill is 15% of its basis. The basis length of the both hills is $1000\,[m]$ and the height h of the first one is $h = 100\,[m]$ and the second one $h = 150\,[m]$.

Lax-Wendroff (MacCormack) scheme have been used to compute following results. The Boussinesq density based model together with the algebraic turbulence model Cebecci-Smith has been used in this case. The gravitational acceleration vector has been set to $\mathbf{g} = (0, 0, -10)$ approximately as the gravitational acceleration of the Earth for all following cases.

The inlet boundary condition has been set according to the equation (4.81) and its range has been chosen as follows:

- density near the ground $\rho_{0_w} = 1.2\,\left[\frac{kg}{m^3}\right]$

- density at the top of the domain $\rho_H = 0.6\,\left[\frac{kg}{m^3}\right]$.

The Reynolds number has been set to $Re = 6.67 \cdot 10^7$ which corresponds approximately to the inlet velocity $u_\infty = 1.0\,[m \cdot s^{-1}]$ if one considers that the kinematic viscosity of the air is about $\nu = 1.5 \cdot 10^{-5}\,[m^2 \cdot s^{-1}]$. The uniform velocity distribution in the inlet has been considered there.

Two cases of the 2D stratified turbulent flow over two cosine hills have been computed. There has been tested an influence of the boundary conditions for the density on the ground wall. Two different boundary conditions have been set. Both cases have been solved on the same geometry configuration with the same fluid properties and the same initial and boundary conditions for all other quantities. The exact settings of boundary conditions for density is described independently for each case in following sections.

5.4.1 Case 1

The inlet boundary condition for density has been set according to the equation (4.81).

The boundary condition for density ρ_w on the ground has been set as Dirichlet boundary condition (i.e. ρ_w is set to be constant value for each boundary face during the computation). The density values have been set using the relation (4.82).

One can see the resulting distribution of the density in the figure (5.21), pressure perturbation distribution in the figure (5.22), x and z velocity components in figures (5.23) and (5.24).
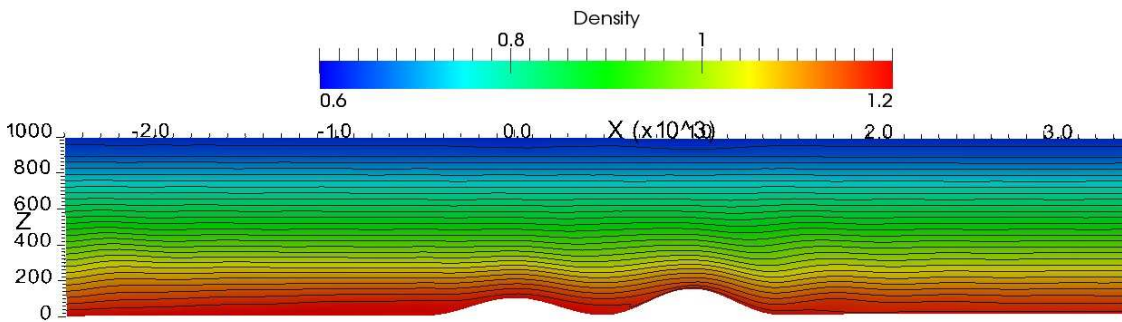
Figure 5.21: 2D cosine 10%, cosine 15% hills - Contours of density $[kg \cdot m^{-3}]$ ($\rho \in [0.6; 1.2]$, $Re = 6.67 \cdot 10^7 \approx U_\infty = 1.0 \ m \cdot s^{-1}$)
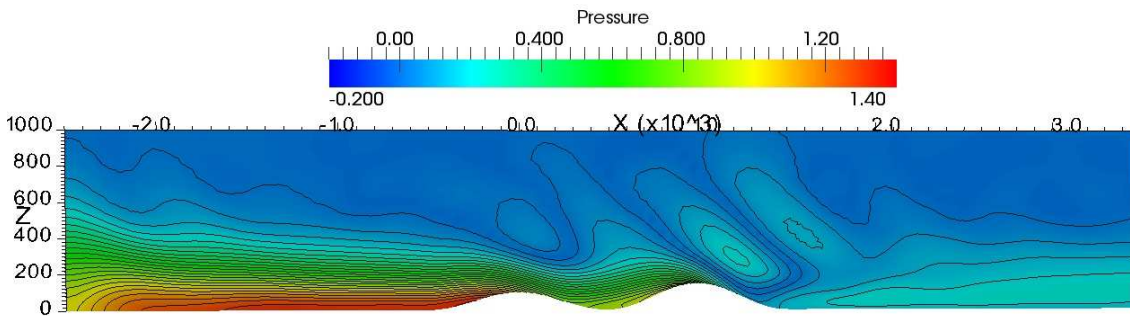
Figure 5.22: 2D cosine 10%, cosine 15% hills - Contours of Pressure Perturbations $[Pa]$ ($\rho \in [0.6; 1.2]$, $Re = 6.67 \cdot 10^7 \approx U_\infty = 1.0 \ m \cdot s^{-1}$)
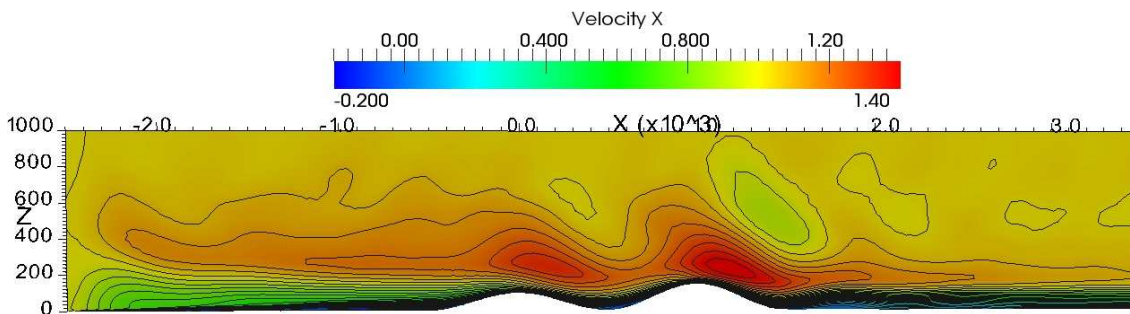
Figure 5.23: 2D cosine 10%, cosine 15% hills - Contours of velocity X ($\rho \in [0.6; 1.2]$, $Re = 6.67 \cdot 10^7 \approx U_\infty = 1.0 \ m \cdot s^{-1}$)
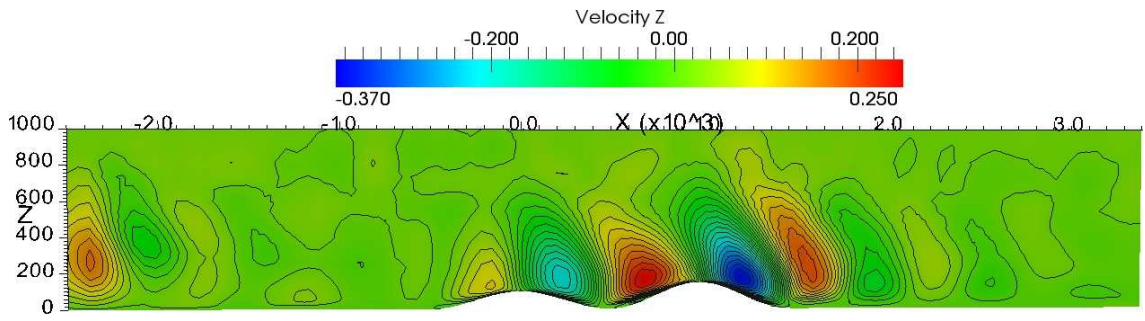
Figure 5.24: 2D cosine 10%, cosine 15% hills - Contours of velocity Z $[m \cdot s^{-1}]$
($\rho \in [0.6; 1.2]$, $Re = 6.67 \cdot 10^7 \approx U_\infty = 1.0 \ m \cdot s^{-1}$)

5.4.2 Case 2

The density linearly decreases with the increasing height according to the equation (4.81).

No boundary condition for density ρ_w on the ground has been set and the density has been extrapolated on the ground wall.

One can see the resulting distribution of the density in the figure (5.25), pressure perturbation distribution in the figure (5.26), x and z velocity components in figures (5.27) and (5.28).
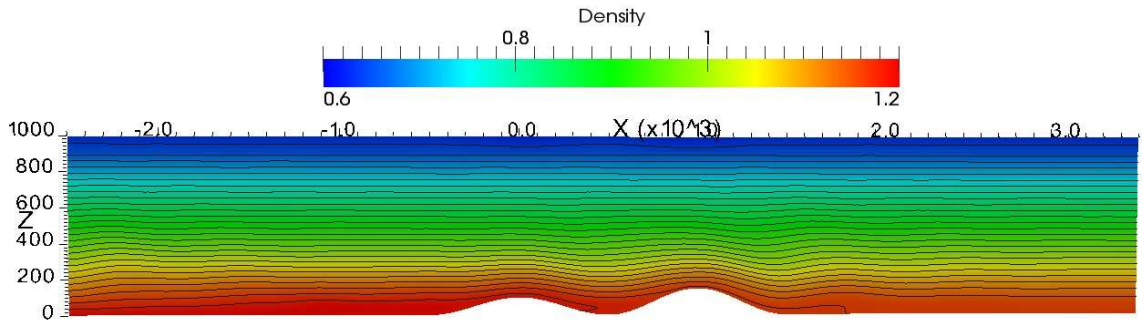
Figure 5.25: 2D cosine 10% cosine 15% - Contours of Density $[kg \cdot m^{-3}]$
($\rho \in [0.6; 1.2]$, $Re = 6.67 \cdot 10^7 \approx U_\infty = 1.0 \ m \cdot s^{-1}$)
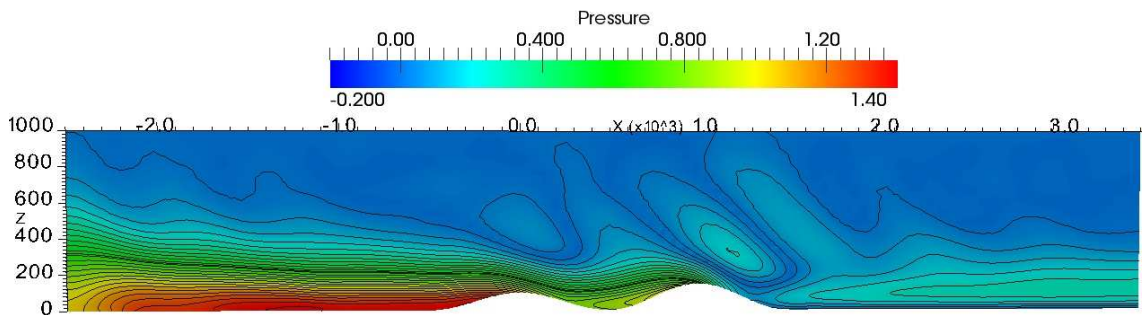
Figure 5.26: 2D cosine 10% cosine 15% - Contours of Pressure Perturbations $[Pa]$
($\rho \in [0.6; 1.2]$, $Re = 6.67 \cdot 10^7 \approx U_\infty = 1.0 \ m \cdot s^{-1}$)
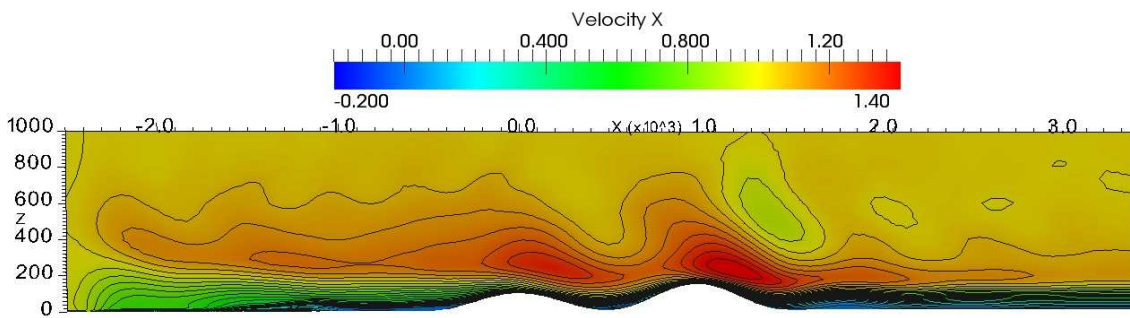
Figure 5.27: 2D cosine 10% cosine 15% - Contours of Velocity X
($\rho \in [0.6; 1.2]$, $Re = 6.67 \cdot 10^7 \approx U_\infty = 1.0 \ m \cdot s^{-1}$)
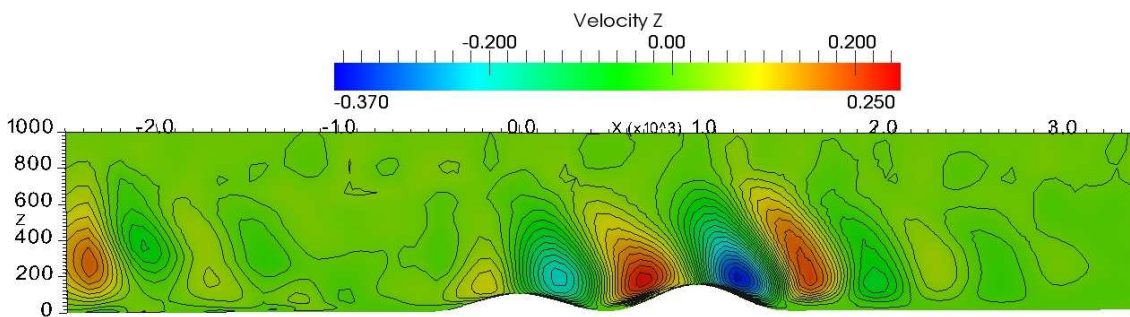
Figure 5.28: 2D cosine 10% cosine 15% - Contours of Velocity Z $[m \cdot s^{-1}]$
($\rho \in [0.6; 1.2]$, $Re = 6.67 \cdot 10^7 \approx U_\infty = 1.0 \ m \cdot s^{-1}$)
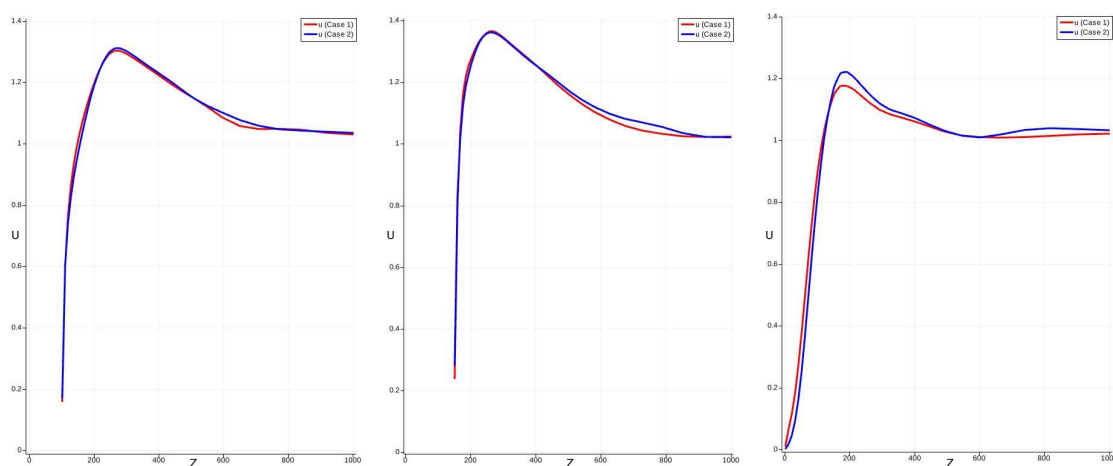
Figure 5.29: 2D cosine 10% cosine 15% - Velocity profile comparison - in $x = 0 \ [m]$ (top of the first hill), $x = 1000 \ [m]$ (top of the second hill), $x = 2000 \ [m]$ (behind the second hill)

5.4.3 Concluding remarks

Both solutions converge to the steady state, as one can see from the figures (5.30), (5.31). Lee waves are present in both cases, as one can see in presented figures. One can see the oscillating direction of the z velocity component in the figures (5.24), (5.28). The creation of lee waves is independent on the choice of boundary conditions for the density. And also the solution does not depend so much on the choice of the wall boundary condition for density, as one can see from presented results. Case 1 and Case 2 solutions are very similar each other, what is visible in the figure (5.29), where velocity profiles are compared in three different places in the computational domain.

The dimensionless number $K = 7.07$ computed using relation (5.4) and taking into account that h is the height of the first hill $h = 100\,[m]$ is the same for both cases.
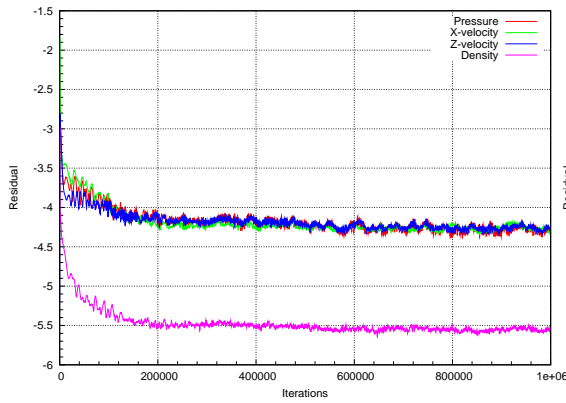
Figure 5.30: Case 1 - Residuals   **Figure 5.31:** Case 2 - Residuals
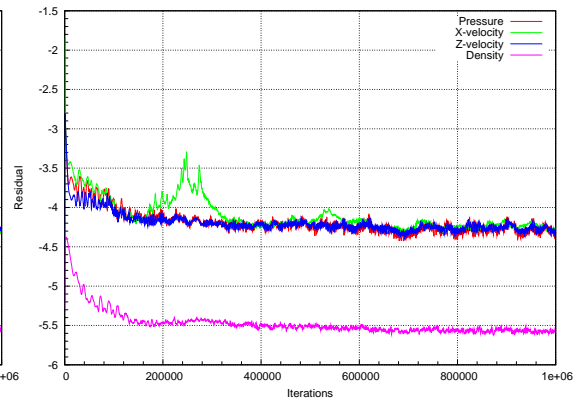
Chapter 6

Numerical Results 3D

Contents

6.1 Neutrally stratified incompressible turbulent results of the flow over one 3D cosine shaped hill

The 3D flow past one cosine shaped hill is considered in this case. The computational domain has been defined as the figures (4.6), (4.7), (4.8) show. The height of the hill is 10% of its basis length. The basis length of the hill is $1000\,[m]$ so the height h of the hill is $h = 100\,[m]$.

Lax-Wendroff (MacCormack) scheme have been used to compute following results. The incompressible Reynolds Averaged Navier-Stokes equations together with the Cebecci-Smith algebraic turbulence model has been used in this case, i.e. neutral stratification has been considered.

The Reynolds number has been set to $Re = 6.67 \cdot 10^7$ which corresponds approximately to the inlet velocity $u_\infty = 1.0\,[m \cdot s^{-1}]$ if one considers that the kinematic viscosity of the air is about $\nu = 1.5 \cdot 10^{-5}\,[m^2 \cdot s^{-1}]$. The uniform velocity distribution in the inlet has been considered there.

The fine computational mesh (200 cells in x direction, 100 cells in y direction, 80 cells in z direction), with the near wall resolution $\Delta z_{min} < 1/\sqrt{Re}$, has been considered in this case.

Reader can see the results of this simulation in figures (6.1) the x velocity distribution in XZ slice in the middle of the domain, (6.2) the z velocity distribution in XZ slice in the middle of the domain and (6.3) the x velocity distribution in XY slice in the middle of the hill height.
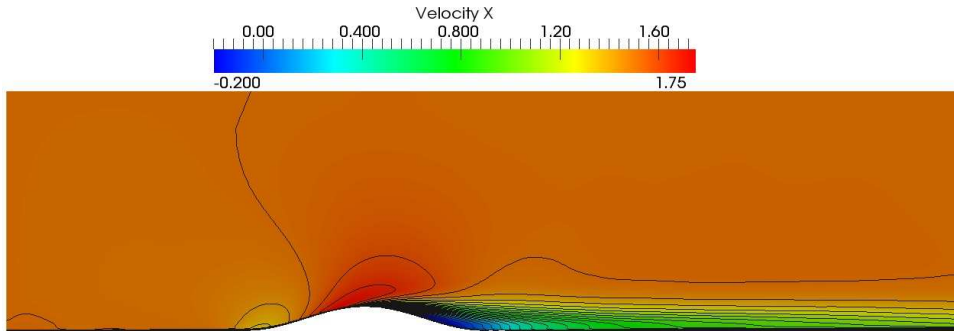
Figure 6.1: 3D cosine 10% hill - Contours of velocity X $[m \cdot s^{-1}]$ - XZ slice in the middle of the domain - $(Re = 6.67 \cdot 10^7 \approx U_\infty = 1.0 \ m \cdot s^{-1})$
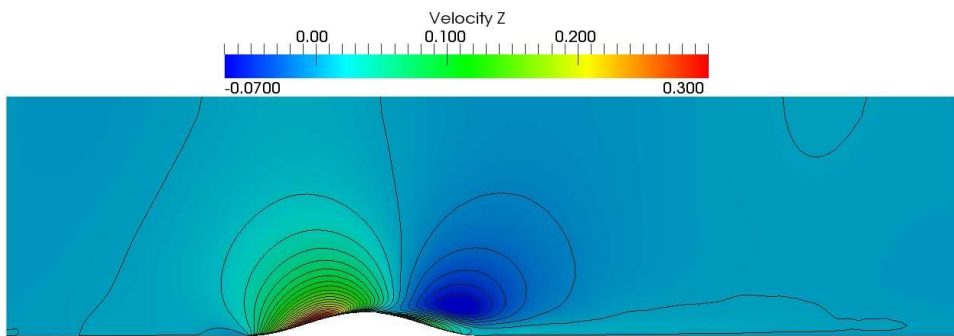
Figure 6.2: 3D cosine 10% hill - Contours of velocity Z $[m \cdot s^{-1}]$ - XZ slice in the middle of the domain - $(Re = 6.67 \cdot 10^7 \approx U_\infty = 1.0 \ m \cdot s^{-1})$
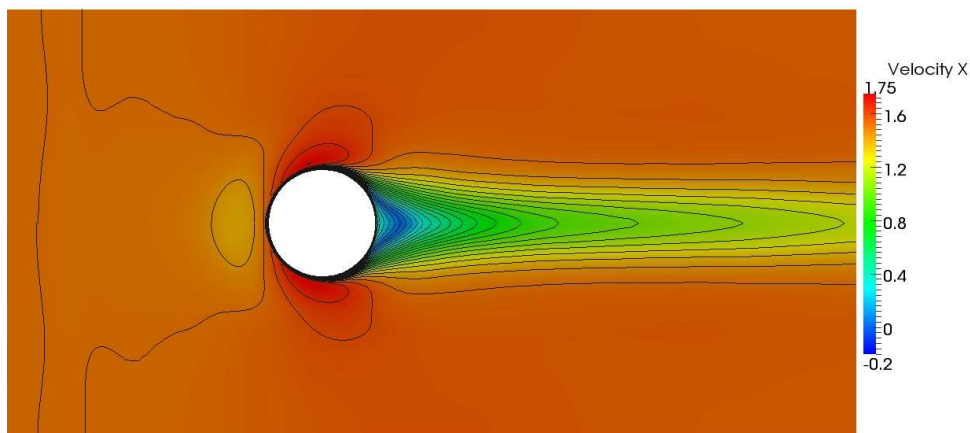
Figure 6.3: 3D cosine 10% hill - Contours of velocity X $[m \cdot s^{-1}]$ - XY slice in the middle of the hill height - $(Re = 6.67 \cdot 10^7 \approx U_\infty = 1.0 \ m \cdot s^{-1})$

6.2 Stratified incompressible turbulent results of the flow over 3D cosine shaped hill

The 3D flow past one cosine shaped hill is considered in this case. The height of the hill is 10% of its basis length. The basis length of the hill is $1000 \, [m]$ so the height h of the hill is $h = 100 \, [m]$.

Lax-Wendroff (MacCormack) scheme have been used to compute following results. The Boussinesq density based model together with the Cebecci-Smith algebraic turbulence model has been used in all three following cases. The gravitational acceleration vector has been set to $\mathbf{g} = (0, \, 0, \, -10)$ approximately as the gravitational acceleration of the Earth for all cases.

All the following computations have been performed using the same computational domain (see figures (4.6), (4.7), (4.8)). The cases differ in the computational grid parameters, the inlet boundary condition for the density and the values of inlet velocity (or one can say in the values of Reynolds number). The stable stratification condition has been set in all simulations but with different ranges (different values of ρ_H and ρ_{0_w}) as the inlet boundary condition according to (4.81), where the height of the domain has been $H = 1000 \, [m]$ in following cases.

6.2.1 Case 1

The fine computational mesh (200 cells in x direction, 100 cells in y direction, 80 cells in z direction), with the near wall resolution $\Delta z_{min} < 1/\sqrt{Re}$, has been considered in the first case.
The inlet boundary condition in the inlet has been set according to the equation (4.81) and its range has been chosen as follows:

- density near the ground $\rho_{0_w} = 1.2 \left[\frac{kg}{m^3} \right]$

- density at the top of the domain $\rho_H = 1.1 \left[\frac{kg}{m^3} \right]$.
No boundary condition for density ρ_w on the ground has been set and the density has been extrapolated on the ground wall.

The Reynolds number has been set to $Re = 10^8$ which corresponds approximately to the inlet velocity $u_\infty = 1.5 \, [m \cdot s^{-1}]$, if one considers that the kinematic viscosity of the air is about $\nu = 1.5 \cdot 10^{-5} \, [m^2 \cdot s^{-1}]$. The uniform velocity distribution in the inlet has been considered there.

Figures (6.4), (6.5) shows results of the first case the distribution of the velocity magnitude, the first one in the XZ plane in the middle of the hill and the second one in the XY plane in the middle of the hill height.
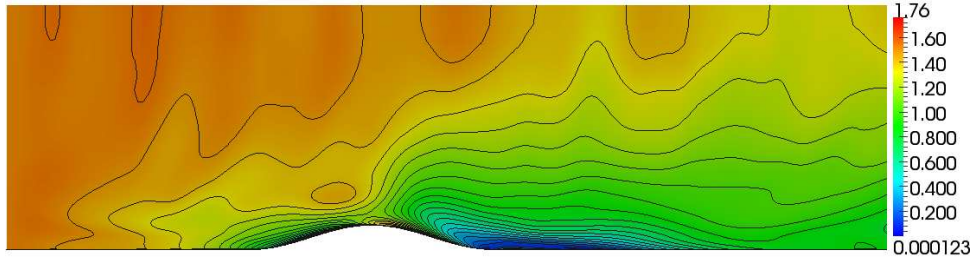
Figure 6.4: 3D cosine 10% hill - Contours of velocity magnitude $[m \cdot s^{-1}]$ - XZ slice in the middle of the domain - ($\rho \in [1.1; 1.2]$, $Re = 10^8 \approx U_\infty = 1.5 \ m \cdot s^{-1}$)
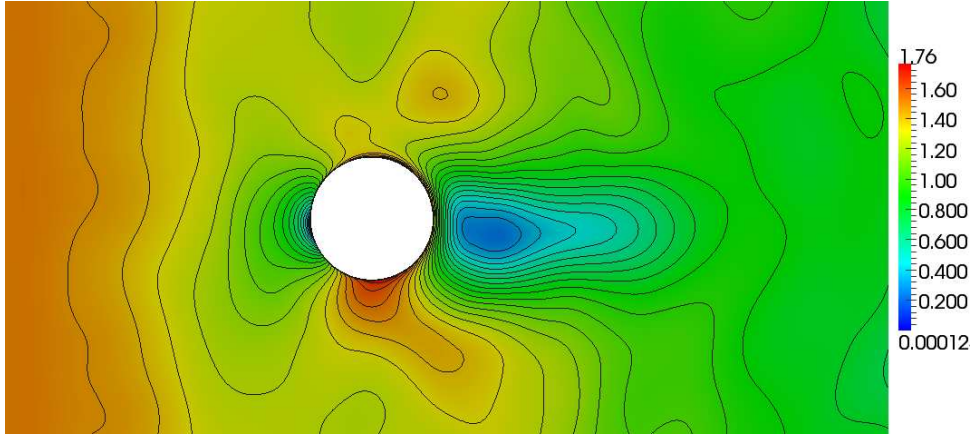
Figure 6.5: 3D cosine 10% hill - Contours of velocity magnitude $[m \cdot s^{-1}]$ - XY slice in the middle of the hill height - ($\rho \in [1.1; 1.2]$, $Re = 10^8 \approx U_\infty = 1.5 \ m \cdot s^{-1}$)

6.2.2 Case 2

The twice coarser computational grid as in the Case 1 (100 cells in x direction, 50 cells in y direction, 40 cells in z direction), with the near wall resolution $\Delta z_{min} \approx 10/\sqrt{Re}$, has been considered in this case.

The inlet boundary condition in the inlet has been set according to the equation (4.81) but the much larger range than in the first and second case has been chosen:

- density near the ground $\rho_{0_w} = 1.2 \left[\frac{kg}{m^3} \right]$

- density at the top of the domain $\rho_H = 0.6 \ \left[\frac{kg}{m^3} \right]$.

The boundary condition for density ρ_w on the ground has been set as Dirichlet boundary condition (i.e. ρ_w is set to be constant value for each boundary face during the computation). The density values have been set using the relation (4.82).

The Reynolds number has been set to lower value $Re = 6.67 \cdot 10^7$ which corresponds approximately to the inlet velocity $u_\infty = 1.0 \ [m \cdot s^{-1}]$, if one considers that the kinematic viscosity of the air is about $\nu = 1.5 \cdot 10^{-5} \ [m^2 \cdot s^{-1}]$. The uniform velocity distribution in the inlet has been considered there same as in previous two cases.

Figures (6.6), (6.8) show results of this second case the distribution of the velocity magnitude in the XZ plane in the middle of the hill and the second one in the XY plane in the middle of the hill height. Figure (5.19) shows the the z velocity component distribution in the XZ plane in the middle of the hill.
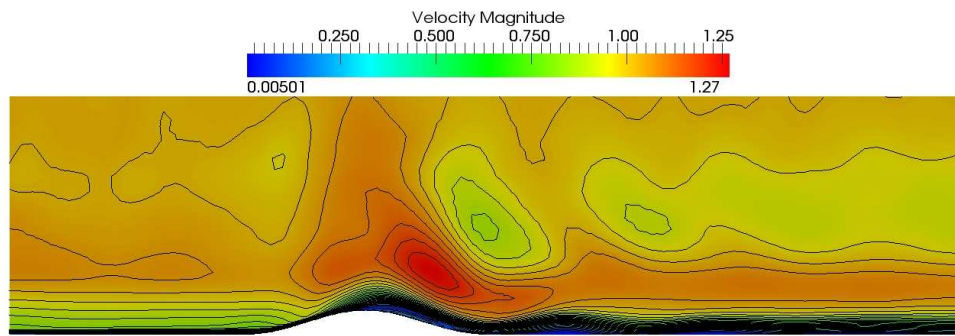
Figure 6.6: 3D cosine 10% hill - Contours of velocity magnitude $[m \cdot s^{-1}]$ - XZ slice in the middle of the domain - ($\rho \in [0.6; 1.2]$, $Re = 6.67 \cdot 10^7 \approx U_\infty = 1.0 \ m \cdot s^{-1}$)
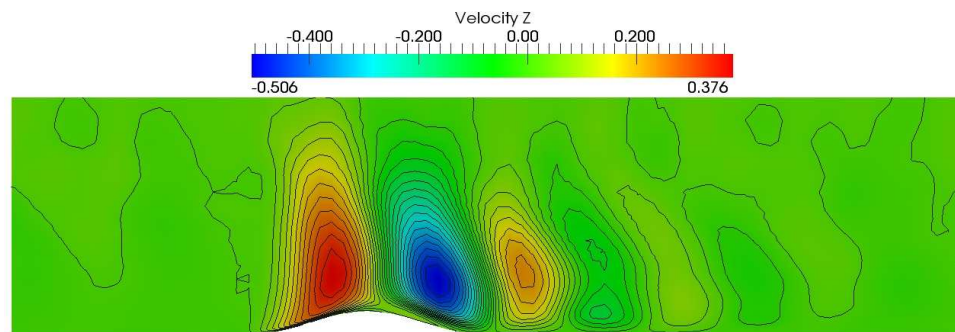
Figure 6.7: 3D cosine 10% hill - Contours of velocity Z $[m \cdot s^{-1}]$ - XZ slice in the middle of the domain - ($\rho \in [0.6; 1.2]$, $Re = 6.67 \cdot 10^7 \approx U_\infty = 1.0 \ m \cdot s^{-1}$)
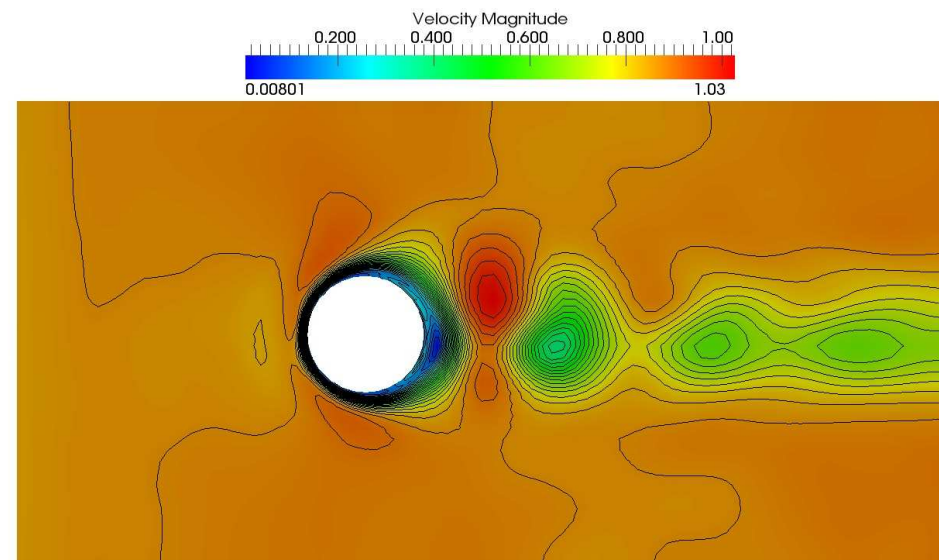
Figure 6.8: 3D cosine 10% hill - Contours of velocity magnitude $[m \cdot s^{-1}]$ - XY slice in the middle of the hill height - ($\rho \in [0.6; 1.2]$, $Re = 6.67 \cdot 10^7 \approx U_\infty = 1.0 \ m \cdot s^{-1}$)

6.2.3 Concluding remarks

The so called "lee waves" should appear in stratified flows [52], [55].

As in the case of 2D simulations one can see the creation of lee waves just in the second case, especially in the figure where the distribution of z component of the velocity vector is shown (6.7). One can see the periodic changes of the vertical direction of the flow, that are damped because of the presence of viscous forces in the fluid.

In the second case where the inlet velocity is lower than in the first case, the density range is much higher and the grid is twice coarser in each direction. The high inlet velocity of the flow lowers the influence of the source term related to the gravity. The higher inlet velocity the lower gravity influence. The range of the density, i.e. the measure of stratification (the density gradient) influences the effect of the gravity source term. The lower density gradient (density gradient is negative in case of stable stratification) the greater effect of the gravity source term.

The influence of the inlet velocity and inlet density gradient could be expressed through the dimensionless numbers: Froude number Fr (the ratio of a body's inertia to gravitational force) or Richardson number Ri (the ratio of potential to kinetic energy), ($Fr = 1/\sqrt{Ri}$). Usually the reciprocal of the Froude number (square root of the Richardson number) K is used in literature [26], [50] (see equation (5.4))

If one computes K according to equation (5.4), one obtains $K = 1.92$ for the Case 1 and $K = 7.07$ for the Case 2. Presented results show the same phenomenon as it is published in all reference papers [26], [34] and [50]. Lee waves appear and its frequency increases with increasing dimensionless number K. Lee waves do not appear in Case 1 even thought the dimensionless number K is greater than zero. They appear only in the Case 2, where K is much higher. The properties of the computational grid could play role in these cases. The coarser grid the less dissipative simulation, i.e. the artificial dissipation added to the solution by the grid is lower on the coarse mesh.

The combination of all these effects could be the cause of the fact that there were no lee waves present in the first case, because the high velocity, the high vertical gradient of the density (low dimensionless number K) and the fine mesh can smooth lee waves.

The next phenomenon visible in the presented figures showing XY plane (6.5), (6.8) is that the flow pattern is not symmetrical in stratified flows. One can see in the figure (6.3) that the flow is symmetrical in the case with neutral stratification. It means that the asymmetry is the most probably caused by the stratification of the flow in our cases.

6.3 Stratified incompressible turbulent results of the flow over two 3D cosine shaped hills

Two cases of the 3D incompressible stratified flows over 2 cosine shaped hills have been computed. The both cases have been performed with the same boundary conditions and the same flow parameters. Case 1 and Case 2 differ in the topology of the computational domain.

The coarser computational grid (120 cells in x direction, 50 cells in y direction, 40 cells in z direction), with the near wall resolution $\Delta z_{min} \approx 10/\sqrt{Re}$, has been considered in these cases.

Lax-Wendroff (MacCormack) scheme have been used to compute following results. The Boussinesq density based model together with the algebraic turbulence model Cebecci-Smith has been used in this case. The gravitational acceleration vector has been set to

$\mathbf{g} = (0, \, 0, \, -10)$ approximately as the gravitational acceleration of the Earth for all cases. The density spread has been chosen as follows:

- density near the ground $\rho_{0_w} = 1.2 \left[\frac{kg}{m^3} \right]$

- density at the top of the domain $\rho_H = 0.6 \left[\frac{kg}{m^3} \right]$.

The boundary condition for density ρ_w on the ground has been set as Dirichlet boundary condition (i.e. ρ_w is set to be constant value for each boundary face during the computation). The density values have been set using the relation (4.82).

The Reynolds number has been set to $Re = 6.67 \cdot 10^7$ which corresponds approximately to the inlet velocity $u_\infty = 1.0 \, [m \cdot s^{-1}]$ if one considers that the kinematic viscosity of the air is about $\nu = 1.5 \cdot 10^{-5} \, [m^2 \cdot s^{-1}]$.

6.3.1   Case 1

The flow over two sinus shaped hills have been considered. The first hill has the height 10% of its basis length (basis $1000 \, [m]$, $h = 100 \, [m]$) and the second one has the height 15% of its basis length (basis $1000 \, [m]$, $h = 150 \, [m]$). The center of the both hills lays on the $(x, \, 0, \, 0)$ axis, they are aligned in x direction (direction of the flow) (see figure (4.9)).

Following figures show the distribution of pressure and velocity in the middle of the domain (XZ plane, $y = 0 \, [m]$) and in the XY plane in located in the middle height of the first hill ($z = 50 \, [m]$)
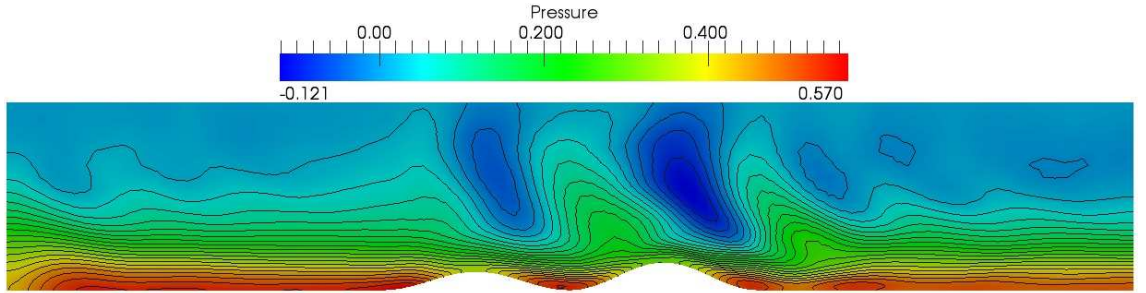
Figure 6.9: 3D cosine 10%, cosine 15% hills - Contours of pressure perturbations [Pa] - XZ slice in the middle of the domain ($\rho \in [0.6; 1.2]$, $Re = 6.67 \cdot 10^7 \approx U_\infty = 1.0 \, m \cdot s^{-1}$)
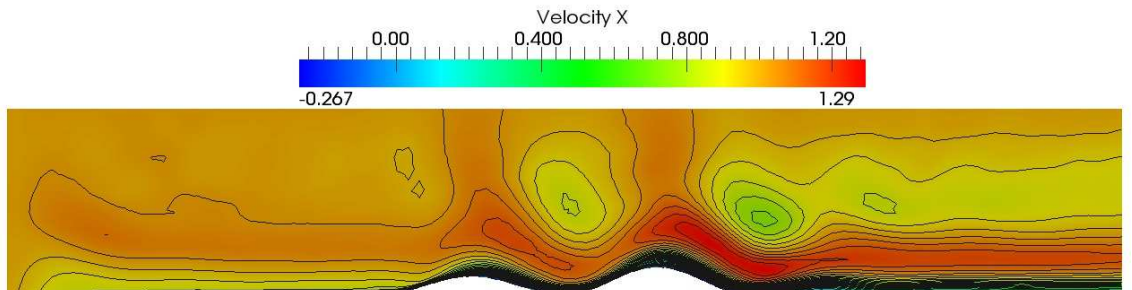
Figure 6.10: 3D cosine 10%, cosine 15% hills - Contours of velocity X $[m \cdot s^{-1}]$ - XZ slice in the middle of the domain ($\rho \in [0.6; 1.2]$, $Re = 6.67 \cdot 10^7 \approx U_\infty = 1.0 \, m \cdot s^{-1}$)
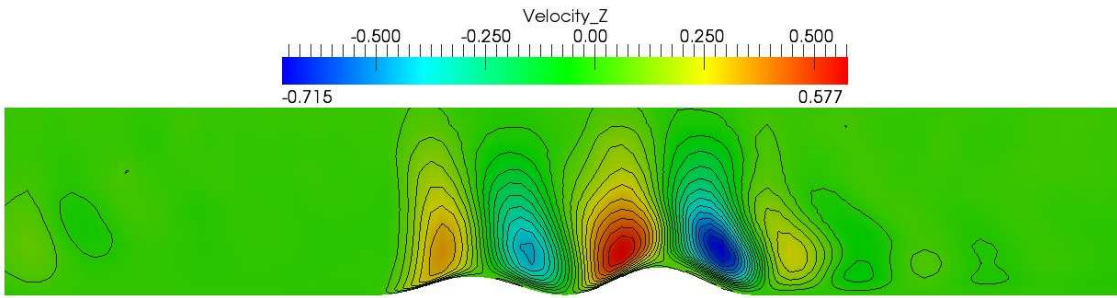
Figure 6.11: 3D cosine 10%, cosine 15% hills - Contours of velocity Z $[m \cdot s^{-1}]$ - XZ slice in the middle of the domain ($\rho \in [0.6; 1.2]$, $Re = 6.67 \cdot 10^7 \approx U_\infty = 1.0 \ m \cdot s^{-1}$)
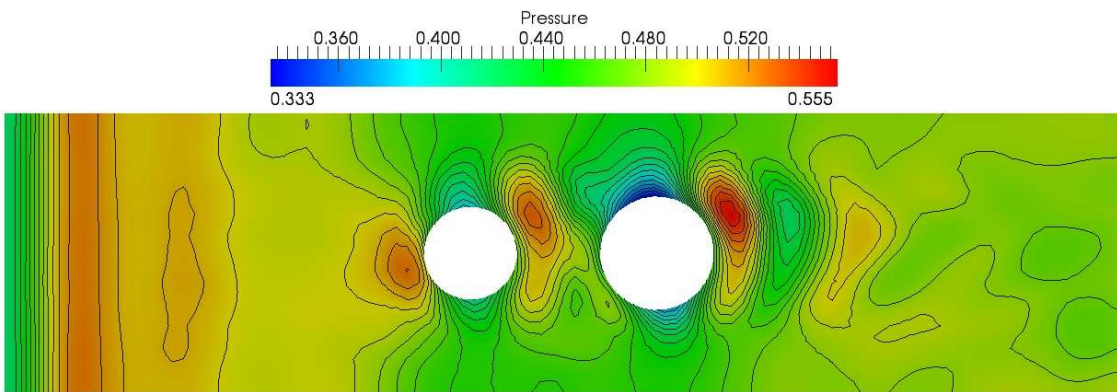
Figure 6.12: 3D cosine 10%, cosine 15% hills - Contours of pressure pert. $[Pa]$ XY slice in the middle of the 1$^{\text{st}}$ hill height ($\rho \in [0.6; 1.2]$, $Re = 6.67 \cdot 10^7 \approx U_\infty = 1.0 \ m \cdot s^{-1}$)
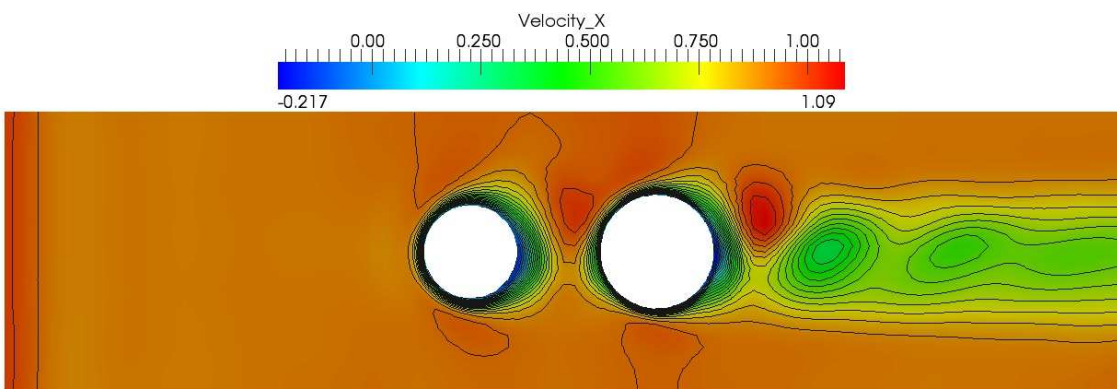
Figure 6.13: 3D cosine 10%, cosine 15% hills - Contours of velocity X $[m \cdot s^{-1}]$ - XY slice in the middle of the 1$^{\text{st}}$ hill height ($\rho \in [0.6; 1.2]$, $Re = 6.67 \cdot 10^7 \approx U_\infty = 1.0 \ m \cdot s^{-1}$)
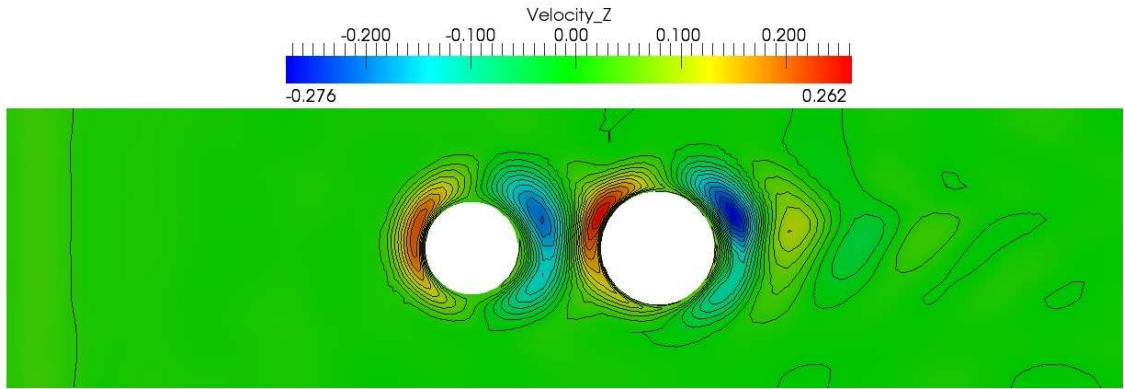
Figure 6.14: 3D cosine 10%, cosine 15% hills - Contours of velocity Z $[m \cdot s^{-1}]$ - XY slice in the middle of the 1st hill height ($\rho \in [0.6; 1.2]$, $Re = 6.67 \cdot 10^7 \approx U_\infty = 1.0 \ m \cdot s^{-1}$)

6.3.2 Case 2

The flow over two sinus shaped hills have been considered. Both hills have the height 10% of its basis length (basis $1000 \, [m]$, $h = 100 \, [m]$) and the center of the first hill lays one quarter of its basis length moved in the direction of -y axis from the x axis and the center of the second hill lays one quarter of its basis length moved in the direction of +y axis from the x axis, so only their quarters are aligned in the x direction (direction of the flow) (see figure (4.10)).

Following figures show the distribution of pressure and velocity in XZ planes (in the middle of the domain $y = 0 \, [m]$ and in the middle of the cosine hills $y = \pm 500 \, [m]$) and in the XY plane in located in the middle of the hills ($z = 50 \, [m]$).
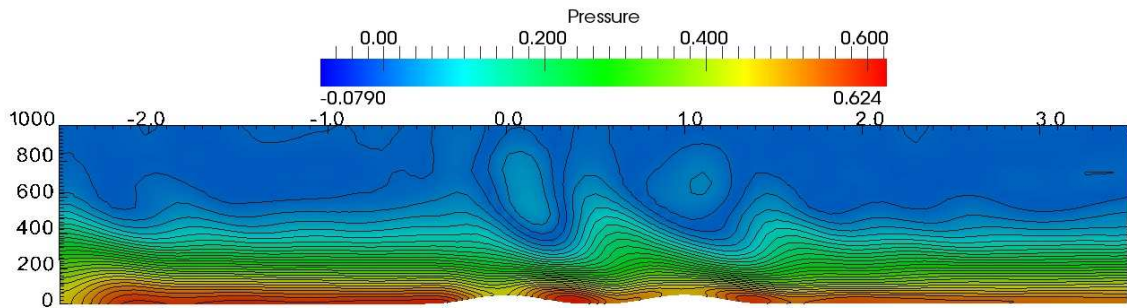
Figure 6.15: 3D cosine 10%, cosine 10% hills - Contours of pressure pert. [Pa] - XZ slice in the middle of the domain ($\rho \in [0.6; 1.2]$, $Re = 6.67 \cdot 10^7 \approx U_\infty = 1.0 \ m \cdot s^{-1}$)
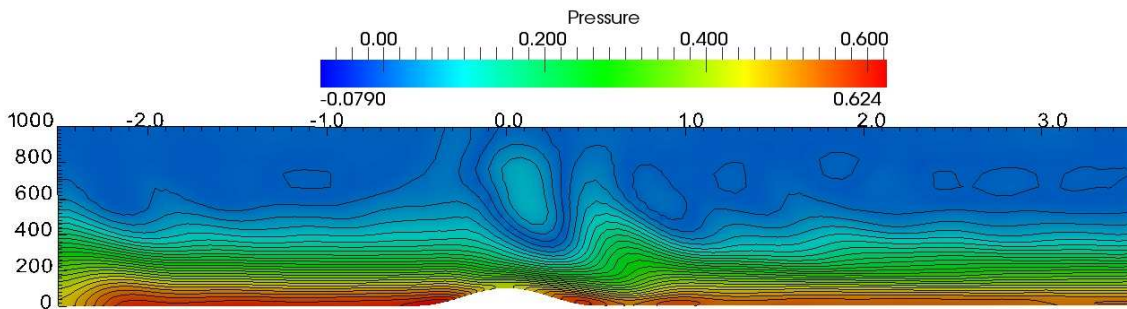
Figure 6.16: 3D cosine 10%, cosine 10% hills - Contours of pressure pert. [Pa] - XZ slice in the middle of the 1st hill ($\rho \in [0.6; 1.2]$, $Re = 6.67 \cdot 10^7 \approx U_\infty = 1.0 \ m \cdot s^{-1}$)
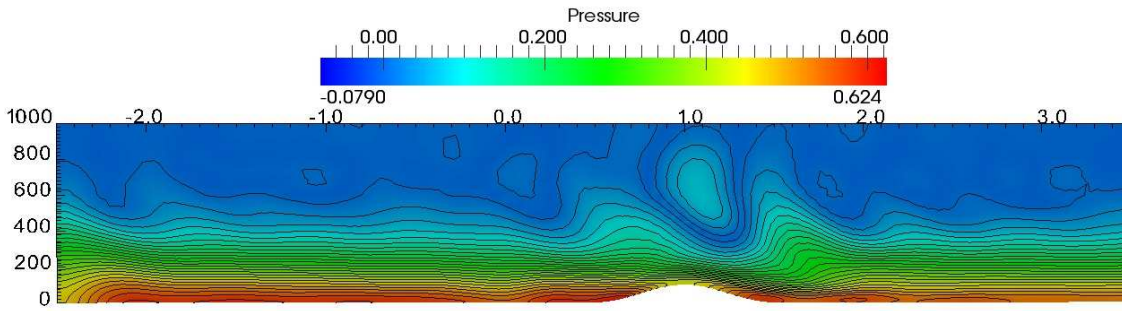
Figure 6.17: 3D cosine 10%, cosine 10% hills - Contours of pressure pert. [Pa] - XZ slice in the middle of the 2nd hill ($\rho \in [0.6; 1.2]$, $Re = 6.67 \cdot 10^7 \approx U_\infty = 1.0 \ m \cdot s^{-1}$)
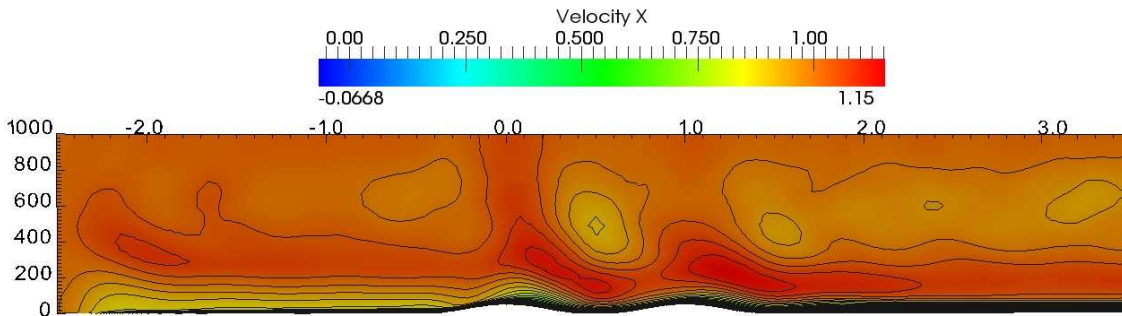
Figure 6.18: 3D cosine 10%, cosine 10% hills - Contours of velocity X $[m \cdot s^{-1}]$ - XZ slice in the middle of the domain ($\rho \in [0.6; 1.2]$, $Re = 6.67 \cdot 10^7 \approx U_\infty = 1.0 \ m \cdot s^{-1}$)
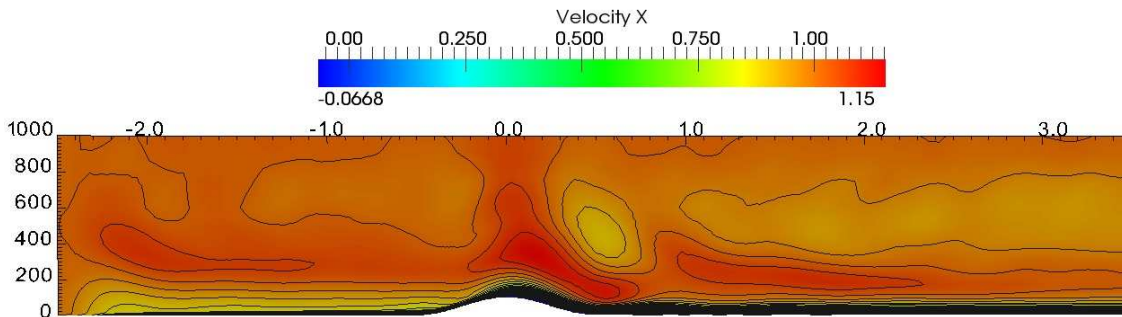
Figure 6.19: 3D cosine 10%, cosine 10% hills - Contours of velocity X $[m \cdot s^{-1}]$ - XZ slice in the middle of the 1st hill ($\rho \in [0.6; 1.2]$, $Re = 6.67 \cdot 10^7 \approx U_\infty = 1.0 \ m \cdot s^{-1}$)
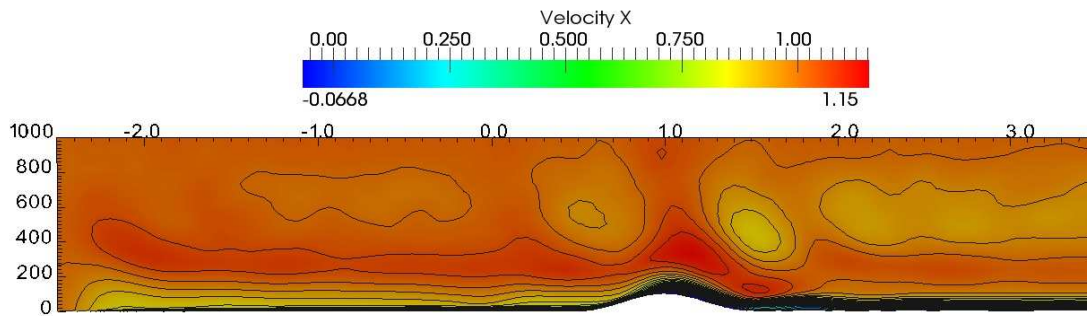
Figure 6.20: 3D cosine 10%, cosine 10% hills - Contours of velocity X $[m \cdot s^{-1}]$ - XZ slice in the middle of the 2nd hill ($\rho \in [0.6; 1.2]$, $Re = 6.67 \cdot 10^7 \approx U_\infty = 1.0 \ m \cdot s^{-1}$)
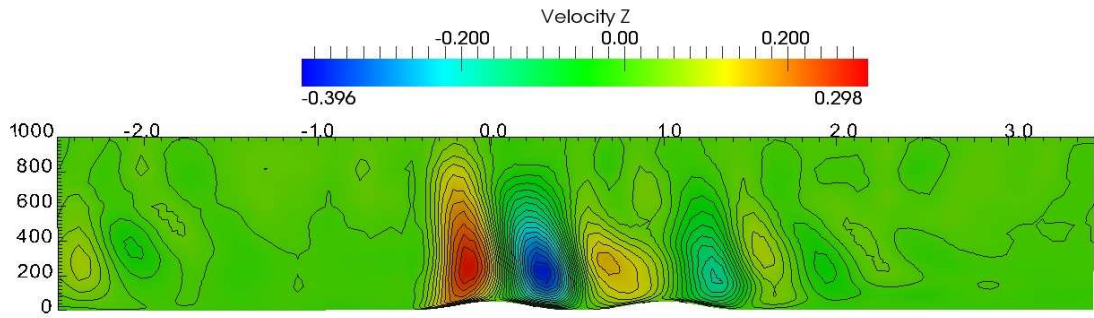
Figure 6.21: 3D cosine 10%, cosine 10% hills - Contours of velocity Z $[m \cdot s^{-1}]$ - XZ slice in the middle of the domain ($\rho \in [0.6; 1.2]$, $Re = 6.67 \cdot 10^7 \approx U_\infty = 1.0 \ m \cdot s^{-1}$)
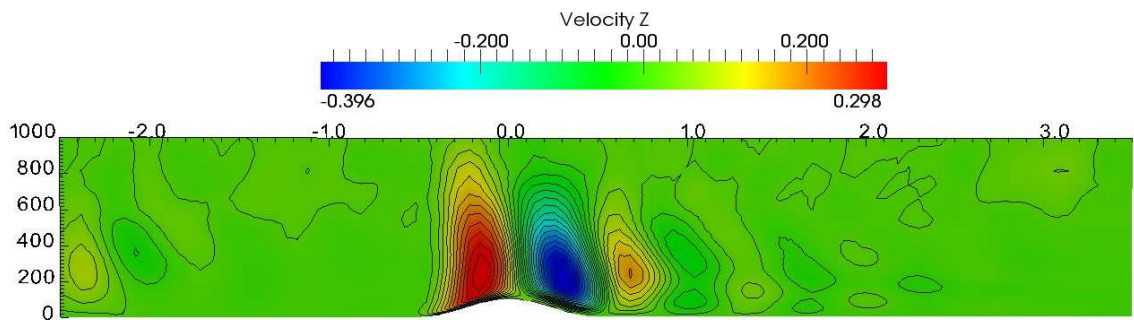
Figure 6.22: 3D cosine 10%, cosine 10% hills - Contours of velocity Z $[m \cdot s^{-1}]$ - XZ slice in the middle of the 1st hill ($\rho \in [0.6; 1.2]$, $Re = 6.67 \cdot 10^7 \approx U_\infty = 1.0 \ m \cdot s^{-1}$)
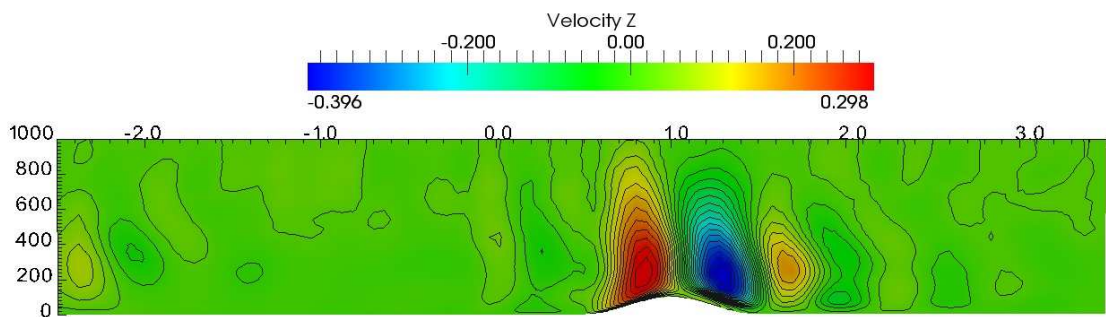
Figure 6.23: 3D cosine 10%, cosine 10% hills - Contours of velocity Z $[m \cdot s^{-1}]$ - XZ slice in the middle of the 2nd hill ($\rho \in [0.6; 1.2]$, $Re = 6.67 \cdot 10^7 \approx U_\infty = 1.0 \ m \cdot s^{-1}$)
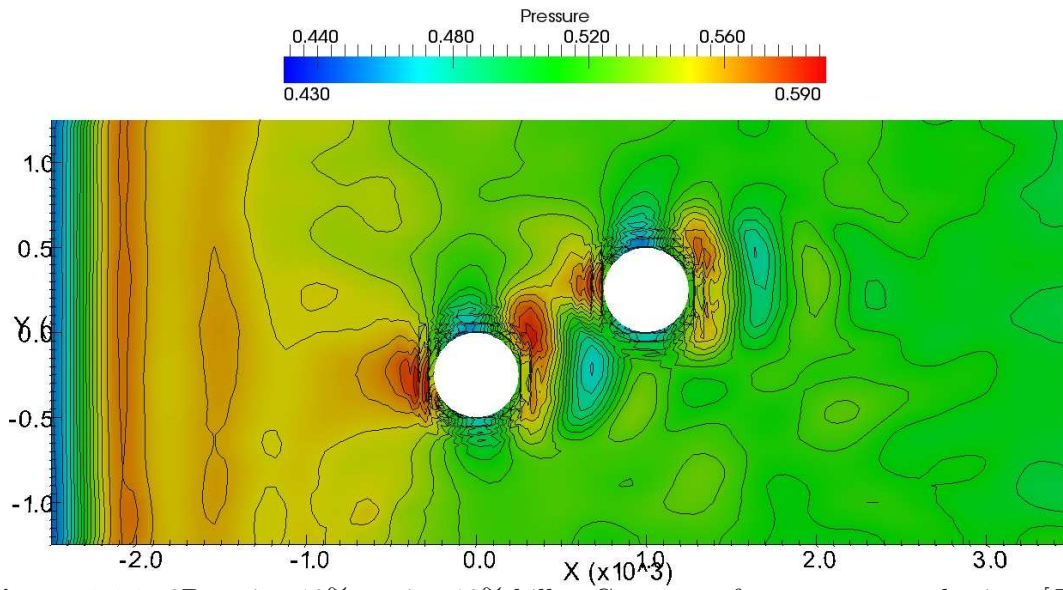
Figure 6.24: 3D cosine 10%, cosine 10% hills - Contours of pressure perturbations $[Pa]$ - XY slice in the middle of the hills height ($\rho \in [0.6; 1.2]$, $Re = 6.67 \cdot 10^7 \approx U_\infty = 1.0 \ m \cdot s^{-1}$)
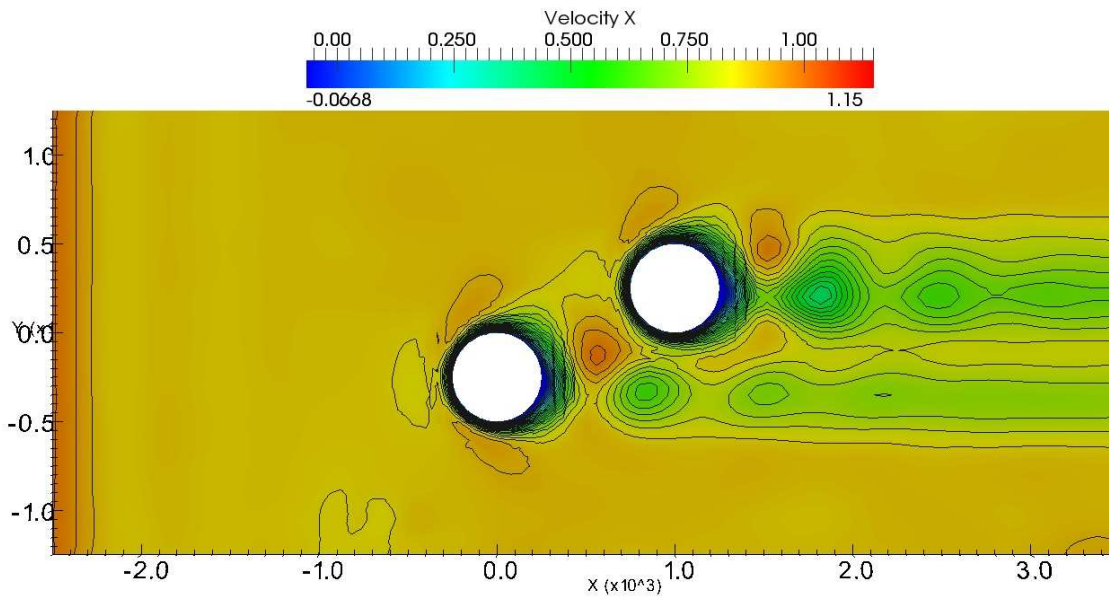
Figure 6.25: 3D cosine 10%, cosine 10% hills - Contours of velocity X $[m \cdot s^{-1}]$ - XY slice in the middle of the hills height ($\rho \in [0.6; 1.2]$, $Re = 6.67 \cdot 10^7 \approx U_\infty = 1.0 \ m \cdot s^{-1}$)
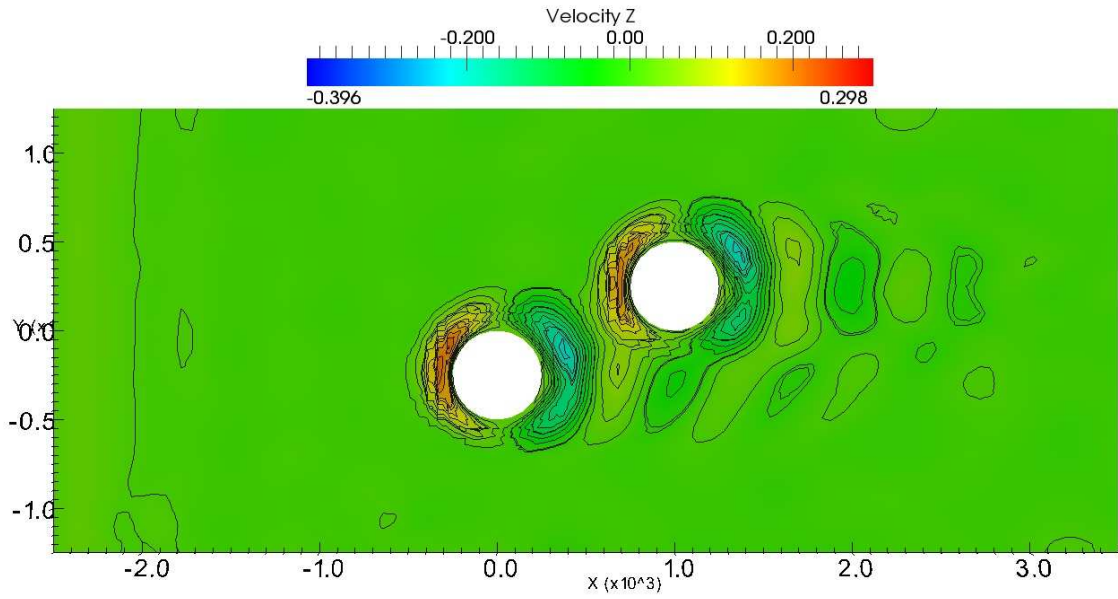
Figure 6.26: 3D cosine 10%, cosine 10% hills - Contours of velocity Z $[m \cdot s^{-1}]$ - XY slice in the middle of the hills height ($\rho \in [0.6; 1.2]$, $Re = 6.67 \cdot 10^7 \approx U_\infty = 1.0 \ m \cdot s^{-1}$)
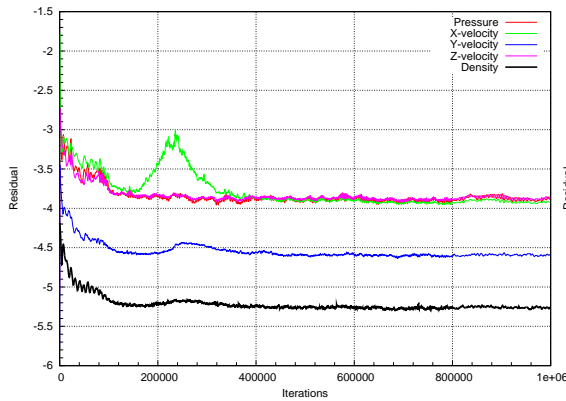
Figure 6.27: Case 1 - Residuals
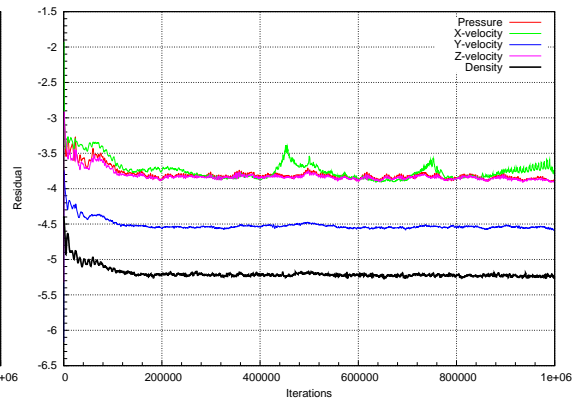
Figure 6.28: Case 2 - Residuals

6.3.3 Concluding remarks

All the computations seem to be converged to steady state, as one can see from residual plots (see figures (6.27) and (6.28)).

Lee waves are present in both cases, as one can see in presented figures, especially in the figures where the distribution of z component of the velocity vector is shown (6.11), (6.21), (6.22), (6.23). One can see there the periodic changes of the vertical direction of the flow, that are damped because of the presence of viscous forces in the fluid.

The results of the Case 1 in XZ planes are comparable with 2D results from the section 5.4. The results from XZ cut in the middle of the 3D domain can be approximated by the simulation using the 2D domain.

One can see the asymmetry of the solution in the figures (6.24), (6.25), (6.26). This asymmetry is most probably caused by the stratification of the fluid and subsequent creation of lee waves, because there is no asymmetry present in case of neutral stratification in 3D computations, as one can see in the figure (6.3). The result in the figure (6.3) has been obtained by the 3D computation using the domain with one cosine hill (see figure (4.6)) with the same settings as the previously presented results except the stratification of the fluid. The density was constant in this case and the gravity acceleration has been set to zero ($\mathbf{g} = (0, 0, 0)$).

The dimensionless number $K = 7.07$ computed using relation (5.4) and taking into account that h is the height of the first hill $h = 100\,[m]$ is the same for both cases.

Chapter 7

Conclusion

The model for the simulation of the stratified turbulent flows in atmospheric boundary layer (ABL) has been introduced. There have been obtained several 2D and 3D numerical results using various geometry configurations, that should simulates the real flows in atmospheric boundary layer.

Presented model predicts the creation of so called lee waves (in 2D and 3D flows), that should appear in the stratified flows in ABL. Lee waves are atmospheric standing waves, that are created behind the obstacles (on the lee sides of hills, mountains), that stays on the ground, due to the non constant temperature (density) (stratification of the fluid) in atmospheric boundary layer flows. They are periodic changes of atmospheric pressure, temperature (density).

Presented results show that the creation of the lee waves depends on the dimensionless number $K = 1/Fr = \sqrt{Ri}$ (the reciprocal of the Froude number/square root of the Richardson number, see equation (5.4)) and the grid resolution. Lee waves appeared only on the coarser meshes when the dimensionless number K has been approximately $K \approx 7$. No lee waves have been observed in the results where the dimensionless number K has been lower than 2.

It is possible to say that the model is good for prediction of stratified flows in atmospheric boundary layer. But the Cebecci-Smith algebraic turbulence model and the explicit Lax-Wendroff (MacCormack form) numerical scheme seem to be the limitations of a applicability of this model to more complex stratified boundary layer flows.

The problem with the algebraic turbulence model is that the algebraic turbulence model is not a best turbulence model for the 3D turbulent flows over a complex geometries predictions. And the problem with explicit scheme is that the explicit scheme is only conditionally stable and the strict restriction for the time step size has to be applied in order to achieve convergence to the solution. The maximum time step size is related to the size of the smallest cell in the computational grid, which has to be very small in computation with such a high Reynolds numbers as appears in ABL flows, where $Re = 10^7 - 10^8$. The semi-implicit or implicit scheme will be much more suitable for the computations of the flows in atmospheric boundary layer.

The reason why the explicit Lax-Wendroff numerical scheme (MacCormack form) and the Cebecci-Smith algebraic turbulence model have been chosen is the fact that they are quite easy to implement and therefore the model could be quickly implemented, validated and tested.

From the reason mentioned above the standard and realizable $k - \varepsilon$ turbulence models (turbulent kinetic energy transport type turbulence models) have been implemented and

validated (see section 5.1). The $k-\varepsilon$ models have been implemented for neutrally stratified flows, therefore the comparison with the results of flows in ABL has been made only with the results of neutrally stratified flows obtained by Ivo Sládek et al. [34] and Eidsvik and Utnes [26]. The comparison shows very good agreement of the results of neutrally stratified flows in ABL, as reader can see in section 5.2.

Two tasks flows from these conclusions for a future work. At first to implement the $k-\varepsilon$ turbulence model to the solver for stratified flows and compare obtained results with another numerical results. Or to implement other more sophisticated turbulence model applicable to the atmospheric boundary layer flows. And the second will be to implement modern implicit or semi-implicit scheme in order to achieve a more robust and faster solver for simulations of the turbulent stratified atmospheric boundary layer flows.

References

Books

[1] Dvořák R., Kozel K.:
Matematické metody v aerodynamice,
Czech Technical University (lecture notes), Prague, 1992

[2] Feistauer M., Felcman J., Straškraba I.:
Mathematical and Computational Methods for Compressible Flow,
Clarendon Press, Oxford 2003.

[3] Ferziger J. H., Perić M.:
Computational Methods for Fluid Dynamics,
Third Edition, Springer Verlag, Berlin, 2002

[4] Fletcher C. A. J.:
Computational Techniques for Fluid Dynamics I and II,
Springer Verlag, Berlin 1996.

[5] Hirsh C.:
Numerical Computation of Internal and External Flows I and II,
John Willey and Sons, New York 1991.

[6] Holton J. R.:
An Introduction to Dynamic Meteorology,
Elsevier Academic Press, 2004

[7] Kozel K., Dvořák R.:
Matematické modelování v aerodynamice,
Vydavatelství ČVUT, Prague, 1996

[8] S. Prata:
C++ Primer Plus (Fourth Edition),
Sams, Indianapolis, IN, USA, 2001

[9] Příhoda J., Louda P.:
Matematické Modelování Turbulentního Proudění,
Czech Technical University (lecture notes), Prague, 2007

[10] Stull R. B.:
An introduction to boundary layer meteorology,
Springer, 1988

[11] Versteeg H. K., Malalasekera W.:
An Introduction to Computational Fluid Dynamics The Finite Volume Method,
Longman Scientific & Technical, Harlow, 2005

Theses

[12] Beneš L.:
Numerické řešení proudění v mezní vrstvě atmosféry,
Ph.D. Thesis, Czech Technical University - Faculty of Mechanical Engineering - Department of Mathematics, Prague, 2000

[13] Bodnár T.:
Numerical Simulation of Flows and Pollution Dispersion in Atmospheric Boundary Layer,
Ph.D. Thesis, Czech Technical University - Faculty of Mechanical Engineering - Department of Mathematics, Prague, 2003

[14] Pirkl L.:
Development and Validation of a Stabilized Finite Element Solver for Variable Density Flows,
Diploma Course Report, Von Karman Institute for Fluid Dynamics, Rhode-St-Genese Belgium, 2009

[15] Sládek I.:
Mathematical Modelling and Numerical Solution of Some 2D and 3D cases of Atmospheric Boundary Layer Flow
Czech Technical University - Faculty of Mechanical Engineering - Department of Mathematics, Prague, 2004

Articles

[16] Barakos G., Mitsoulis E., Assimacopoulos D.:
Natural Convection Flow in a Square Cavity Revisited: Laminar and Turbulent Models with Wall Functions,
International Journal for Numerical Methods in Fluids, vol. 18, 1994, p. 695 - 719

[17] Beneš L., Fürst J.:
Numerical Simulation of the Stratified Flows in the Open Air,
Topical Problems of Fluid Mechanics 2010 Proceedings, Prague, Institute of Thermomechanics, AS CR, v.v.i., 2010, p. 7 - 10

[18] Beneš L., Bodnár T., Kozel K., Sládek I.:
Two Cases of the Real ABL Flow over Complex Orography,
Finite Volumes for Complex Applications V. London, ISTE Ltd, 2008, p. 209-216

[19] Beneš L., Fürst J., Fraunié Ph.:
Numerical Simulation of the Stratified Flow,
Topical Problems of Fluid Mechanics 2008 Proceedings, Prague, Institute of Thermomechanics, AS CR, v.v.i., 2008, p. 5 - 8

[20] Beneš L., Kozel K., Sládek I.:
Numerical Solution of Atmospheric Boundary Layer Flow,
Zeitschrift fǍźr angewandte Mathematik und Mechanik, 2000, vol. 80, no. 3, p. S619-S620

[21] Beneš L., Sládek I., Kozel K.:
Numerical Solution of Flow in the Athmospheric Boundary Layer
Topical Problems of Fluid Mechanics 1998 Proceedings, Prague, Institute of Thermomechanics, AS CR, v.v.i., 1998, p. 3 - 4

[22] Bodnár T., Kozel K., Sládek I.:
Matematické modelování a numerické řešení proudění v mezní vrstvě atmosféry,
Topical Problems of Fluid Mechanics 1996 Proceedings, Prague, Institute of Thermomechanics, AS CR, v.v.i. 1996, p. 3 - 4

[23] Castro I. P., Apsley D. D.:
Flow and Dispersion over Hills,
A Comparison between Numerical Predictions and Experimental Data
Journal of Wind Engineering and Industrial Aerodynamics, 67 & 68, 1997, p. 375 - 386

[24] Castro I. P., Apsley D. D.:
Flow and Dispersion over Topography,
A Comparison between Numerical and Laboratory Data for Two-Dimensional Flows
Atmospheric Environment, Vol. 31, Issue 6, 1997, p. 839-850

[25] Chorin A.J.:
The numerical solution of the Navier-Stokes equations for an incompressible fluid,
Bulletin of the American Mathematical Society 73, 1967, p. 928 - 931

[26] Eidsvik K., Utnes T.:
Flow separation and hydrostatic transition over hills modeled by the Reynolds equations,
Journal of Wind Engineering and Industrial Aerodynamics, Issues 67 - 68 (1997), p. 408 - 413

[27] Fürst J., Fraunié Ph.:
The High Order Schemes for Stratified Flows,
Topical Problems of Fluid Mechanics 2007 Proceedings, Prague, Institute of Thermomechanics, AS CR, v.v.i., 2007, p. 49 - 52

[28] Henkes R. A. W. M., van der Flugt F. F., Hoogendoorn C. J.:
Natural Convection Flow in a Square Cavity Calculated with Low-Reynolds-Number Turbulence Models,
International Journal of Heat and Mass Transfer, vol. 34, 1991, p. 1543 - 1557

[29] MacCormack R. W., Paullay A. J.:
Computational Efficiency Achived by Time Splitting of Finite Difference Operators,
AIAA Paper 72-154, San Diego, California, 1972

[30] MacCormack R. W.:
The Effect of viscosity in hypervelocity impact cratering,
AIAA Paper 69-354, 1969

[31] McDonald P. W.:
The Computation of Transonic Flow through Two-Dimensional Gas Turbine Cascades,
ASME Paper 71-GT-89, 1971

[32] Peng S.-H., Davidson L.:
Computation of Turbulent Buoyant Flows in Enclosures with Low-Reynolds-Number $k - \omega$ models,
International Journal of Heat and Fluid Flow, vol. 20, 1999, p. 172 - 184

[33] Shih T.-H., Liou W.W., Shabbir A., Yang Z., Zhu J.:
A New k-ε Eddy Viscosity Model for High Reynolds Number Turbulent Flows - Model Development and Validation,
NASA Technical Memorandum 106721, 1994

[34] Sládek I., Kozel K., Jaňour Z.:
On the Numerical Validation Study of Stratified Flow over 2D - Hill Test Case,
Finite Volumes for Complex Applications VI, Problems & Perspectives, Berlin, Springer-Verlag, 2011, vol. 1, p. 731-739

[35] Sládek I., Kozel K., Jaňour Z.:
On the Thermally Stratified Atmospheric Flow Modeling,
Topical Problems of Fluid Mechanics 2010 Proceedings, Prague, Institute of Thermomechanics, AS CR, v.v.i., 2010, p. 135-138

[36] Sládek I., Kozel K., Jaňour Z.:
On the Validation Study Devoted to Stratified Atmospheric Flow over an Isolated Hill,
Colloquium Fluid Dynamics 2010 Proceedings. Prague, Institute of Thermomechanics, AS CR, v.v.i., 2010, p. 21-22

[37] Sládek I., Kozel K., Jaňour Z.:
On the Validation 2D - Flow Study over an ERCOFTAC Hill,
Colloquium Fluid Dynamics 2007 Proceedings, Prague, Academy of Sciences of the Czech Republic, Institute of Thermomechanics, 2007, p. 83-84

[38] Sládek I., Kozel K., Jaňour Z.:
On the Turbulence modelling of Atmospheric Flow over a Coal Depot,
Topical Problems of Fluid Mechanics 2007 Proceedings, Prague, Institute of Thermomechanics, AS CR, v.v.i., 2007, p. 161 - 164

[39] Šimonek J., Kozel K., Jaňour Z.:
Numerical Solution of 2D and 3D Atmospheric Boundary Layer Stratified Flows,
Finite Volumes for Complex Applications VI, Problems & Perspectives, Berlin, Springer-Verlag, 2011

[40] Šimonek J., Kozel K., Jaňour Z.:
Numerical Simulation Stratified Flows in Atmospheric Boundary Layer,
Topical Problems of Fluid Mechanics 2011 Proceedings, Prague, Institute of Thermomechanics, AS CR, v.v.i., 2011

[41] Šimonek J., Kozel K., Jaňour Z.:
Numerical Simulation of 3D Stratified Flows in Atmospheric Boundary Layer,
Topical Problems of Fluid Mechanics 2010 Proceedings, Prague, Institute of Thermo-
mechanics, AS CR, v.v.i., 2010, p. 143-146

[42] Šimonek J., Kozel K., Jaňour Z.:
Numerical Solution of 2D and 3D Stratified Flows in Atmospheric Boundary Layer,
Proceedings of the Fifth Conference on Computation Fluid Dynamics ECCOMAS
CFD 2010, Lisbon, Instituto Superior Técnico, Technical University of Lisbon, Na-
tional Civil Engineering Laboratory, 2010

[43] Šimonek J., Tauer M., Kozel K., Jaňour Z.:
Computation of 2D Stratified Flows in Atmospheric Boundary Layer,
Colloquium Fluid Dynamics 2009 Proceedings, Prague, Institute of Thermomechan-
ics, AS CR, v.v.i., 2009

[44] Šimonek J., Kozel K., Fraunié Ph., Jaňour Z.:
Numerical Solution of 2D Stratified Flows in Atmospheric Boundary Layer,
Topical Problems of Fluid Mechanics 2008, Prague 2008

[45] Šimonek J., Kozel K., Trefilík J.:
Numerical Solution of Inviscid an Viscous Flows with Application,
Topical Problems of Fluid Mechanics 2007, Prague, Institute of Thermomechanics,
AS CR, v.v.i., 2007, p. 169-172

[46] Tauer M., Šimonek J., Kozel K., Jaňour Z.:
Mathematical Modeling of 2D Atmospheric Boundary Layer Flow Field,
Topical Problems of Fluid Mechanics 2010 Proceedings, Prague, Institute of Thermo-
mechanics, AS CR, v.v.i., 2010, p. 147-150

[47] Tauer M., Šimonek J., Kozel K., Jaňour Z.:
Numerické řešení proudění v blízkosti zemského povrchu,
Topical Problems of Fluid Mechanics 2009, Prague, Institute of Thermomechanics,
AS CR, v.v.i., 2009, p. 99-102

[48] Tauer M., Šimonek J., Kozel K.:
Computation of 2D Flows in Atmospheric Boundary Layer,
Computational Mechanics 2009 - Book of Extended Abstracts, Pilsen, University of
West Bohemia, 2009

[49] Trefilík J., Šimonek J., Kozel K., Příhoda J.:
Numerical Solution of 2D Flow in a Channel,
Topical Problems of Fluid Mechanics 2008, Prague, Institute of Thermomechanics,
AS CR, v.v.i., 2008, p. 121-124

[50] Uchida T., Ohya Y.:
Numerical Study of Stably Stratified Flows over a Two Dimensional Hill in a Channel
of Finite Depth,
Fluid Dynamics Research 29/2001, p. 227 - 250

Reports

[51] Dubcová L., Feistauer M., Horáček J., Sváček P.:
Numerická simulace interakce kmitajícího profilu a turbulentního proudění,
Research Report, Institute of Thermomechanics, AS CR, v.v.i., 2006

[52] Durran D. R.:
Lee Waves and Mountain Waves,
Encyclopedia of Atmospheric Sciences, Elsevier Science Ltd., 2003, p 1161 - 1169

[53] Jaňour Z.:
O matematickém modelování stratifikované atmosféry,
Research Report, Institute of Thermomechanics, AS CR, v.v.i., 2007

[54] Příhoda J.:
Řešení dvourozměrného proudění nestlačitelné tekutiny pomocí algebraického modelu turbulence,
Research Report, Institute of Thermomechanics, AS CR, v.v.i., 2005

[55] Wurtele M.G., Datta A., Sharman R.D.:
Lee Waves: Benign and Malignant,
NASA Contractor Report 186024, 1993